Cyprus University of Technology

Faculty of Engineering and Technology

Doctoral Dissertation

SOLUTION PROCESSED ELECTRODES FOR ORGANIC SOLAR CELLS

Efthymios Georgiou

Limassol, March 2018

CYPRUS UNIVERSITY OF TECHNOLOGY

Faculty of Engineering and Technology

Department of Mechanical Engineering and Material Science and Engineering

Molecular Electronics and Photonics Research Unit

Doctoral Dissertation

SOLUTION PROCESSED ELECTRODES FOR ORGANIC SOLAR CELLS

Efthymios Georgiou

Limassol, March 2018

Approval Form

Doctoral Dissertation

SOLUTION PROCESSED ELECTRODES FOR ORGANIC SOLAR CELLS

Presented by

Efthymios Georgiou

Supervisor: Professor Stelios A. Choulis

Signature _____

Member of the committee (President): Professor Evangelos Vitoratos

Signature _____

Member of the committee: Associate Professor Itskos Grigorios

Signature _____

Cyprus University of Technology

Limassol, March 2018

Copyrights

The approval of the dissertation by the Department of Mechanical Engineering and Materials Science and Engineering does not imply necessarily the approval by the Department of the views of the writer.

Acknowledgments

I am thankful to my supervisor Professor Stelios A. Choulis for giving me the opportunity to be a member of Molecular Electronics and Photonics Research Unit and for his precious guidance throughout the completion of this Thesis.

Special thanks to all former and present members of the Molecular Electronics and Photonics Research Unit, Dr. Achilleas Savva, Dr. Marios Neophytou, Dr. Felix Hermerschmidt, Dr. Ignasi Burges-Ceballos, Dr. Vasileios Drakonakis, Dr. Panayiotis Pouloupatis, Dr. Ioannis Papadas, Dr. Dimitris Tzikritzis, Sergey Pozov, Fedros Galatopoulos, Apostolos Ioakeimides and Alexandra Chrysou for sharing their knowledge with me and fruitful discussions during our collaboration.

Thank you to my family, my parents, sisters and Alexia for all the support and patience throughout the years.

ABSTRACT

Organic photovoltaics (OPVs) have attracted great scientific interest due to their low weight, flexibility and possibility of roll-to-roll mass production, providing green energy with low cost. The next important research and development milestones of OPVs are considered to be the avoidance of high cost materials, such as the transparent conductor indium tin oxide (ITO), and the avoidance of high vacuum and energy intensive deposition techniques, such as thermal evaporator, which is commonly used for the deposition of the reflective metal top electrode. Through the use of solution-processed electrodes, OPVs can be fabricated in a roll to roll production line. The inkjet printing (IJP) deposition technique has the potential to be introduced in the roll to roll production of OPVs due to its ability to print two-dimensional patterns and save material with drop on demand technology.

In this thesis (Chapter 3), the potential of replacing the rigid and expensive ITO with IJP copper grids was investigated. Copper (Cu) nanoparticle inks have drawn much attention since they are cheaper than silver nanoparticle inks. A printing and sintering optimization of a proposed Cu ink is presented, resulting in high quality and conductive Cu grid structures. However, challenges arise during the implementation of Cu grid in the fabrication of OPVs. Specifically, Cu oxidizes during the necessary annealing step of PEDOT:PSS at 140°C in air, resulting in reduced conductivity. A highly conductive PEDOT:PSS formulation was introduced in order to enhance the conductivity of the electrode and assist in current collection. 3.4% power conversion efficiency (PCE) was achieved whereas the reference ITO-based device exhibited 4.9% PCE.

The two following chapters (Chapters 4 and 5) are focused on the top electrode of inverted OPVs. A lifetime study is presented, comparing a solution processed PEDOT:PSS hole transporting layer (HTL) with the evaporated MoO_3 HTL under 65°C in dark. The results show that devices using PEDOT:PSS as HTL are significantly more stable over time under heat conditions, compared to the devices using evaporated MoO_3 as HTL which are suffering from fast degradation. OPVs with PEDOT:PSS and MoO_3 as bi-layer HTL in different configurations were fabricated in an approach to isolate the interfaces and the degradation parameters. The results show that P3HT:PCBM/MoO_3 as well as MoO_3/Ag interfaces, contribute to the fast degradation of inverted OPVs with MoO_3/Ag as top

electrode. In addition, the above aspect was further enhanced by applying reverse engineering method in inverted OPVs with MoO_3/Ag as top electrode.

Based on the lifetime results of Chapter 4, PEDOT:PSS HTL was used in combination with IJP silver (Ag) for the development of a fully solution processed evaporation-free top electrode (Chapter 5). In inverted OPVs, silver top electrode can be deposited with printable deposition techniques compatible with roll to roll production line. A fully solution processed electrode is presented in inverted OPVs consisting of a highly conductive PEDOT:PSS and IJP Ag. Thick PEDOT:PSS layer was used in order to address the diffusion of solvents contained in Ag ink, into the active layer. It is proposed that highly conductive PEDOT:PSS assists in current collection of the printed electrode. Finally, a mixture of commercially available Ag inks with different nanoparticle sizes, was used in order to retain high conductivity, to control the printability and to achieve intimate interfaces.

TABLE OF CONTENTS

LIST OF TABLES

LIST OF FIGURES

LIST OF ABBREVIATIONS

AFM…….……...……...Atomic Force Microscopy

Ag.....Silver

Al.....Aluminium

ATO…….……Antimuonium Doped Tin Oxide

AZO……..……Aluminum Doped Zinc Oxide

BHJ…….…….…….……Bulk-heteronjunction

Ca.....Calcium

Cu……...…….Copper

CNT……..……..Carbon Nanotubes

DPPTTT…… ……..thieno[3,2-b]thiophene-diketopyrrolopyrrole

Eg.....Energy Gap

EG……...Ethylene glycol

ETL……...……..Electron Transporting Layer

FF……...…….……Fill Factor

FTO……..……..Fluorine doped Tin Oxide

HOMO…….....… Highest Occupied Molecular Orbital

HTL……...…….…….Hole Transporting Layer

ITO……....……..Indium Tin Oxide

IJP……..Inkjet Printed

J_{sc}…….…..Short Circuit Current Density

LiF.....Lithium Fluoride

LUMO……...…Lowest Unoccupied Molecular Orbital

Si-PCPDTBT……poly[(4,40-bis(2-ethylhexyl) dithieno[3,2-b:20,30-d]silole)-2,6-diyl-alt-(4,7-bis(2-thienyl)-2,1,3-benzothiadiazole)-5,50-diyl]

oDCB……...…… ….ortho DiChlorobenzene

OPV……...……Organic Photovoltaic

P3HT……...…….Poly- 3 - hexylthiophene

PCBM…….……...… Phenyl-C61-butyric acid methyl ester

PC[70]BM……[6,6]-phenyl C71-butyric acid methyl ester

PCE……...…...……Power Conversion Efficiency

PCT…….…….Photocurrent Mapping

PVs…….Photovoltaics

PEDOT:PSS……...…… Poly(3,4-ethylenedioxythiophene):poly(styrenesulfonate)

PEI……...polyethylenimine

PFN……..... poly[(9,9-bis(3′-(N,N-dimethylamion)propyl)-2,7-fluorene)-alt-2,7-(9,9-dioctyl)-fluorene])

PTB7……..Poly[[4,8-bis[(2-ethylhexyl)oxy]benzo[1,2-b:4,5-b']dithiophene-2,6-diyl][3-fluoro-2-[(2-ethylhexyl)carbonyl]thieno[3,4-b]thiophenediyl]]

SEM……Scanning Electron Microscope

V_{oc}……...…….Open Circuit Voltage

ZnO……Zinc Oxide

ISOS……..International Summit of OPVs Stability

ITIC……3,9-bis(2-methylene-(3-(1,1-dicyanomethylene)-indanone))-5,5,11,11-tetrakis(4-hexylphenyl)-dithieno[2,3-d:2’,3’-’]-s-indaceno[1,2-b:5,6-b’]dithiophene)

1. Introduction to Organic Photovoltaics

1.1.A brief history of photovoltaic systems

According to the International Energy Agency, world energy consumption will be increased by 28% by 2040 (International Energy Outlook 2017). This increases the need to use technologies utilizing renewable energy with the lower cost. Nowadays, the energy consumption and the elimination of the conventional energy sources, necessitates the use of renewable energy. Furthermore, due to the greenhouse effect, the global warming phenomenon is becoming more severe and therefore it makes necessary the use of green energy which is environmentally friendly. Sunlight is an ubiquitous form of energy and it can be considered as the most important source of energy on earth. By taking advantage of a small proportion of the abundant solar radiation, the energy demand on earth can be covered at a large degree.

Photovoltaic devices are taking advantage of solar energy by converting energy of solar light directly into electricity by the photovoltaic effect. The photovoltaic effect was invented by the French scientist Edmund A. Becquerel in 1839, when he observed the platinum plates coated with silver chloride or silver bromide inserted in acidic solution, to produce electricity under illumination.[1] In 1876 Adams and Day discovered the photoconductive effect when they observed electricity production from selenium while being exposed to sunlight.[2] The above inventions led to the formation of the first selenium photovoltaic cell in 1883 produced by Fritts.[3] This was the beginning of the technological developing world of solar photovoltaics that promote the magical idea of converting solar light into electricity. The efficiency of photovoltaics (PVs) was very poor until the beginning of 1950s. The first silicon based solar cell was produced in Bell Telephone laboratories with power conversion efficiency of 6% in 1954 by Chapin D. M. et al.[4] Due to their high cost, the initial applications of PVs were limited to aerospace industry and later in small devices such as calculators, radios, watches and other small battery charging devices. However, due to the energetic crisis in 1970s while the Earth's oil reserves would have run out and the energy demand would have been multiplied, increased public awareness about renewable energy sources. Over the next years there was a significant development of this technology aiming for high efficiency, long stability

and manufacturing cost reduction. Furthermore, significant efforts have begun on PV development for residential and commercial use.

The first generation of photovoltaics is based on single crystalline and multi-crystalline silicon. Silicon based photovoltaics are the most commonly used and well-studied PV technologies. Nowadays, the power conversion efficiency of single crystalline and multi-crystalline silicon is 27% and 22% respectively with 15-20 years lifetime manufacturer warranty.[5] Thin film PVs such as Cadmium tellurite (CdTe) and Copper Indium Gallium Selenide (CIGS) constitute the second generation of PVs. They are less costly per watt than 1st generation PVs due to the reduced material and energy consumption during manufacturing. The third generation PVs were designed to combine advantages from 1st and 2nd generation PVs. Dye-sensitized, quantum dot, perovskite and organic solar cells are technologies subjected to the third generation of PVs. The energy consumption for manufacturing 3rd generation PVs is reduced dramatically compared to the other two generations. In addition, thickness of 3rd generation PVs could be reduced to less than 1 μm allowing product development opportunities for flexible and lightweight PVs.

1.2. Organic Photovoltaics (OPVs)

Organic materials are constituted from carbon which is an abundant source on earth. Therefore, photovoltaics constituted by organic materials that are significantly cheaper than inorganic materials aim to a dramatic fabrication cost reduction. The first organic compound in which photoconductivity was observed is anthracene, as indicated by Pochettino and Volmer in 1906 and 1913, respectively. Remarkable progress in organic photovoltaics (OPVs) has been made in 1970s. OPVs with power conversion efficiencies far below 1% have been fabricated. For the interest of the reader, review article in organic solar cells by Chamberlain G.A. in 1982, is recommended. The first remarkable two-layer (bi-layer) organic solar cell with around 1% power conversion efficiency was fabricated by Tang in 1979.[6]

In 2000, Alan J. Heeger, Alan G. MacDiarmid and Hideki Shirakawa were awarded with the Nobel Prize in Chemistry for the discovery of organic semiconducting polymers in 1977.[7] With simple words, they discovered that plastic with suitable impurities can present semi-conductive properties. This discovery broke the myth that plastics are insulators of electricity and simultaneously begun a revolution in the world of electronics.

The combination of the very good mechanical properties of plastics with the semiconducting properties have developed new opportunities and prospects in manufacturing flexible, lightweight and low-cost electronic devices. As a result, organic photovoltaics have attracted the attention of the research community and companies due to the ease of manufacturing with simple deposition techniques at room temperature. Furthermore, the low cost and the ability to fabricate ultrathin, lightweight and flexible photovoltaics make them even more attractive and set them as emerging technology.

The next important invention was the mixing of polymeric organic semiconductor with a fullerene derivative by Heeger A.J. et al in 1995, resulting in the well-known bulk heterojunction active layer structure which is used until today. Nowadays, the best certified reported OPVs efficiencies are based on the so-called bulk heterojunction (BHJ) architecture, where the active layer is consisted of a blend of a conjugated polymer (electron donor) and a fullerene derivative (electron acceptor). The last two decades OPVs are under the spotlight of researchers, and the power conversion efficiency (PCE) and the lifetime performance of OPVs are continuously improving. Up scaling of this technology should combine high efficiency, long lifetime and low-cost printing manufacturing. Recent progress in BHJ OPVs overcame the barrier of 10% certified power conversion efficiency (see Figure 1.1).[8] In addition, the promising progress of the lifetime performance of OPVs during the last years resulted in OPVs with 2-4 years stability.[9] However, this technology demands low-cost manufacturing in order to make their commercialization more realistic. One of the next important research and development OPV milestones toward up scalability is considered to be the avoidance of energy consuming deposition techniques and thereby high cost materials. This thesis focuses on solution processed electrodes which is a key parameter for the roll to roll fabrication of OPVs.[10]

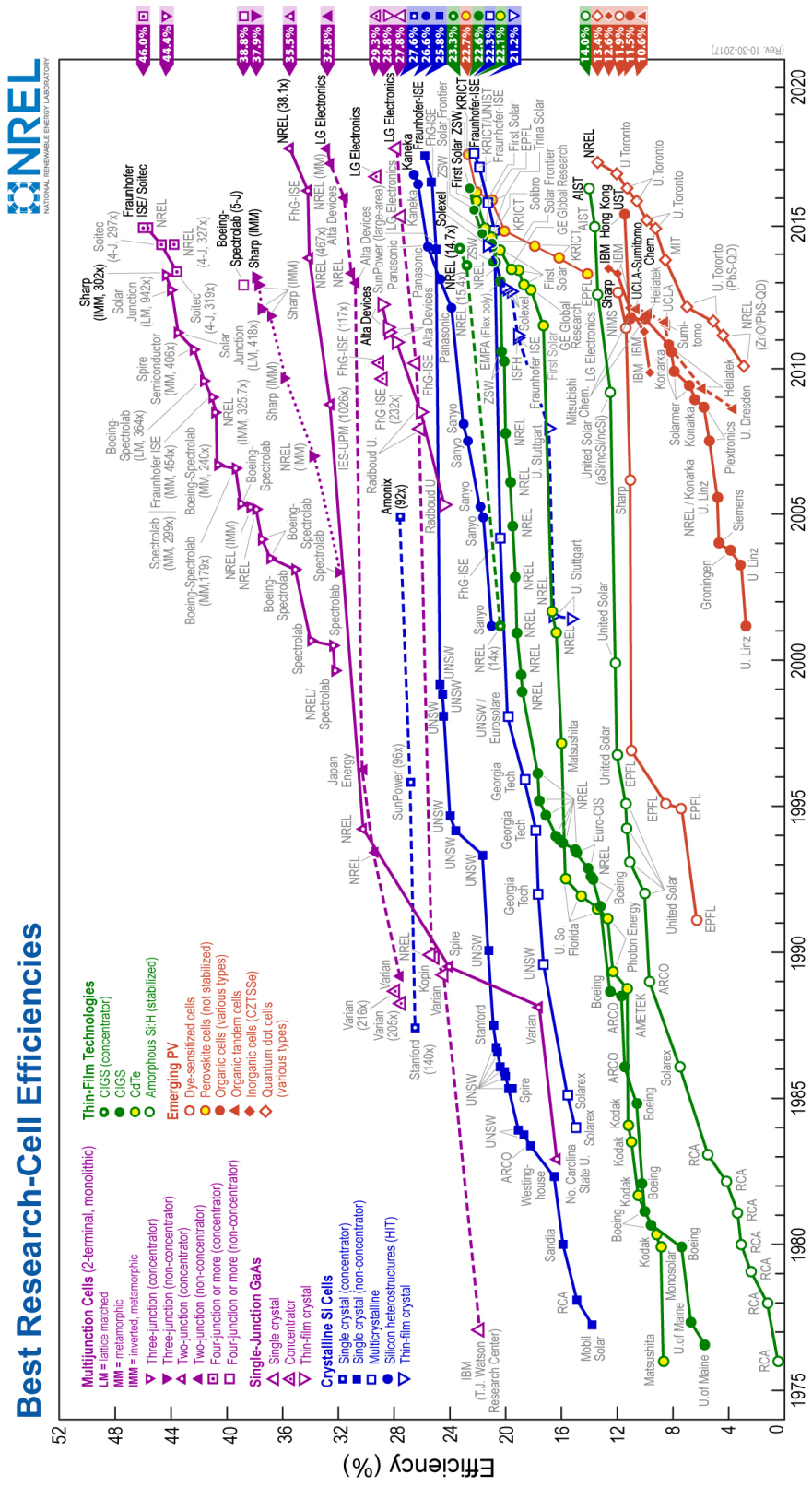

Figure 1.1: The line graph shows the on record certified by National Research Laboratory (NREL) cells power conversion efficiencies for various photovoltaic cells since 1975 (Figure was adopted from NREL National center of photovoltaics)

1.3. Historical evolution of OPVs active layer structure

1.3.1. Single layer structure

The active area of the first organic solar cell structure was consisted of a single layer of organic semiconductor, sandwiched between two electrodes with different work functions (Figure 1.2 image in left). The bottom electrode is a transparent conductive oxide in order to allow the solar radiation to pass through it and reach the active area. The top electrode is a low work function metal such as Al, Ca, Mg, Ca/Al, LiF/Al. The active region, which is the organic semiconductor, absorbs light and an electron is excited from the valence band to the conduction band. As a result, an exciton is formed. The exciton is a pair of an electron and a hole bonded together with Coulomb bond. An electric field is created due to the difference between the work function of the two electrodes but is rarely sufficient to break the bond of the exciton created in organic semiconductors. The excitons diffuse along the polymer chain with a diffusion length of 10-20 nm.[11] Therefore, the only excitons dissociation in this structure occurred in the area of 10-20 nm of the upper electrode. As a result, this structure was suffering from high exciton recombination rates and therefore low power conversion efficiencies in the range of 0.1 % were achieved.[12] The challenge raised from this structure was to overcome this limitation by finding more efficient mechanisms of exciton dissociation.

1.3.2. Bi-layer structure

The bi-layer structure (Figure 1.2 image in the middle) in which the active region was consisted of two organic materials, an electron donor and an electron acceptor, was developed in 1979. An electrostatic field sufficient to break the bond of the exciton was created at the interface of the two materials. The exciton diffusion length is about 10-20 nm and therefore the exciton dissociation occurred at 10-20 nm above and below the interface of both materials. This structure was more efficient in excitons dissociation than the single layer structure. Thus, the power conversion efficiency was increased about 10 orders of magnitude and reached 1 % efficiency.[13]

1.3.3. Bulk Heterojunction

The first bulk heterojunction structure was developed in 1995 and brought a revolution in the field of organic photovoltaics. Bulk heterojunction is the dominant active layer

structure used in OPVs until today. The active area consists of a blend of an electron donor and an electron acceptor in order to increase the interfaces between the two materials (Figure 1.2 image in right). In this structure the excitons that are generated in the electron donor material have more possibilities to reach the electron acceptor in their diffusion length range. In the interface of both materials, an electric field is created to split the exciton sufficiently into free carriers. In the first bulk heterojunction structure, the semiconductive polymer poly (2-methoxy-5-(2-ethyl-hexyloxy)-1,4-phenylene vinylene) (MEH-PPV) was used as the electron donor and the fullerene [6]-phenyl-C61 butyric acid methyl ester (PCBM) as the electron acceptor.[14] As a result, the donor-acceptor interfaces lead to more efficient exciton dissociations, overcoming the barrier of 1% efficiency. The morphology of the active layer blend has a major influence on the exciton dissociation efficiency. The annealing temperatures, the drying of the film, the choice of solvents and additives are some of the most significant factors determining the final bulk heterojunction morphology.[15–18]

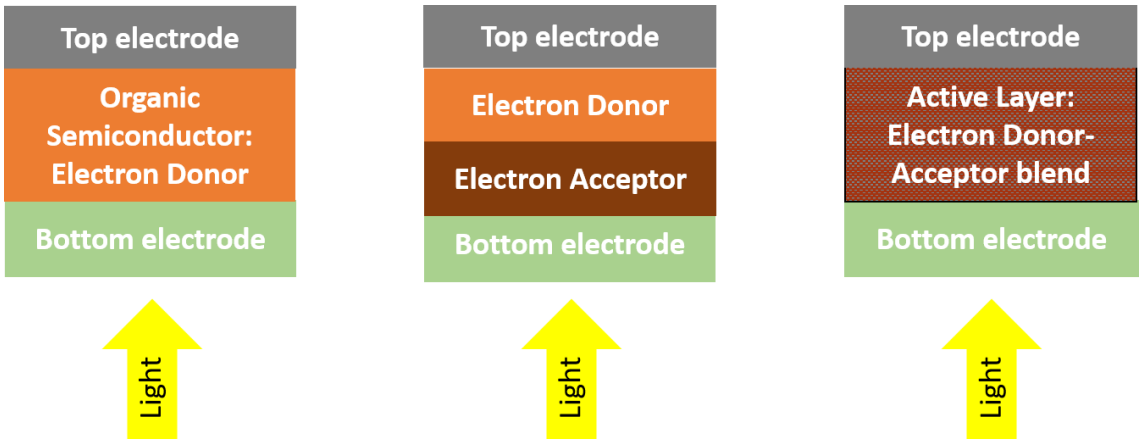

Figure 1.2: Single layer, Bi-layer and Bulk Heterojunction structure

1.4. Working principle of OPVs

As previously mentioned, the most widely used active layer structure is the Bulk Heterojunction where the active area is a blend of an electron donor and an electron acceptor. The Bulk Heterojunction structure replaced the bi-layer structure in order to increase the interfaces between electron donor and acceptor for more efficient exciton dissociation.

Organic semiconductors absorb photons efficiently due to their high absorption coefficient and thus active layer thickness of only some hundreds of nanometers is enough to absorb all the light at its maximum absorption spectrum. Photons with energy equal or greater than the energy gap are absorbed by the photoactive film which is the organic semiconductor (electron donor). An electron is excited from the highest occupied molecular orbital (HOMO) to the lowest unoccupied molecular orbital (LUMO) of the conjugated polymer. Then the exciton, which is a pair of an electron and a hole held with Coulomb bonds, is created. The electron and the hole are bonded together much more strongly than in inorganic semiconductors, due to the low dielectric constant of the organic semiconductor materials. Therefore, a lot of energy is needed in order to break the bond of the exciton. If an exciton finds the electron acceptor in the length less than the exciton diffusion length (~10-20 nm) then the electron moves from the LUMO of the donor to the LUMO of the acceptor.[19][11] Due to the potential difference (LUMO of donor - LUMO of acceptor) of the donor-acceptor interface an electrostatic field is created and the exciton dissociation is occurred. At this point, the electron and the hole are still retained with Coulomb bonds, however they are weaker (polaron pair). This is caused due to the formation of intermolecular energy states in donor-acceptor interface (Charge Transfer States).[20] In this intermediate state, the exciton will be either recombined or get completely separated into free charges (electrons and holes) which can then move to their corresponding electrodes. Recombination of charged carriers should be minimized for an efficient charge separation.

Dissociation of the exciton occurs when the generated electrostatic field is sufficient to break the bond of the exciton. This force is theoretically defined by the difference of the LUMO level of the donor and the LUMO level of the acceptor.[21] If the electric field

between LUMO of donor and LUMO of acceptor is big enough to overcome the exciton binding energy (200-500 meV) then the exciton will split into free carriers.[22]

Electrons move along the electron acceptor and they are finally collected by the cathode. The positive charged carriers (holes) are left in the HOMO of the electron donor and are collected by the anode. Between electrodes and active layers, interfacial layers (buffer layers) are commonly introduced in order to favor the charge selectivity and carrier transportation to the respective electrodes.

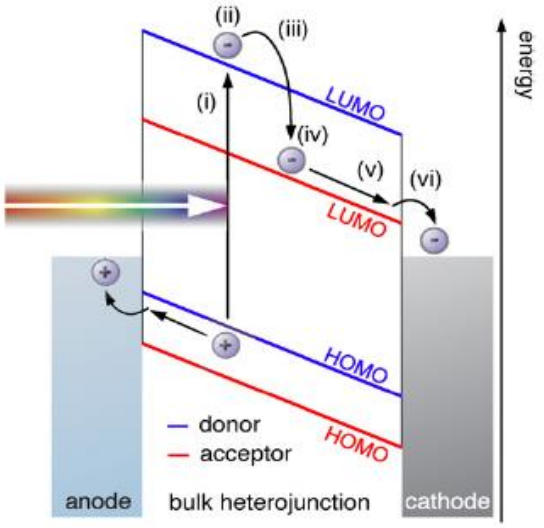

Figure 1.3: **(i) Electrons from the energy level HOMO of the donor go to the energy level LUMO of the donor (ii) singlet exciton creation (iii) separation of the exciton by the transfer of the electron from the energy level LUMO of the donor to the energy level LUMO of the acceptor (iv) polaron pair (v) separation of the polaron pair due to the electric field and charge transportation by hopping process to the local energy states (vi) charge collected from the electrodes: photocurrent. (Figure adopted from Deibel C. and Dyakonov V., reference [13])**

1.5.Device Architectures

In normal structure, the electrons are collected from the top electrode (Al) and the holes from the bottom electrode (ITO/Hole Transporting Layer). The top electrode is consisted of low work function metals such as aluminum (Al) which is relatively unstable and prone to moisture and oxygen.[23,24] However, if the polarity of the electrodes is inverted, the cathode and the anode are flipped. This configuration is called inverted structure. In inverted OPVs, the electrons are collected from the bottom electrode (ITO/Electron

Transporting Layer) and the holes from the top electrode (Hole Transporting Layer/Metal) allowing the use of air stable high work function electrodes such as silver (Ag) or gold (Au). Inverted OPVs present prolonged lifetime stability compared to the normal structured OPVs.[25] Furthermore, inverted OPVs provide technological opportunities due to their design flexibility. The Ag electrode can be deposited with printed techniques lowering the fabrication cost of OPVs, as will be shown in more details in Chapter 5 of this thesis. Due to the aforementioned advantages, inverted structure is more preferable and has attracted more scientific interest during the last years.[26]

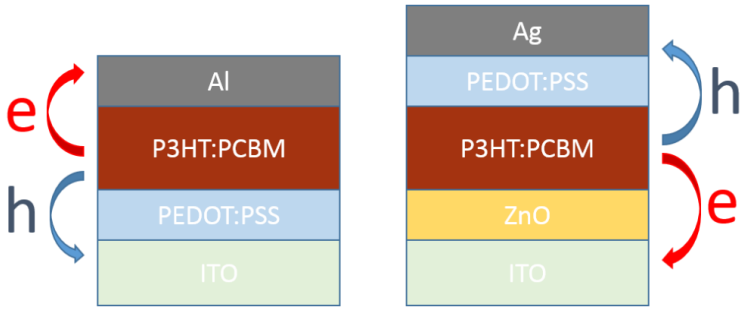

Figure 1.4: **Normal structure (Left) OPVs and Inverted structure OPVs (right)**

1.6. Lifetime of OPVs

The three main pillars for OPVs commercialization are power conversion efficiency, manufacturing cost and lifetime performance. OPVs device stability is affected by chemical and physical modifications. Chemical degradation arises from interactions between two materials or components resulting in chemical structure alterations. Physical modifications are associated with structural modifications. Both types of modifications are caused by external and internal factors. External factors are oxygen, moisture, temperature, light and mechanical stress. Internal factors are associated with chemical modifications. External factors may accelerate chemical modification. For instance, temperature can cause thermal diffusion at interfaces and morphological evolution of active layer. Light can accelerate both chemical and physical modifications. Light can induce heat affecting physical modification. In addition, light can also cause photodegradation and accelerate the reaction of oxygen within the device, affecting chemical modification. [27–29]

The research community has established standardized lifetime protocols in an effort to have reliable lifetime data comparison and thus more understandable degradation mechanisms under different environmental stress factors. These regulated lifetime test procedures are called ISOS which stands for a dedicated annual session on OPVs stability, named International Summit on OPVs Stability. ISOS standards are divided in five main testing categories: dark (ISOS-D), outdoor (ISOS-O), laboratory weathering (ISOS-L), thermal cycling (ISOS-T) and solar-thermal-humidity cycling (ISOS-LT). Each of the above categories is subdivided in three stages depending on the level of testing. The three test protocol levels are basic (Level 1), intermediate (Level 2) and advanced (Level 3) and are defined according to the equipment, the conditions and the range of parameters. For the interested reader, more details of the ISOS protocols can be found in Reese M.O., et al..[30] In Chapter 4 of this thesis ISOS-D-2 protocol (65°C, ambient humidity) was used to examine useful information about the degradation mechanism of non-encapsulated inverted OPVs comparing a solution processed with an evaporated hole transporting layer.

The diversity between the deposition processes, the materials, the device structures, the device geometries, the encapsulation types and the ageing mechanisms, can cause diversity of degradation patterns among reported lifetime data. In addition, the lack of experience on lifetime performance of OPVs does not allow to predict their durability based on the accelerating testing, and therefore the establishment of pass-fail tests either. Again, OPV community set lifetime parameters on frequently obtained patterns as an approach to identify better the lifetime data reported in the literature.[30] Professor's Krebs F. group has demonstrated a statistical approach for analysing various OPV samples under different stress factors based on ISOS protocols.[31] Their average lifetime was determined and the ratio between the accelerated and real outdoor test was calculated. The same approach was used for analysing the entire literature lifetime data and potentially to be used in order to predict the lifetime of OPVs.[32,33]

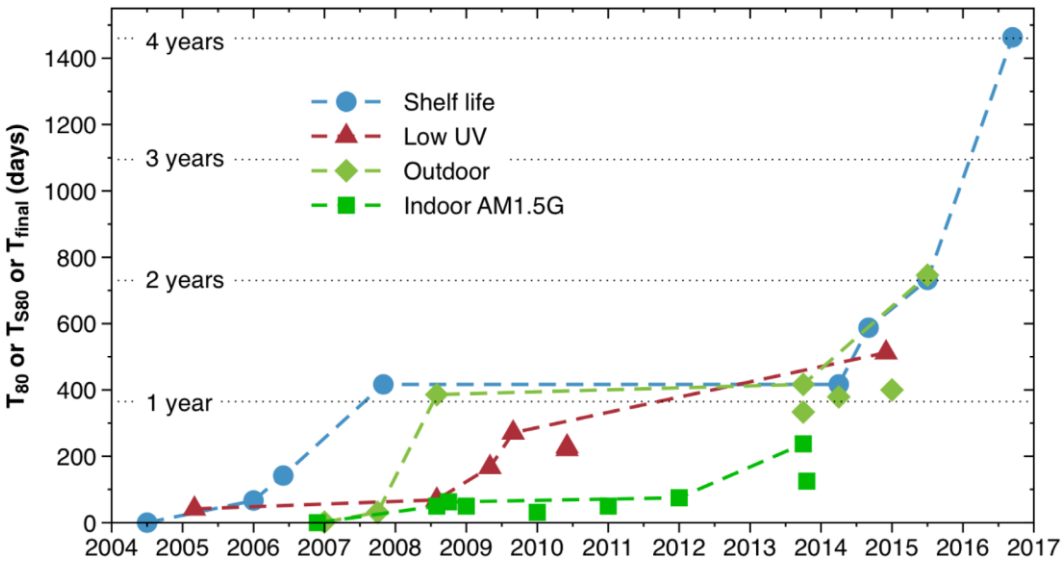

Figure 1.5: Diagram of the best OPV lifetime values according to the test condition (T_{80} : time when performance reaches 80%, T_{final}: used when study was interrupted before OPVs reach T80). (Figure adopted from Gevorgyan, et al., reference [29])

The last years, a lot of progress has been made in the lifetime performance of OPVs, and OPVs with shelf life stability of up to four years now exist (Figure 1.5).[29] Despite the progress in lifetime performance in OPVs compared to the early stages of this technology, stability of OPVs remains one of the main bottlenecks to push this technology to the market.

2. OPVs Materials, Performance Parameters and Fabrication Methods

2.1.Materials for organic solar cells

2.1.1. Material for electrodes

The reflective top metal electrode of OPVs is usually thermally evaporated. Normal structure OPVs use aluminum (Al) and inverted structure OPVs silver. Indium tin oxide (ITO), is the most widely used transparent conductor in OPVs and in other optoelectronic applications in general. Its high transparency (>90%) and low sheet resistance values (4-30 Ω/sq) are the two key parameters of its extensive usage as the transparent electrode. However, it is deposited with sputtering technique which requires vacuum and high amount of energy, incompatible with solution processing and roll to roll manufacturing. Furthermore, its high cost (indium is rare mineral) and brittleness make it incompatible for cheap, printable and flexible electronic applications.[34] Other vacuum deposited transparent conductive oxides that fulfill the bottom electrode requirements are fluorine doped tin oxide (FTO) and aluminum doped zinc oxide (AZO).[35,36] Multilayer electrodes, and more specifically a thin metal layer sandwiched between two dielectrics (metal oxide-metal-metal oxide), attracted much attention as a replacement of ITO transparent conductor since they provide the possibility to use cheap and abundant elements.[37–39] However, vacuum deposition and energy intensive techniques tend to be the Achilles heel for the mass production of OPVs. Therefore, the use of solution processed electrodes could be the key for realizing low cost mass production photovoltaics. Many efforts have been made for solution processing both the bottom and top contacts. Solution processed ITO-free electrodes constitute an emerging topic toward commercialization of flexible electronic applications. Highly conductive PEDOT:PSS, metal nanowires, carbon-based materials and metal nanoparticles are the most promising candidates reported in the literature.[40–47]

Metal nanowires and especially silver nanowires have attracted tremendous interest as a replacement of ITO transparent electrode due to their fascinating mechanical, optical, electrical and solution processable properties. In addition, nanowires attracted the attention of industry due to aesthetic reasons in contrast to metal grid designed electrodes. Critical parameters that affect the performance of metal nanowires are the aspect ratio,

the size uniformity, the density, the smoothness and the purity. Transparency is achieved through the formation of percolation network due to the low diameter of nanowires which is usually less than 100 nm and the high aspect ratio which is higher than 100. Metal nanowires can be dispersed in polar solvents and deposited with all solution processing techniques such as spray coating, spin coating, doctor blade and inkjet printing.[47–50] The most commonly reported sheet resistance and transmittance values in the literature are 10-100 Ω/sq and 80-90% respectively.[51,52] OPVs utilizing this material has already demonstrated high performance either used as bottom, either as top and either as both solution processed electrodes.[42] OPVs with efficiencies comparable to those with ITO electrode were achieved. Furthermore, it has been demonstrated that silver nanowires are more bending durable than ITO in flexible OPVs.[48] Nevertheless, the stability and the synthesis of well controlled length and consequently the conductivity of silver nanowires should be addressed for further application. Copper nanowires are significantly cheaper and can provide nearly the same conductivity with silver nanowires. However, they are sensitive to oxygen and moisture leading to reduced conductivity due to copper oxidation.[53] An effective method to reduce the oxidation reactivity is the coating of an inert shell with noble materials such as silver and nickel. However, the complexity of the processing of such synthesis limit their further development.

Recently, carbon-based materials (graphene, graphene oxide, carbon nanotubes) attracted a lot of attention from research community. The discovery of graphene offered advantages for the application of flexible electronics. The theoretical high electrical conductivity (sheet resistance of 6 kΩ/sq) and light transmittance (97.7%) of a single graphene lead to extensive research of this material as a transparent conductor.[54] However, films deposited in real are never identical. The formation of graphene can be obtained with chemical vapor deposition and mechanical cleaving.[55,56] This is the main bottleneck of this material since the mentioned techniques are not compatible with low-cost mass production photovoltaics. On the other hand, graphene oxide has shown strong potential for mass production of flexible transparent electrodes since it can be dispersed in polar solvents providing versatility in solution processability of this material.[57] The electrical conductivity of graphene oxide is relatively poor, but it can be improved by thermally or chemically reduced process resulting in graphene-based material providing sheet resistance values ranging from 0.2-1 kΩ/sq.[56]

The single Carbon NanoTube (CNT) has amazing electrical properties (conductivity of $3x10^4$ S/cm and mobility 100000 cm^2/Vs).[58] However, when single CNTs come in contact to form a CNTs network their conductivity is significantly affected from the contact resistance between CNTs which depends on the CNT length, diameter, synthesis and purity. The reported sheet resistance values of CNTs networks in the literature are in the range of 200-300 Ω/sq with 80% transmittance at 550 nm.[59–61] It is worth noting that the current values are not competitive to those of ITO. Similarly to graphene, a major challenge is their poor dispersion due to their high affinity for each other caused by Van der Waals interactions. In addition, their high roughness could be considered as another obstacle for their use as transparent electrodes.

The relatively good processability and unique optoelectronic properties of PEDOT:PSS conductive polymer make it one of the alternative ITO-free solution processed electrode. The conductivity of PEDOT:PSS (0.001-4000 S/cm) is continuously improved by various approaches. Numerous studies showed that a treatment with acids or polar solvents leads to partial removal of the insulating PSS and promotes the polymer chains to a linear-extended coil alignment resulting in enhanced interchain mobility and conductivity.[62–65] Kim et al used concentrated H_2SO_4 to treat PEDOT:PSS and achieve 4380 S/cm conductivity (50 Ω/sq sheet resistance) which is the highest reported value in the literature. OPVs with PCEs comparable to those with ITO electrode were achieved.[66] However, treatment with strong acids doesn't meet the requirements of a mass production transparent electrode since they can cause safety and environmental issues. Despite the improved conductivity values of treated PEDOT:PSS, they still don't meet the requirements for a transparent electrode (10 Ω/sq and >85% transparency). The limited conductivity and high sheet resistance of PEDOT:PSS lead to OPVs with high series resistance values and thus lower performance. The high series resistance limits the use of PEDOT:PSS as electrode in large area OPVs. In addition the long term stability of PEDOT:PSS is an issue since is vulnerable to high temperatures and humidity.[67,68] Therefore, further optimization of this material is needed in terms of conductivity and stability for its wider usage as transparent conductor.

Metal grids combined with PEDOT:PSS as the bottom transparent electrode significantly decrease the resistance of the anode and overcome the resistance limitations of PEDOT:PSS as a sole electrode.[69] Metal grids provide areas fully covered with high

conductivity and areas fully transparent, and in combination with the PEDOT:PSS constitute the transparent electrode. Metal grid can be formed with thermal evaporation through micro structured mask, lithography or by printing metal nanoparticle inks.[70–73] The latter is a prerequisite for solution processed OPVs. Metal nanoparticles' size is ranging from one to several hundred nanometers. In addition, the high surface to volume ratio results in increased surface energy and low melting point. The metal nanoparticles can be formed with various synthetic methods and they can be dispersed in solvents. Therefore, they can be deposited with printing techniques such as flexographic, screen and inkjet printing. The ink could be designed by careful choice of solvents, binders and additives to meet the deposition technique requirements.[74] Sintering of the metal nanoparticles is required in order to provide the desired percolation network paths for electrical conductivity. The most commonly used sintering methods are the thermal, laser, photonic, chemical and microwave sintering.[75–79] The applied energy melts nanoparticles and merge them. This results in a conductive connected network achieving 10-30 % of the bulk conductivity of the metal.[80] Metal nanoparticles have been used for the design of both electrodes, the bottom transparent electrode and the top electrode.[81–85]

For the bottom transparent electrode with Metal grid/PEDOT:PSS, an optimization is needed for the metal covered area depending on the metal grid and PEDOT:PSS conductivity (compromise between resistive and shadowing losses). Furthermore, studies comparing different grid geometries and line morphologies were also reported.[86,87] From our previous work, the optimization of inkjet printed Ag grid was established in detail, consisting of lines with 200 nm height and 45-50 μm width, as bottom electrode in OPVs. Two-step thermal sintering process was applied to control the line morphology and achieve the desired conductivity and desired adhesion of Ag on glass substrate.[79,88] OPVs using Ag lines grid and PEDOT:PSS as the bottom electrode achieved comparable efficiency with those of ITO-based device as shown in Figure 2.1.

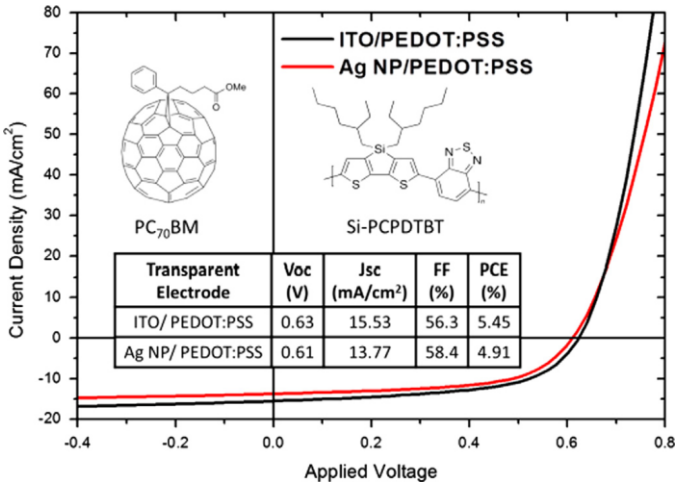

Figure 2.1: Performance characteristics of OPVs with 8-line grid/PEDOT:PSS in comparison with the ITO-based device (Neophytou et al., reference [79])

Cu nanoparticle inks could provide similar conductivity with Ag nanoparticle inks and since they are significantly cheaper they could further reduce the fabrication cost of OPVs. More details about ITO-free OPVs based on IJP Cu grid will be followed in Chapter 3 of this thesis which demonstrates IJP Cu nanoparticles as a replacement of ITO bottom electrode. In addition, Chapter 5 demonstrates inkjet printed Ag nanoparticles as evaporated free top contact in inverted OPVs.

2.1.2. Photoactive materials

Nowadays, the bulk heterojunction structure which is a blend of an electron donor and an electron acceptor is used as the active layer of OPVs. Donor materials are usually conjugated polymers where the most widely used is P3HT. Research community synthesizes various polymer donors in order to improve the device efficiency and the lifetime performance of OPVs.[89]

Fullerene derivatives are used as electron acceptors in the active layer blend. Over the last years, fullerene derivatives tend to be replaced by polymeric acceptors in order to reduce the cost and increase the efficiency and stability of OPVs.[90,91] Some of the highest reported PCEs in the literature are using newly developed acceptors such as ITIC and IDTBR.[92] Furthermore, combination of polymer acceptors with small amount of fullerene acceptors (ternary blends) have been used for further improvement on the efficiency of the device.[93]

It should be noted that the purpose of this thesis is not to produce high record PCEs but to focus on the electrodes of OPVs. As a result, well-studied materials were used as electron donors and acceptors. The materials used in this work as electron donors for the active layer are Si-PCPDTBT in Chapter 3, P3HT, DPPTTT and PTB7 in Chapter 4 and P3HT in Chapter 5. PC[60]BM and PC[70]BM were used as electron acceptors.

2.1.3. Hole and Electron transporting materials

A hole transporting layer (HTL) and electron transporting layer (ETL) are used in order to provide hole or electron selectivity of the contacts. These interfacial layers are rensposible for reasonable functions: (1) Tuning of the energy level alignment of the electrode/active layer and thus facilitating better Ohmic contact formation of the electrode/active layer. (2) Define the polarity of the electrode and hence the device architecture (normal or inverted). (3) Control surface properties to alter the morphology of the active layer. (4) Improve charge transport by favoring exciton dissosiation, charge extraction and minimizing recobination rates. (5) They are also used as optical spacers and plasmonic effects to enhance light absorbption of the active layer. In addition, these interfacial layers are usually used to improve the stability of OPVs by prohibiting chemical or physical reaction between the polymer and the electrode.[94]

HTL is characterized by a good hole mobility. The energy level of HTL should align with the HOMO level of the donor and act as electron blocking layer. The conjucated polymer PEDOT:PSS is the most widely used and studied HTL. PEDOT:PSS with different conductivities, wetting properties, acidity and optoelectronic properties were developed and widely used to serve several roles in OPVs. Despite the extensive usage of this material, devices using PEDOT:PSS are vulnerable to humidity due to its hygroscopic nature.[95] In addition, acidity of PEDOT:PSS proved detrimental for the stability of normal structured OPVs.[96,97] The replacement of this material is still a challenging task in terms of device stability. V_2O_5, WO_3, and MoO_3 are some oxide materials used in order to replace it. A lifetime study under heat conditions comparing an evaporated MoO_3 and a solution processed PEDOT:PSS is exhibited in Chapter 4 showing that the solution processed PEDOT:PSS HTL exhibited significantly better lifetime performance than MoO_3 HTL.

Calcium and Lithium Fluoride are usually used as electron selective layers in normal structured OPVs, however their high reactivity with air limit OPVs lifetime performance. TiOx and ZnO are extensievly used as electron transporting layers (ETL) in inverted OPVs. Such metal oxides can be deposited with thermal evaporation or sputtering under vacum. However, as already mentioned, thease techniques are not suitable for upscaling fast production of OPVs. Solution processed oxides were developed using low temperature solution processed methods and used in OPVs elctrode configurations.[98] Doping of these oxides with other metal elements can alter their workfunction alowing band alignment regarding electrode configuration and active layer materials. In addition, doping provide higher conductivity values and therefore thicker oxide layers could be used providing flexibility on deposition of this layer with upscaling roll to roll techniques.[99,100]

2.2. OPV Performance Parameters

The performance and other important parameters of a solar cell device are characterized by Current-Voltage (JV) curves which are obtained under dark and under illumination. A JV curve is plotted when external bias (negative-positive) is applied to the device and the produced current is pointed to the corresponding value of voltage. The cell can be considered as a two terminal device which conducts like a diode in the dark and generates a photo-voltage when illuminated by the sun.

The solar cell is illuminated by the solar simulator which emits simulated sunlight of an air mass 1.5 G spectrum at a power output per incident area of 100 mW/cm^2 (one sun). This process is done in order to have comparative efficiency results from all around the world.

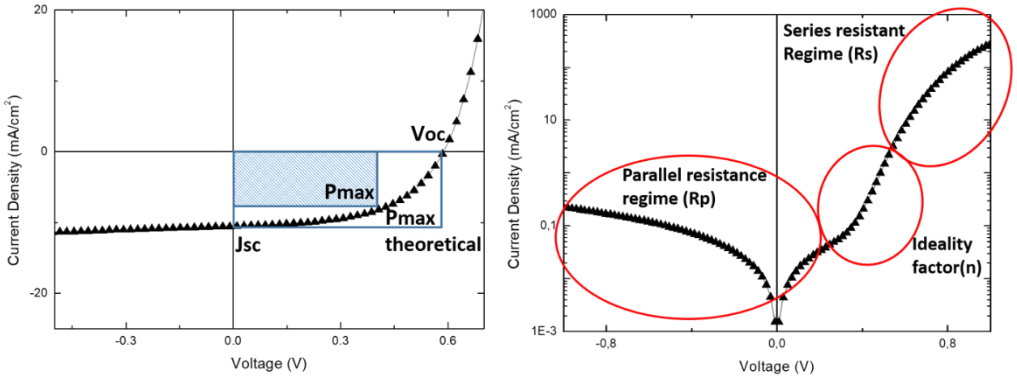

Figure 2.2: (a) Current density (J) vs Voltage (V) characteristics under illumination of an organic solar cell (b) Dark current density vs Voltage characteristics

From the illuminated Current-Voltage (JV) curve which is illustrated in Figure 2.2a four parameters, which determine and characterize the efficiency of a solar cell, can be obtained. These parameters are the short circuit current density (J_{sc}), the open circuit voltage (V_{oc}), the fill factor (FF) and the power conversion efficiency (PCE).

The solar cell in dark conditions acts as a diode and the JV curve (Figure 2.2b) which is obtained under dark conditions can provide other significant characteristics: the parallel resistance (R_p), the ideality factor (n), and the series resistance (R_s). The R_p arises from leakage of current (the current which flows in the opposite direction of the current flow) through the device and appears at low-negative voltages. Technically at these voltages ($V<0$) the device acts as a photodetector consuming power to produce photocurrent. R_p is determined by the quality of the films and the interfaces. R_p is limited by leakage current through pinholes in the device and carrier recombinations during their transfer at the electrodes. At $V>V_{oc}$ region (R_s region) again the device consumes power. R_s arises from the resistance of the materials and the interfaces in the vertical direction of the device, in the direction of the current flow, and appears at high positive voltages (see Figure 2.2b Region R_s). R_s is also determined by the conductivity of the electrodes. For an efficient solar cell, the R_p should be as large as possible and the R_s should be as low as possible. Both R_s and R_p affect the FF. The intermediate voltages (Region n) are characterized by the ideality factor (n) which is mainly influenced by the morphology of the active layer.

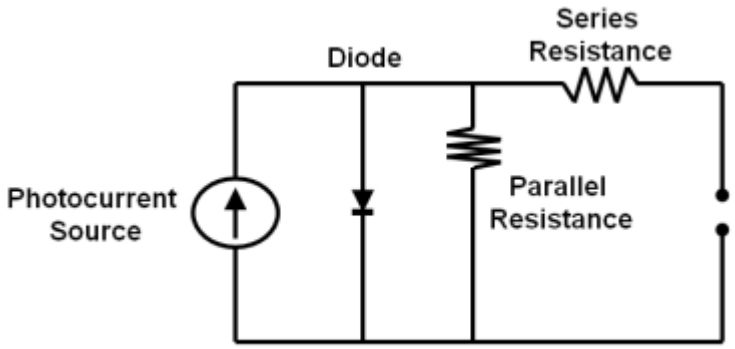

Figure 2.3: The equivalent circuit for an OPV

The equivalent electric circuit diagram of an OPV is also important for further understanding the function of a solar cell. The circuit consisting of four parts is illustrated in Figure 2.3. The photocurrent source represents the current generated by the absorption of light and subsequent carrier generation. The diode represents the excitons recombination at the interfaces. The series resistance represents the internal resistance of the solar cell in the direction of current flow. The parallel resistance represents the leakage current through the cell.

2.2.1. Short-circuit Current Density (J_{sc})

The short-circuit current density J_{SC} is the current density at zero bias (V = 0). The Jsc is influenced by the following factors. (1) Absorption efficiency (n_{abs}) which is determined by the overlap of absorption spectrum of the active layer and the solar spectrum, the light intensity and the thickness of the active layer. (2) Exciton dissociation efficiency (n_{diss}) which is determined by the active layer morphology and donor-acceptor interface. (3) Charge collection efficiency (n_{out}). **[21,101,102]**

$$\mathbf{Jsc} \sim \mathbf{n_{abs} \cdot n_{diss} \cdot n_{out}} \qquad \textbf{Equation 1}$$

The photo generated current is given from the equation below where is the exclusion of dark current (J_d) from short circuit current. Dark current is the current which flows in the device under dark under an applied voltage. J_d flows in the opposite direction of the photocurrent.

$$J_{ph} = J_{sc} - J_d \qquad \textbf{Equation 2}$$

2.2.2. Open Circuit Voltage (V_{OC})

The open-circuit voltage V_{oc} is the voltage across the solar cell when J = 0 (open-circuited device). This means that V_{oc} is the value when photocurrent generation and dark current are canceled out. V_{oc} is strongly affected by the difference of the HOMO of the donor and the LUMO of the acceptor, as indicated in Equation 3 where $q=1.6.10^{-19}C$ is the elementary charge, E_{LUMO} (acceptor) and E_{HOMO} (donor) are the energy levels of the acceptor LUMO and the donor HOMO respectively.[103] V_{oc} in OPVs is strongly affected from the donor-acceptor system and the morphology of the active layer blend.

$$qVoc \approx E_{LUMO}(\text{acceptor}) - E_{HOMO}(\text{donor}) \qquad \textbf{Equation 3}$$

2.2.3. Fill Factor (FF)

The Fill Factor (FF) is the ratio between the theoretical power $P_{max\ theoritical}$ (defined by J_{sc} x V_{oc}) and the maximum power (P_{max}) which is actually being produced. Due to the diode behavior and additional resistance and recombination losses, $|J_{max}|$ and V_{max} are always less than $|J_{SC}|$ and V_{oc}, respectively. Therefore, FF can be calculated from the equation below:

$$FF\% = \frac{P_{max}}{P_{\max\ theoritical}} = \frac{J_{max}V_{max}}{J_{sc}V_{oc}} \qquad \textbf{Equation 4}$$

Actually, the Fill Factor of a solar cell is the measure of the power that can be extracted from the diode. Higher FF values indicate higher maximum power obtained. Both serial (R_s) and parallel resistance (R_p) influence the FF.

2.2.4. Power Conversion Efficiency (PCE)

The PCE is the most important parameter of a solar cell device as it reflects how efficient a solar cell can convert light to electricity. PCE is the ratio between the power of incident light and the maximum power P_{max} that can be obtained from the particular device. P_{light} is constant at 100 mW/cm^2. The PCE is given by:

$$n = \frac{P_{max}}{P_{light}} = \frac{J_{sc}\,V_{oc}\,FF}{P_{light}} \qquad \textbf{Equation 5}$$

2.2.5. Quantum Efficiency (QE)

The external quantum efficiency (EQE) is defined as the percentage of photons hitting the device which are converted to electrons and collected by the terminals.

$$\boldsymbol{EQE}(\%) = \frac{\boldsymbol{Number\ of\ collected\ electrons}}{\boldsymbol{Number\ of\ incident\ photons}} \qquad \textbf{Equation 6}$$

Another useful value for better understanding of the OPVs performance is the internal quantum efficiency (IQE). IQE includes the absorption characteristics of the active layer whereas EQE does not and therefore significant information can be extracted. Internal quantum efficiency is defined as the ratio of the number of extracted charge carriers to the number of absorbed photons in the active layer.

$$\boldsymbol{IQE}(\%) = \frac{\boldsymbol{Number\ of\ collected\ electrons}}{\boldsymbol{Number\ of\ photons\ absorbed\ in\ the\ A.L.}} \qquad \textbf{Equation 7}$$

High percentage value of IQE indicates an efficient exciton separation, charge carrier transportation and charge collection.

2.3. Device Fabrication Methods

2.3.1. Doctor Blade

Doctor Blade deposition technique is a lab scale technique that could provide insight on the up-scalability of OPVs processing parameters since its working principle is similar to the slot die coating up scalable technique. It uses a small amount of material for large area surfaces and deposits high quality uniform layers in the direction of a moving blade. A specific amount of solution is applied either to the substrate surface or in the gap between the substrate and the blade according to high or low viscosity respectively. The blade moves at a speed set by the operator along the substrate and the solution is deposited on the entire surface of the substrate and dry due to the evaporation of the solvent. Both rigid and flexible substrates could be deposited using this technique. Parameters which affect the thickness and the quality of the film are the speed of the blade, the substrate temperature, the distance of the blade from the substrate, the volume, the concentration and the viscosity of the solution. In general, when the speed of the blade increases, thicker films are yielded. This technique was used for the deposition of most layers of this thesis as you will see in the next chapters.

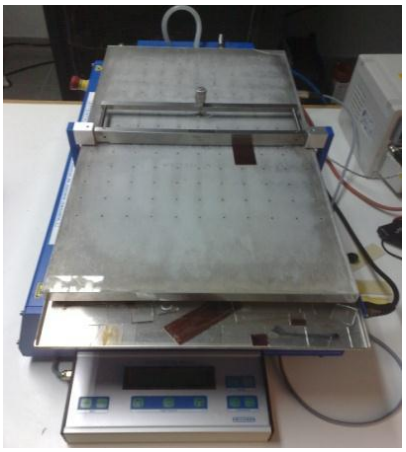

Figure 2.4: Doctor Blade

2.3.2. Roll to roll manufacturing

As previously mentioned, one of the three crucial commercialization aspects of OPVs is the fabrication cost. One of the most important privilege of OPVs is that the can be solution processed allowing deposition in ambient conditions via lower cost techniques. Roll to roll manufacturing enables high speed and low-cost fabrication of flexible lightweight photovoltaics. These are important parameters for commercialization and accomplishments of product development targets of OPVs. Roll to roll manufacturing could constitute a combination of various techniques such as slot die coating, spray coating, gravure, flexographic, rotary screen printing and flatbed screen printing. The interested reader can find extensive information about the aforementioned techniques elsewhere.[10,104,105] Slot die coating is a contactless deposition method in which the ink flows along a coating blade and it is retained between the blade and substrate by meniscus forces. The substrate is moving and the ink is deposited uniformly along the direction of the moving substrate. Slot die coating does not allow 2-D pattering of the coated film in contrast with other deposition techniques. One can say that slot die coating is an up scalable version of doctor blading technique which is extensively used in this thesis. However, there are a lot of limitations and challenges while transferring fabrication from lab-scale to up scalable techniques.

2.3.3. Thermal Evaporator

Thermal evaporator is responsible for the deposition of the reflective metal electrode of the device. It can deposit metals by evaporating them and thereby forms the top reflective electrode. The metal is placed in a boat which is located in a chamber that has to be evacuated to a base pressure of ~ 10^{-6} mbar. The vacuum which is achieved is sufficient to decrease the boiling point of most metals. Also, vacuum removes residual gases inside the chamber, preventing the evaporated metal atoms to collide or react with other foreign atoms. When the boiling point is reached the metal starts to evaporate. Then, the evaporated atoms rise up inside the evaporation chamber and condense to a solid state on the surface of a sample. The result is a uniform high-quality film and the thickness can be controlled by the evaporation rate. In addition, thermal evaporator can be used for the deposition of various materials such as metal, metal oxides and organic materials. However, it is an energy consuming technique and incompatible with roll to roll

manufacturing and therefore many research units try to find alternative methods to replace it.

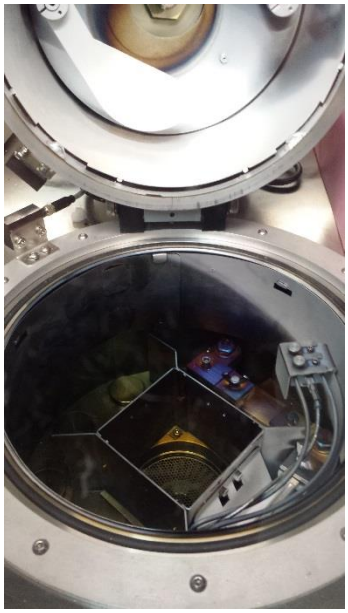

Figure 2.5: Thermal evaporator

2.3.4. Inkjet printing

Inkjet printing is a promising deposition method for organic solar cells due to its ability to deposit a specific volume of drop on a specific spot. This means that it allows the printing of two-dimensional patterns and high resolution/quality layers by controlling the processing. In addition, inkjet printing with drop on demand technology can save material and as a result, the overall fabrication cost can be reduced significantly. Inkjet printing is a contactless method, the print head does not come in direct contact with the substrate, and therefore it can print on a variety of substrates without damaging the underlying layers. Chapter 3 and 5 of this thesis are based on inkjet printing metal nanoparticles for the design of the bottom and top electrode, respectively.

This method is separated into two categories according to the droplet ejection. In the first category the droplets are continuously generated from one nozzle and a droplet jet is formed and electrostatically deflected into the desired area (continuous). This method is very fast, but the printing area is limited. In the second category, the droplets are generated and ejected from many nozzles and accelerated towards a specific spot on the

substrate (drop on demand). In contrast with the first method, this one has the capability to cover a greater surface due to the number of nozzles that it uses. The drop on demand technology is subdivided in three categories: piezoelectric, thermal and electrostatic. The piezoelectric method is the most commonly used since it is suitable to print various types of inks materials. The mechanical pressure is created through a piezoelectric crystal and an applied voltage based on the piezoelectric effect. Then the droplets are created and ejected through the nozzles on the desired spot. The droplet in thermal printing is created by a pressure formed by heating the ink. This method requires one of the ink compounds to have low boiling point solvent. For the electrostatic inkjet printing, an electrostatic field is applied between the nozzles, then the drop is charged electrostatically and it is ejected from the nozzles to the substrate. **[106]**

Figure 2.6: Dimatix 2800 series inkjet printer

The thickness of the printed layer can be controlled by printing several layers or by increasing the volume of the droplet on a specific spot. The latter can be controlled by the parameter called drop spacing. The thickness (d) of the inkjet-printed film can be calculated in the equation below:

$$\boldsymbol{d = \frac{N_d V_d c}{\rho}} \qquad \textbf{Equation 8}$$

Where N_d is the number of the droplets delivered per area (cm^{-2}), V_d is the volume of the droplets, c is the concentration of the solid material in the ink in g cm^{-3} and ρ is the density of the material in the final film in g cm^{-3}.**[105]**

The ink properties play a major role in the quality of the printable layer. They also define if the ink can be printed or not. To ensure if the ink is printable, the inverse (Z) of the Ohnesorge number (Oh) should be calculated.[107]

$$\boldsymbol{Z = \frac{(\alpha\rho\gamma)^{1/2}}{\eta} = \frac{N_{Re}}{(N_{We})^{1/2}}} \qquad \textbf{Equation 9}$$

N_{Re} is the Reynolds number which is the ratio of inertial to viscous forces. N_{We} is the Weber number which is the balance between inertial and capillary forces. The equations of the two numbers are illustrated below.

$$\boldsymbol{N_{Re} = \frac{\upsilon\alpha\rho}{\eta}} \qquad \textbf{Equation 10}$$

$$\boldsymbol{N_{We} = \frac{\upsilon^2 a\rho}{\gamma}} \qquad \textbf{Equation 11}$$

Where υ is the average velocity of the droplet, ρ is the density, γ is the surface tension, η is the viscosity of the fluid and α is the radius of the printing nozzle. Jang, D. et al. determine that a fluid with Z > 14 is not printable.[107]

The viscosity for jettable fluids should be 2-30 centipoise. Low viscosity is required for the ink to be jetted. Fluids with viscosity up to 30 centipoises may be jetted but their drop velocity limits the processing. Surface tension should be 30-60 dynes/cm to prevent dripping from the nozzles. Low surface tension is preferred in order to achieve desirable spreading of the ink and wetting of the substrate. In addition, low surface tension provides easy generation of a stream of droplets. The printable inks consist of many types of solvents. It is commonly known that for roll to roll manufacturing water-based solvents which are not harmful for human health are preferred (instead of aromatic and organic solvents).[108] Many works have shown that printing high quality of an active area blend should combine a mixture of two solvents, one with low and one with high boiling point. The low boiling point solvent compensates the drying rate of the printed film and the high boiling point solvent prevents nozzle clogging.[105,106]

Crucial printing parameters in the printing of high quality layers of specific thickness using an inkjet printer are the temperature of the printer's platen (substrate temperature), the cartridge temperature, the drop spacing and the nozzle height. By increasing the substrate temperature, the drying process is accelerated. The manipulation of the drying

process has a major influence on the layer morphology since it can affect the drying kinetics and determine the uniformity of the printed layer. The drying process depends on the boiling point of the solution. The higher is the boiling point the slower is the drying process. However, most printing inks incorporate mixture of solvents,[109] the surface tension and boiling point gradient generate flows during drying. The capillary and maragoni flows that are generated during the drying process should be balanced to provide the desired layer morphology.[110–112]

Drop spacing is the parameter that determine the film thickness. The greater the spacing between drops, the less amount of material is used during printing and therefore lower thicknesses are achieved. When the drop spacing is too big the drops may not be able to merge and give the desirable pattern (**Error! Reference source not found.**).

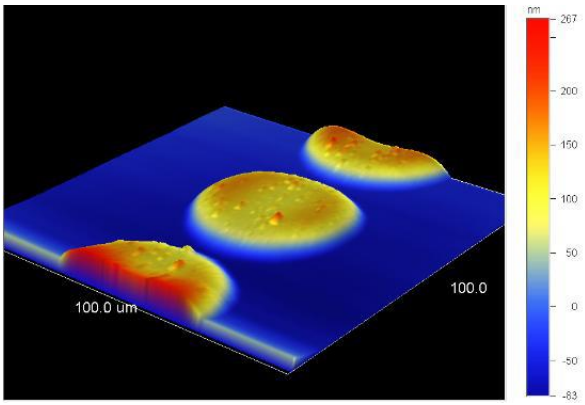

Figure 2.7: Mapping image of IJP pattern with large drop spacing, insufficient for droplets merging and film formation

An important parameter which is related with the resolution of the printed layers is the applied voltage which determines the volume, the speed and the uniformity of each drop and it synchronizes the fall of the drops. Also, voltage controls drop formation and drop size which are majorly defined by the nozzle size and fluid properties (viscosity, density, and surface tension). Figure 2.8 shows synchronize and uniform droplet ejection through the nozzles. It can be observed that the droplets have a tail due to the cohesive forces within the fluid. In order to achieve successful and high resolution printed layer the tail should be collected into the main drop. On the other hand, long tails can lead to the 'satellite effect' which is a drop contained in a ring of ink around it. In general, lower voltage leads to shorter tails which are more preferable.

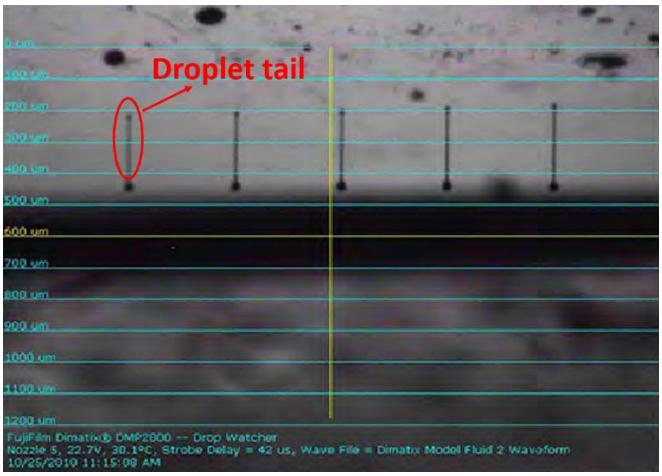

Figure 2.8: Droplets ejection from nozzles

Furthermore, important factors are the spreading, the wetting and the drying of the solution which is applied on the substrate. As it has already been mentioned, these are determined by the properties of the solution (viscosity and surface tension) and by the surface on which it will be applied (surface energy). The surface tension is the interaction between the consistency forces and the adhesive forces. The surface tension and surface energy are a function of the contact angle. The wetting of a surface is favored by the increase in the surface energy of the solid and the decrease in the surface tension of the liquid. A contact angle occurs when a drop falls on a solid substrate. For optimal spreading and wetting of the ink on the surface, the contact angle between the solution and the substrate must be limited to the minimum. The contact angle (θ) is defined by the Thomas Young equation, which describes the balance between the forces (F= γ.ds, where ds is the path element between the three phases) that are created when a liquid drop meets a solid surface.

$$\boldsymbol{\gamma_{lv}\cos(\theta) = \gamma_{sv} - \gamma_{sl}} \qquad \textbf{Equation 12}$$

Where θ is the contact angle, γ_{lv} is the interface tension between the liquid and the vapor (environment), γ_{sv} is the interface tension between the solid and the vapor (environment) and γ_{sl} is the interface tension between the solid and the liquid. The Young equation assumes that the surface of the solid is smooth, uniform and rigid. It must also be chemically and naturally inactive with the liquids which come in contact with.

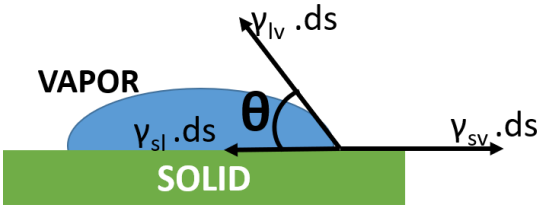

Figure 2.9: Contact angle

3. Printed copper nanoparticle metal grids for cost-effective ITO-free solution processed solar cells

The high cost and rigidity of the widely used ITO electrode in OPVs limit the commercialization prospects of flexible photovoltaics. A promising method of replacing ITO is by metal grid designs which ensure adequate light transmittance and appropriate conductivity for efficient current collection. Furthermore, inkjet printing with drop on demand technology has the ability to be introduced in a roll to roll production line providing opportunities for solution processed electrodes. Nowadays, noble metal nanoparticle inks such as silver are dominant in the field and several efficient ITO-free OPVs with inkjet-printed (IJP) silver grids have been reported in the literature. However, copper nanoparticle inks have drawn much attention since they have the potential to constitute an alternative cost-effective solution for ITO-free printed electronic applications.

This chapter demonstrates an effort to show the challenges and potential of IJP Copper (Cu) structures to replace the rigid and expensive ITO. Efficient cost-effective ITO-free OPVs processed in ambient conditions and comprising an IJP copper nanoparticle grid were presented for the first time. This reported work demonstrates important aspects of copper nanoparticles for printed electronics such as printing parameters, sintering and metal grid design optimisation. The proposed copper nanoparticle ink which has excellent jetting and printing properties resulting in high quality IJP Cu nanoparticle metal grids. ITO-free, Si-PCPDTBT: PC[70]BM OPVs processed in ambient low-cost fabrication conditions comprising embedded and non embedded inkjet-printed copper grid/Poly(3,4-ethylenedioxythiophene): poly(styrenesulfonate) (PEDOT:PSS) as the bottom electrode with power conversion efficiencies (PCE) of 2.6% and 3.4% respectively are presented. The results of the ITO-free OPVs using inkjet-printed Cu nanoparticle current collecting grids are discussed relevant to reference ITO-based OPVs with PCE of 4.9%. Part of the PCE losses for the developed non embedded Cu based ITO-free OPVs are due to the bottom electrode conductivity which decreases upon the necessary annealing step of PEDOT:PSS in air.

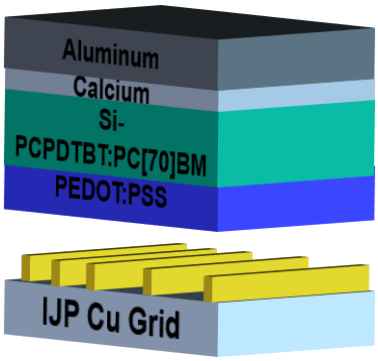

Figure 3.1: Device structure of ITO-free OPV

3.1. Introduction

The viability and sustainability of organic photovoltaics is based on three main pillars, namely an increased power conversion efficiency (PCE), a prolonged lifetime and low production costs. During the last years, a lot of effort has been undertaken by the research community around those three pillars toward OPVs commercialization. OPVs with high PCEs and prolonged lifetime have been achieved.[92,113,114] However, the combination of PCE, stability and low cost production is still challenging and essential for a feasible commercialization of this technology. One of the major privileges of OPVs is that they can be solution processed and fabricated with fast roll to roll techniques such as gravure, flexographic, slot die coating and inkjet printing.[115–117] Inkjet printing with drop on demand technology has the ability to be integrated in a roll to roll production line reducing the fabrication cost and providing technological opportunities and a unique design flexibility.[118] Inkjet printing has been used for the deposition of all the layers of an OPV stack and recently some works have demonstrated fully IJP OPV.[81,82,118–120] Remarkably, inkjet printing has been widely used in the fabrication of metal grid designs as a substitution of the rigid and expensive ITO transparent conductor.[34,121–123] Nowadays, silver nanoparticle based inks are dominant in the field and several efficient ITO-free OPVs with IJP silver grids have been reported.[46,72,80,88,124–126] A high efficient ITO-free OPVs with IJP Ag grid is also reported in our previous work.[46,127] On the other hand, copper nanoparticle based inks are gaining more and more attention, as copper nanoparticle ink is six times cheaper than silver nanoparticle ink and could potentially further reduce the fabrication cost of OPVs.[128] However extensive research in literature showed that ITO-free printed electronic devices using Cu electrodes have not been previously reported.

The main drawback of Cu-based inks is the instability of the printed Cu-structures related to undesired oxidation while being processed in ambient conditions. Due to the high Cu oxidation reactivity with increasing temperature in ambient conditions, the conventional thermal sintering used in noble metal nanoparticles (e.g. Ag) is not practicable. Instead, alternative fast sintering methods such as laser sintering or intense pulsed light sintering have been reported to be more convenient.[78,129–131] A selective sintering is performed while a specific wavelength beam is applied and absorbed by Cu nanoparticles. Laser

sintering provides concentrated power in a very short time frame, thus minimizing Cu oxidation and yielding the desired conductivities for optoelectronic applications.

However, Polino et al. reported another major drawback which may challenge the use of Cu inks for the fabrication of OPVs and other printed opto-electronic applications. They investigated three different commercially available Cu nanoparticle inks and reported serious difficulties due to the identified fast oxidation of the IJP Cu grids when combined with PEDOT:PSS.[128]

In this work efficient ITO-free OPVs comprising IJP Cu grid/PEDOT:PSS as the bottom electrode were presented for the first time. Importantly, both the printing and the sintering of the Cu grids were performed in ambient conditions. The proposed Cu nanoparticle ink produced using copper nanoparticles of approximately 100 nm in diameter, has been formed by a high temperature plasma synthesis method (CI-005, synthesized by Intrinsiq Materials). The dispersion was adjusted to a viscosity of approximately 12 cP and the surface tension of the ink was 29-30 $mN.m^{-1}$ providing excellent printability behaviour and stability during the printing and sintering pristine Cu grids process. Furthermore, it was shown that optimization of the laser sintering procedure provided high conductivity and good adhesion on glass substrates. The non-embedded Si-PCPDTBT: PC[70]BM based ITO-free devices showed a power conversion efficiency (PCE) of 3.4% whereas the ITO-based OPV showed a 4.9% PCE. It is shown that the conductivity of the developed bottom electrode decreases upon the necessary annealing step of PEDOT:PSS in air. Oxidation of copper at elevated temperatures is revealed as the main drawback of Cu grid-based OPVs and one of the reason of demonstrating lower device performance than ITO-based OPVs. Finally, initial trials on embedded IJP Cu based Si-PCPDTBT: PC[70]BM OPVs are also developed by following a reverse nanoimprinting transfer procedure and a PCE of 2.6% is achieved. Despite the lower performance and additional steps needed during the fabrication process the embedded ITO-free OPVs show the potential of processing sintered Cu on flexible surfaces, providing technological opportunities for flexible electronic applications.

3.2. Materials and Methods

Soda-lime glass substrates were sonicated in acetone and subsequently in isopropanol for 10 minutes followed by additional 10 minutes of UV-O_3 treatment before printing. The

CI-005 copper ink was produced using copper nanoparticles of approximately 100 nm in diameter, which had been formed by a high temperature plasma synthesis method. The nanoparticles were added to a blend of solvents containing a small quantity of additives and resin and dispersed using a bead mill. The dispersion was then filtered and adjusted to a viscosity of approximately 12 cP with additional solvent. The surface tension of the ink was 29-30 $mN.m^{-1}$. The copper nanoparticle-based ink (Intrinsiq materials CI-005) was inkjet-printed using a Fujifilm Dimatix DMP-2800 piezoelectric drop on demand printer with a 10 pL cartridge on top of the glass substrates. The printing process was performed in ambient conditions. The substrate and cartridge temperatures were set at 35 °C. The print head was set at 700 µm above the substrate and Cu lines were printed with 25 µm drop spacing resulting in lines of ~450nm average height and ~80-85 µm width as measured with a Veeco Dektak 150 profilometer.

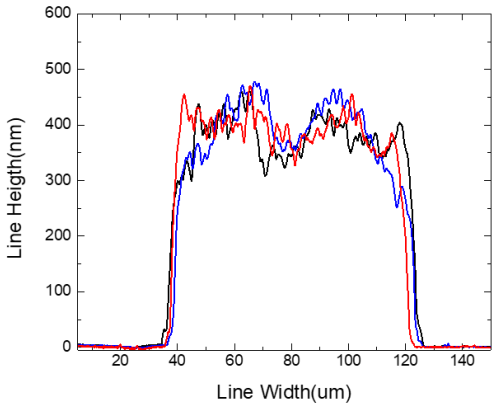

Figure 3.2: Profilometry of IJP Cu lines printed with 25 µm drop spacing

The IJP Cu grids were dried on a hotplate at 60 °C for 1 hour. An infra-red diode laser (LAPS 60, Intrinsiq Materials) with an output current of 55 A, 808 nm beam, 25 mm/s speed and a distance of 14 mm between a focusing lense and the sample surface was used to sinter the IJP Cu grids. Highly conductive (~200 $S.cm^{-1}$) PEDOT:PSS with neutral pH (Clevios P Jet NV2) was doctor bladed on top of the ITO or on the embedded IJP Cu layer resulting in ~90 nm layer thickness. For non-embedded IJP Cu grids ~200 nm PEDOT:PSS was doctor bladed to overcoat the Cu lines. Annealing of PEDOT:PSS layers was performed at 140°C on a hotplate for 20 minutes in ambient conditions. For the embedding of IJP Cu grid,the procedure described elsewhere was followed and is

shown in detail in Figure 3.3.[18, 34] Ormocomp© and ormoprime© were purchased from micro resist technology.

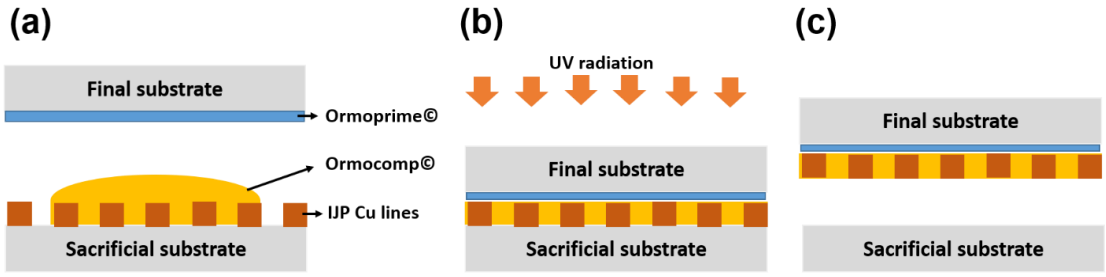

Figure 3.3: Embedding procedure of IJP Cu lines (a) Ormoprime© adhesion promoter is applied on the final substrate. Transparent UV-curable Ormocomp© resin is drop-casted on the sacrificial substrate with the IJP Cu grid. (b) The two substrates are brought to close proximity and pressured. Then, UV radiation is applied. (c) The two substrates are separated mechanically by applying force between the two substrates leading to the embedded IJP Cu grid substrates.

Pre-patterned ITO substrates (sheet resistance 4 Ω/□) were purchased from Psiotec Ltd. The photoactive layer, a blend of poly[(4,40-bis(2-ethylhexyl) dithieno[3,2-b:20,30-d]silole)-2,6-diyl-alt-(4,7-bis(2-thienyl)-2,1,3-benzothiadiazole)-5,50-diyl] (Si-PCPDTBT):[6,6]-phenyl-C71-butyric acid methyl ester (PC[70]BM) (1:1.5 by weight) at a concentration of 15 mg/ml in chlorobenzene, was doctor bladed on top of PEDOT:PSS resulting in a layer thickness of ~100 nm. To complete the normal-structured stack, 10 nm of calcium and 100 nm of aluminum both of which were thermally evaporated on top of the photoactive layer and patterned through a shadow mask, resulting in four solar cells, each with an active area of 9 mm^2. Topographic analyses were performed using a Quanta 200 SEM (FEI, Hillsboro, Oregon, USA). A four-point probe (Jandel RM3000) conductivity meter was employed for sheet resistance measurements. The current density-voltage (J/V) characteristics were measured with a Keithley source measurement unit (SMU 2420) and a calibrated Newport solar simulator equipped with a Xe lamp (AM1.5G spectrum at 100 $mW.cm^{-2}$ as measured by an Oriel 91150V calibration cell equipped with a KG5 filter). A 9 mm^2 mask was used to define the exact area of the device. Photocurrent mapping measurements were performed under 405 nm laser excitation using a Botest PCT photocurrent system.

3.3. Results and Discussion

3.3.1. Laser sintering optimization

It is known that the sintering of copper nanoparticles with conventional heating methods leads to fast oxidation.[132] In this work the sintering of the inkjet-printed Cu structures was therefore performed with laser sintering by using an infra-red (808 nm) diode laser beam in continuous mode in order to overcome the aforementioned limitation.[78,130] It is worth mentioning that a drying step of IJP Cu structures is needed before laser sintering in order to avoid spontaneous solvent evaporation which lead to unfavoured morphological distorters and spikes during sintering. In this work, Cu films were dried at 60°C for one hour on a hotplate. This step provide mild drying of solvents contained in Cu ink and control the flows that are generated during drying [79], defining somehow the uniformity of the printed layer and eliminating spikes that might occur during laser sintering.

In order to find the optimum laser sintering conditions, a scan with constant speed and different distances between a laser focusing lense and the substrate (focal length) was performed. This distance defines the diameter of the laser spot on the sample surface and consequently the energy input per area. The optimum distance was found to be between 12-16 mm (Figure 3.4).

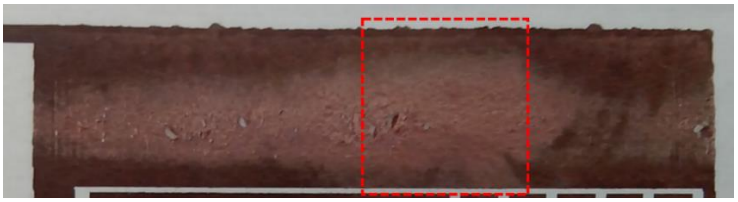

Figure 3.4: Sintered Cu structure with different focuses. Red dashed boarded area indicates the sintered area with 12-16 mm distance between focusing lense and sample surface

Figure 3.5 illustrates the conductivity of Cu films sintered with different laser scanning speeds and distances of 16 mm (black squares), 14 mm (red circles) and 12 mm (blue triangles). The highest conductivities were achieved with 16 and 14 mm at 15 and 20 $mm.s^{-1}$ scanning speeds. However, at these speeds the Cu structure was partially or sometimes completely detached from the substrate due to the high power applied and the subsequent excessive thermal stress. Therefore, optimum sintering conditions were found to be at 25 $mm.s^{-1}$ scanning speed and a distance of 14 mm, still providing a high

conductivity of ~36000 S.cm^{-1} (sheet resistance of ~500 mΩ/□ for ~550 nm film thickness) and also the desired adhesion on the glass substrates. Figure 3.5b and c show SEM images of a Cu layer before and after laser sintering, respectively. The effect of laser sintering can be seen in the necking and merging of Cu nanoparticles.

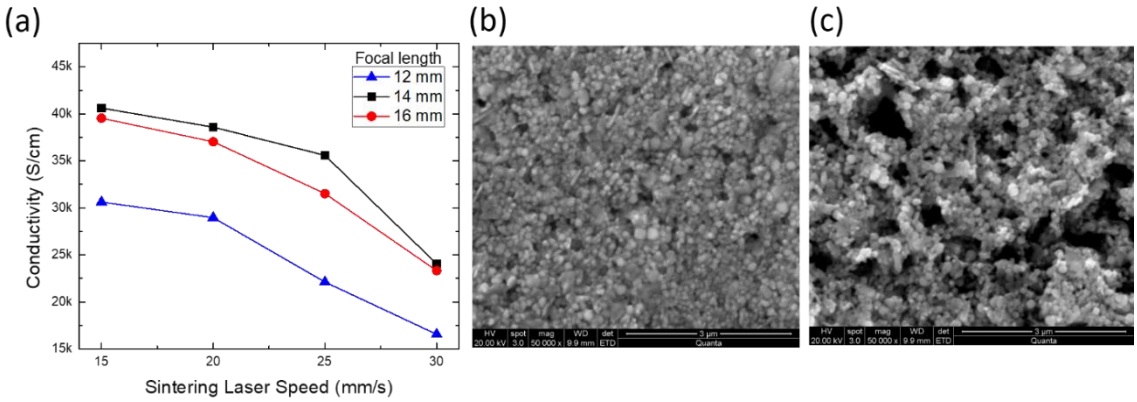

Figure 3.5: (a) Conductivity of printed Cu layers after sintering with different laser speeds at 12 mm (blue triangles), 14 mm (black squares) and 16 mm (red circles) focal lengths. (b) SEM image of un-sintered Cu and (c) SEM image of sintered Cu

3.3.2. Cu line dimensions, PEDOT:PSS thickness and conductivity

The main challenges of IJP metal grid structures when used for OPVs, are the line height and potential spikes occurring during solvent evaporation contained in the nanoparticle ink. These can lead to direct contact of metal with the active layer or even with the top electrode resulting in high leakage current or in short circuits. In order to overcome this limitation thick PEDOT:PSS layers were used to overcoat the metal grid lines.[125,133] However, thick PEDOT:PSS layers reduce the transparency of the electrode and thus studies to reduce the line height by controlling printing parameters, embedding metal grid in transparent resin and either with UV-O_3 treatment have been reported.[124,134–138] In this study, only the implementation of UV-O_3 treated surfaces resulted in optimum wettability of the ink on the substrates, enabling the printing of high quality lines, as shown in Figure 3.6.

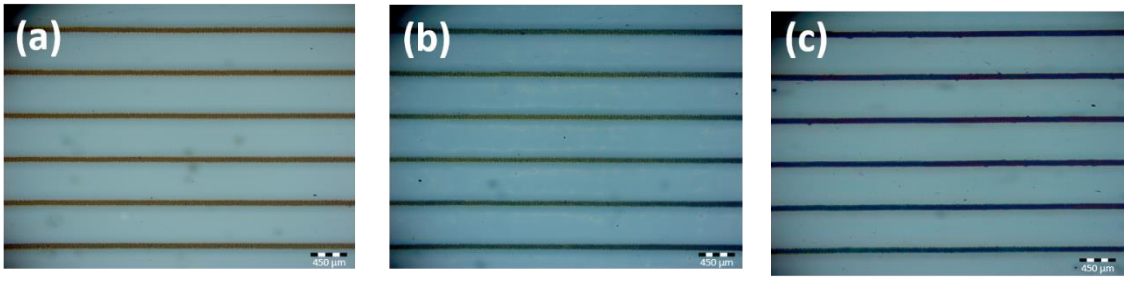

Figure 3.6: Microscope images of IJP Cu lines (a) without PEDOT: PSS, (b) with ~100 nm PEDOT: PSS incompletely covered and (c) with ~200 nm PEDOT: PSS completely covered

In addition, by altering the printing parameters and especially the drop spacing the lowest possible Cu line achieved was 450 nm as shown in Figure 3.2. On the other hand, the thinnest possible PEDOT:PSS layer should be applied in order to reduce transmittance losses, while still covering the Cu lines. Figure 3.6b and 3.6c show microscope images of IJP Cu lines with ~100 nm and ~200 nm PEDOT:PSS layers, incompletely and fully covered, respectively. The latter is in accordance with the findings of Galagan et al. who reported that ~200 nm of PEDOT:PSS were enough to cover 600 nm Ag grid lines.[125]

It is well known that an optimized ITO-free electrode consisting of a metal grid and PEDOT:PSS should combine minimum transmittance losses and a desired conductivity. In previous reported works the optimum metal covered area was found to be around 10-13%.[124,125] In addition, high and low conductivity PEDOT:PSS combined with Ag grids have been previously implemented to efficiently replace ITO. The use of high or low conductivity PEDOT:PSS depends on the metal conductivity, the metal covered area, the grid design and the device area.

In our previous work it was shown that highly conductive Ag grid with 13% Ag covered area and low conductivity formulation Clevios PH PEDOT:PSS (0.01 $S.cm^{-1}$) efficiently replaced ITO.[133] In this work, the device performance of OPVs with Cu-grid and two different PEDOT:PSS formulations with low (0.01 $S.cm^{-1}$) and high conductivity (200 $S.cm^{-1}$) respectively is initially investigated.

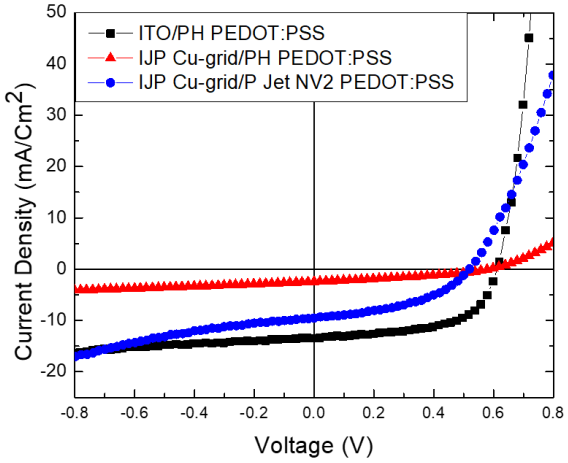

Figure 3.7: Illuminated J/V characteristics of OPVs with bottom electrode: ITO/ PH PEDOT:PSS (black squares), Embedded 8-line Cu grid/ PH PEDOT:PSS (red triangles), Embedded 8-line Cu grid/ P Jet NV2 PEDOT:PSS (blue circles).

Table 3.1: **Photovoltaic parameters of OPVs with IJP Cu grid with different PEDOT:PSS formulations**

OPVs with bottom electrode:	**Voc (V)**	**Jsc ($mA.cm^{-2}$)**	**FF (%)**	**PCE (%)**
ITO/ PH PEDOT:PSS (control device)	0.62	13.5	58	4.8
IJP Cu grid/ PH PEDOT:PSS	0.58	2.4	34	0.5
IJP Cu grid/ P Jet NV2 PEDOT:PSS	0.52	9.6	44	2.2

OPVs with IJP Cu grid combined with low conductivity PEDOT:PSS exhibited poor device performance (Figure 3.7 and Table 3.1). It is found that low conductive PEDOT:PSS cannot assist in an efficient charge collection. Therefore, Clevios P Jet NV2 PEDOT:PSS with ~200 $S.cm^{-1}$ conductivity combined with IJP Cu grid constitutes the bottom electrode of ITO-free OPVs in this work.

3.3.3. Non-embedded ITO-free OPVs with IJP Cu line grids

To investigate the effect of the surface covering area on the device performance, devices with different number of Cu grids lines were fabricated. Their representative illuminated and dark J/V characteristics are shown in Figure 3.8.

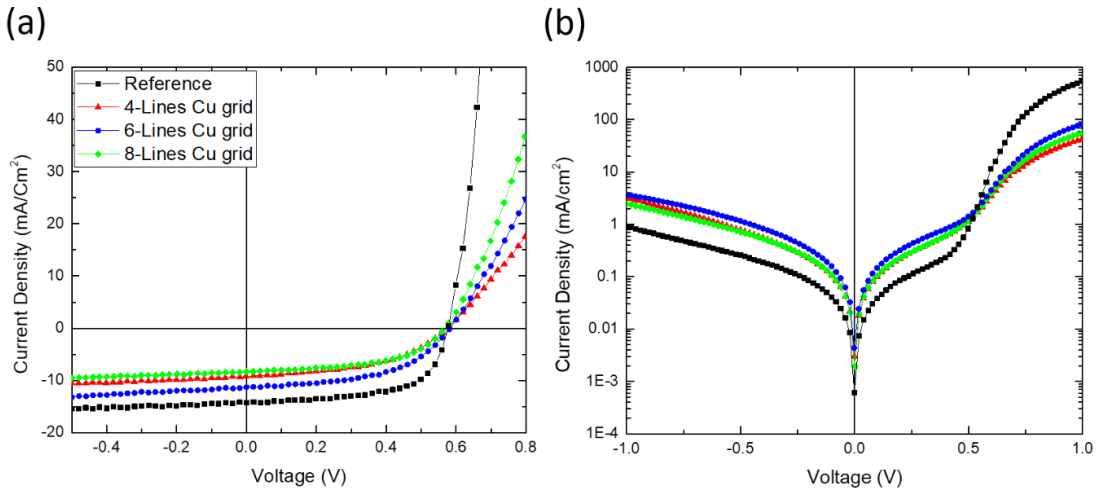

Figure 3.8: (a) Illuminated and (b) dark J/V characteristics of OPVs with bottom contact: ITO (black squares), 4-line Cu grid (red triangles), 6-line Cu grid (blue circles), 8-line Cu grid (green diamonds).

ITO-free OPVs based on IJP Cu grids with a pitch of 0.6 mm (4 lines), 0.43 mm (6 lines) and 0.33 mm (8 lines) were fabricated and compared. Table 3.2 summarizes the photovoltaic parameters of the OPVs under study. The control ITO-based device demonstrated the highest power conversion efficiency (PCE) of 4.9% whereas the highest PCE of Cu grid-based OPVs is 3.4% (6 lines). Comparing the ITO-free devices an improvement of the fill factor (FF) in Cu-grids comprising more lines is observed. In addition, short circuit current (J_{sc}) is increased by increasing the number of lines until a turning point where the shadowing losses are more dominant. The optimum balance between carrier collection and shadowing losses was obtained with a 6-line grid, providing 11.4mA.cm^{-2} J_{sc} and 51% FF whereas the reference exhibits 14.1 mA.cm^{-2} and 58% FF. Around 15% of the total 20% loss in J_{sc} can be well attributed to the shadowing losses of Cu grid design (Figure 3.9) and the lower transmission of the thicker PEDOT:PSS layer.

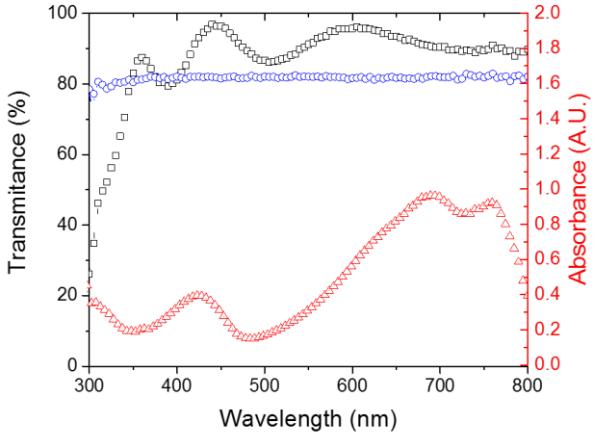

Figure 3.9: Transmittance of ITO (black squares) and 6-Lines Cu grid (Blue circles). Absorbance of Si-PCPDTBT-layer (red triangles).

Table 3.2: Photovoltaic parameters of OPVs with IJP Cu grid with different number of lines. The photovoltaic parameters were averaged over four devices.

ITO-free Cu based OPVs	Surface coverage (%)	Voc (V)	Jsc ($mA.cm^{-2}$)	FF (%)	PCE (%)	R_s ($\Omega.cm^2$)	R_p ($\Omega.cm^2$)
ITO	-	0.60±0.02	14.1±0.7	58±2	4.9±0.1	1.48	2328
4-line grid	11.33	0.57±0.01	9.7±0.3	43±4	2.4±0.2	8.37	863
6-line grid	17.00	0.58±0.01	11.4±0.8	51±2	3.4±0.3	4.50	583
8-line grid	22.67	0.56±0.01	8.8±0.4	48±4	2.3±0.2	6.38	858

However, to gain more insights about the losses in device performance in ITO-free OPVs, the dark JV characteristics were plotted (Figure 3.8b). The series resistance (R_s) of Cu grid-based OPVs is significantly higher than that of ITO-based OPVs. The Cu grid-based OPVs measured under dark conditions (Figure 3.8b) have low current density at forward bias and thus significantly higher series resistance (R_s) values compared with ITO-based

OPVs. The R_s indicates the current resistance in the vertical direction between the layers and interfaces comprising the OPV. In this case the changes in R_s can therefore be assigned mainly to the conductivity of the electrode.[139,140]

In addition, all the Cu grid-based OPVs have higher leakage current (lower parallel resistance, Rp) than ITO-based OPVs. The latter can be attributed to the morphology of Cu grid-based OPVs and peaks of Cu-lines that were not fully over coated by PEDOT:PSS, in contrast to the flat morphology of ITO electrode. The increased Rs and reduced Rp values of Cu grid-based OPVs are reflected in the lower fill factor values compared with the ITO-based OPVs. The FF of the control device is 58% whereas optimum Cu grid-based OPVs exhibit 51% FF.

It has been concluded that one of the main reasons of the lower device performance compared with the ITO-based OPVs is the conductivity of the electrode. In line to this, the JV parameters reveal conductivity limitations of the Cu grid arising possibly from the OPV fabrication process. Therefore, further studies were performed aiming the identification of the reduced performance of IJP Cu/PEDOT:PSS bottom electrode.

3.3.4. Compatibility study of Cu grid with PEDOT:PSS

A possible reason of the reduced conductivity of Cu-grids could be the failure of Cu-lines during OPVs processing. In order to analyze the functionality of the developed Cu grids photocurrent mapping measurements were carried out (Figure 3.10).

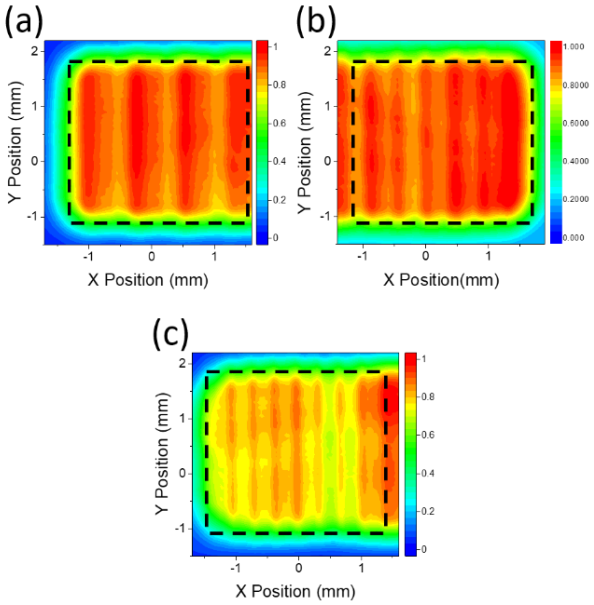

Figure 3.10: Normalized photocurrent mapping images of OPVs with IJP Cu grid lines (a) 4 lines, (b) 6 lines and (c) 8 lines.

This powerful imaging technique allowed us to easily identify defects in photocurrent distribution along the Cu grid structures. Normalized photocurrent mapping images reveal an efficient and homogeneous current distribution through the Cu grid lines for the 4-line and 6-line configuration, proving the reliability of the printed lines. In contrast to this high photocurrent intensity, the 8-line Cu-grid showed a lower intensity and less current collection, which is in accordance with the J_{sc} values shown in Table 3.2.

Despite the initial high conductivity of Cu, ITO-free OPV parameters demonstrated lower current density and higher series resistance compared with the reference device, revealing conductivity limitations of Cu grid that might have been occurred during the fabrication of OPVs.

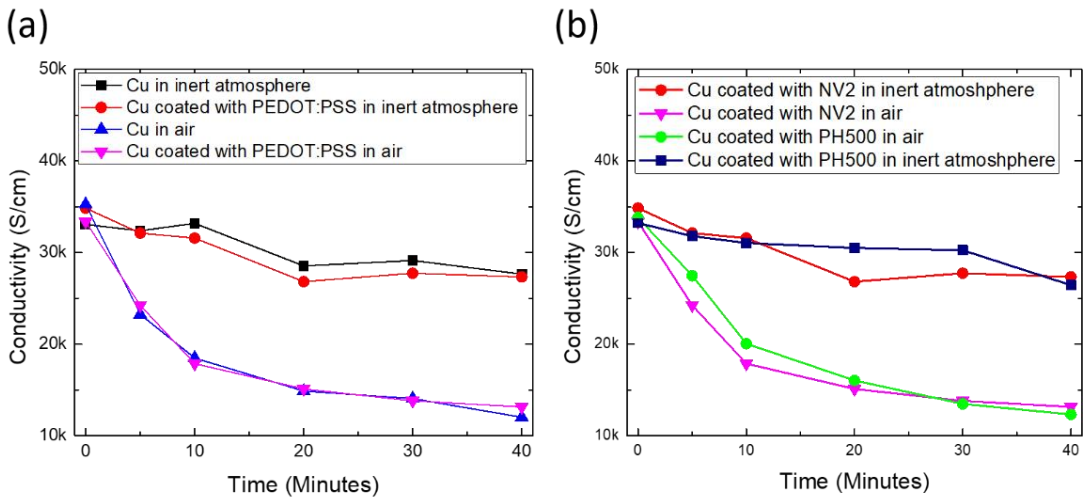

Figure 3.11: (a) Conductivity over time of IJP Cu layers aged at 140 °C (i) in inert atmosphere (black square), (ii) coated with PEDOT:PSS NV2 in inert atmosphere (red circle), (iii) in air (blue triangle) and (iv) coated with PEDOT:PSS NV2 in air (magenta downward triangle) (b) Conductivity over time of IJP Cu layers aged at 140 °C (i) coated with PEDOT:PSS PH500 in inert atmosphere (blue squares), (ii) coated with PEDOT:PSS PH500 in air (green circles)

As mentioned previously, Polino et al. pointed out the incompatibility of PEDOT:PSS with Cu grid. In order to investigate the compatibility of Cu grid with PEDOT:PSS, the sheet resistance of Cu films with and without PEDOT:PSSs was measured over time at 140 °C in air and in inert atmosphere. The temperature of 140 °C was chosen since it is widely used as the optimum annealing temperature for the PEDOT:PSS in OPVs

fabrication. Figure 3.11a illustrates the resulting conductivity values of Cu layers subjected to thermal stress at 140 °C with and without PEDOT:PSS (clevios P Jet NV2 formulation) for 40 minutes. Interestingly, the results indicate that PEDOT:PSS has no considerable influence on Cu conductivity but heating of Cu in air does cause a reduction in conductivity. The initial conductivity value (35000 $S.cm^{-1}$) of pure Cu nanoparticle films is reduced to less than the half (15000 $S.cm^{-1}$) after 20 minutes at 140°C in air. On the other hand, the conductivity of such films aged for 20 minutes in inert atmosphere only suffers a minor reduction.

Mayousse et al., have observed improved conductivity values of copper nanowires when coated them with PEDOT:PSS (pH ~2.5). The enhanced conductivity was ascribed to the acidic nature of PEDOT:PSS (pH ~2.5).[141] The remaining insulating copper oxide was removed and allows regeneration of the electrode when acidic PEDOT:PSS was coated on top of copper nanowires. In order to investigated the above statement, PEDOT:PSS PH500 with pH ~2.5 was introduced to this study. Cu layers were fully coated with the specific formulation PEDOT:PSS. Figure 3.11b illustrates the calculated conductivity values over time of Cu with and without the two PEDOT:PSS under comparison subjected at 140 °C. Again, we haven't observed any change in conductivity before and after coating Cu with PEDOT:PSS PH500 but we have observed similar degradation trend of Cu conductivity on films coated with the PEDOT:PSS NV2 formulation when heat is applied. These results indicate that in this case the acidic nature of PEDOT:PSS could not assist in conductivity enhancement and therefore acidity of PEDOT:PSS has not any influence in Cu conductivity, in contrast to heat.

Further investigation of the influence of different temperatures, ranging from 60°C-160°C, on the Cu conductivity is presented in Figure 3.12 which would be useful for other material systems or optoelectronic applications. Reduction of Cu conductivity was observed for all temperatures used in this study over time. It can be observed that as the temperature increases the conductivity exhibits a decrease. A fast oxidation and a dramatic reduction of Cu conductivity was observed at 160°C. In addition, the influence of different PEDOT:PSS annealing temperatures on the device performance of Cu-grid based OPVs was investigated as shown in Figure 3.12 and Table 3.3. The annealing temperature of PEDOT:PSS has a major influence on the device performance of OPVs. Cu-grid based OPVs with PEDOT:PSS annealed at 80 °C and 100°C have lower PCE

than those annealed at 120°C and 140°C. Cu-grid based OPVs with PEDOT:PSS annealed at 120°C have slightly better performance than Cu-grid based OPVs with PEDOT:PSS annealed at 140°C. Overall annealing temperature of PEDOT:PSS at 120 °C or 140 °C are found to fulfilled the processing annealing conditions of PEDOT:PSS but are still high enough to reduce Cu conductivity.

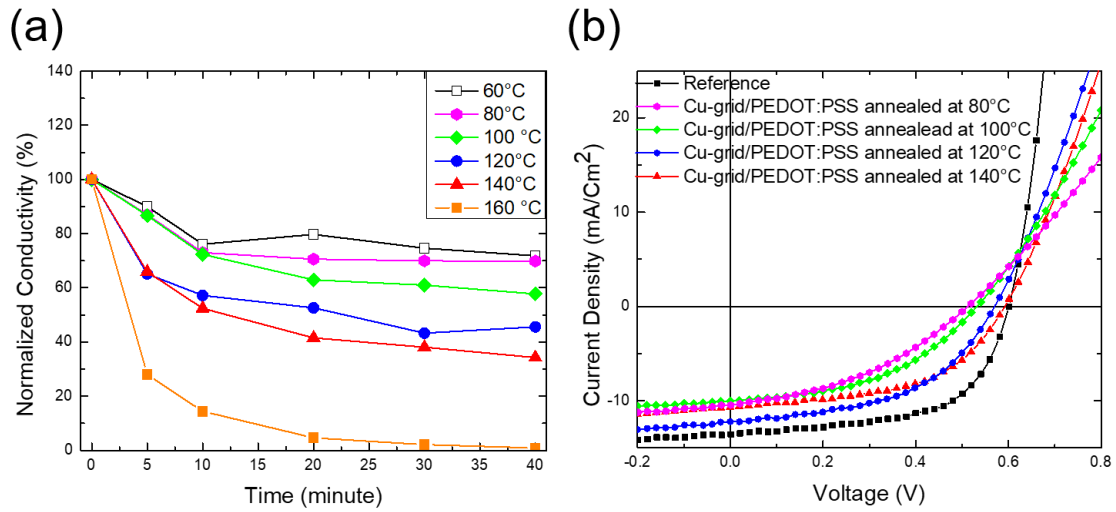

Figure 3.12: (a) Influence of different temperatures on the Cu conductivity. (b) Influence of lower PEDOT:PSS annealing temperatures on Cu grid-based OPVs performance

Table 3.3: **Photovoltaic parameters of OPVs with IJP Cu grid with different annealing temperatures of PEDOT:PSS. The photovoltaic parameters were averaged over four devices.**

OPVs	Voc (V)	Jsc ($mA.cm^{-2}$)	FF (%)	PCE (%)
Reference	0.61±0.01	13.8±0.7	58±3	4.9±0.1
Cu grid-PEDOT:PSS annealed at 140°C	0.59±0.01	10.7±0.2	51±1	3.2±0.1
Cu grid-PEDOT:PSS annealed at 120°C	0.56±0.01	12.1±0.7	50±1	3.4±0.2
Cu grid-PEDOT:PSS annealed at 100°C	0.53±0.02	10.5±0.6	44±3	2.4±0.1

Cu grid-PEDOT:PSS annealed at 80°C	0.51±0.02	10.7±0.6	41±2	2.2±0.3

These results show the corrosion tendency of sintered Cu nanoparticle films at elevated temperatures in air and emphasize the significance of OPV processing limitation of Cu at elevated temperatures in air.[142] Based on the above, the increased R_s and therefore the lower device performance of Cu-based OPVs is attributed to the reduced conductivity of Cu arising from oxidation during the annealing of PEDOT:PSS.

It is believed that this is the main reason of the mismatch between the optimum found Cu covered area (17%) of this work and other works which have reported optimum metal covered area around 10-13%. In this case, more Cu lines are needed in order to improve the conductivity of the electrode, however this has a negative impact on its transparency (higher shadowing), thus limiting the J_{sc}. The same applies for the proposed PEDOT:PSS formulation as its high conductivity is needed to improve the overall conductivity of the electrode and assist in current collection. The above results indicate that transferring the annealing process of PEDOT:PSS to inert atmosphere might recover part of the PCE losses of the ITO-free OPVs. However, all the printed Cu-based ITO-free OPVs presented in this work are processed in ambient conditions, which is suitable parameter for low-cost solution processed OPV.

3.3.5. Embedding of IJP Cu grids through reverse nanoimprinting transferring procedure

As mentioned earlier, a crucial point of ITO-free OPVs with inkjet printed metal grids is the line height and topography, as they need to be coated with a thick PEDOT:PSS layer. In order to overcome the aforementioned limitation and reduce the transmittance losses, ITO-free OPVs with embedded metal grid designs were developed.[124]

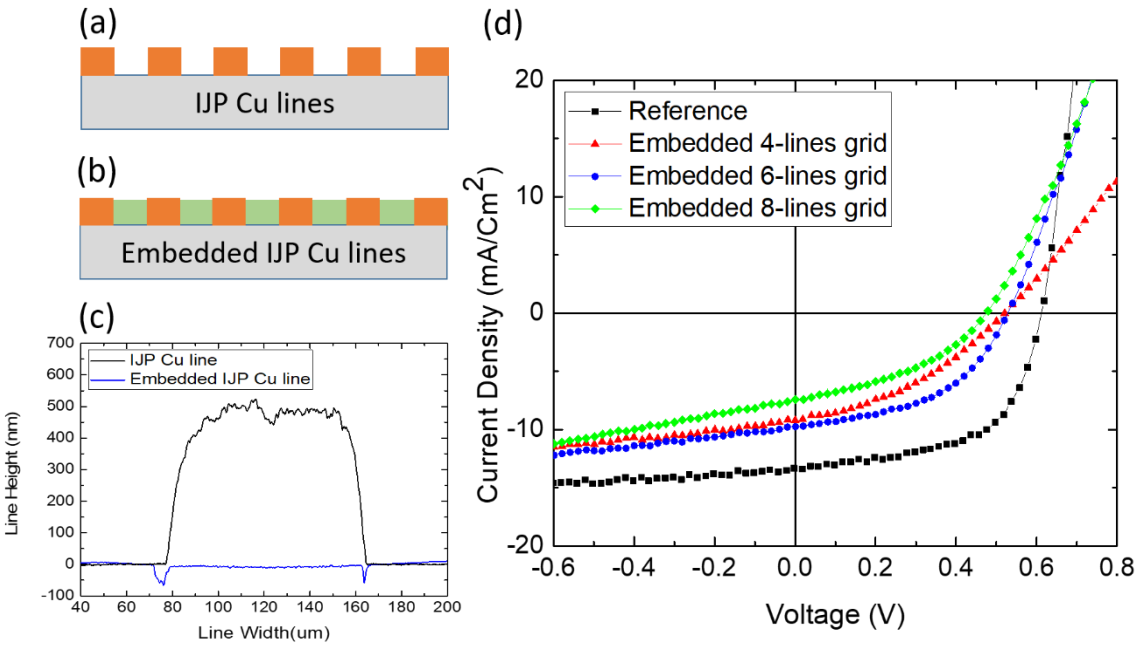

Figure 3.13: Schematic view of Cu lines (a) before embedding and (b) after embedding. (c) Profilometry of IJP Cu lines before (black line) and after embedding (blue line). (d) Illuminated J/V characteristics of OPVs with bottom contact: ITO (black squares), Embedded 4-line Cu grid (red triangles), Embedded 6-line Cu grid (blue circles), Embedded 8-line Cu grid (green diamonds).

At first, the embedding of IJP Cu lines within a transparent resin (see transparency of resin in Figure 3.14) allow the use of thinner PEDOT:PSS, thus reducing losses in transparency. Secondly, the employed flipping over procedure provides superior, flat smooth surfaces and lines without spikes as depicted in Figure 3.13c. Smooth surfaces and lines without spikes could reduce leakage current and thus improve R_p and FF values. In addition, since line height influences the grid conductivity, embedding allows the use of thicker lines without affecting the layers that will be deposited. Finally, the specific embedding procedure followed in this study could provide technological opportunities as the final embedded Cu-grid can be applied on flexible surfaces.

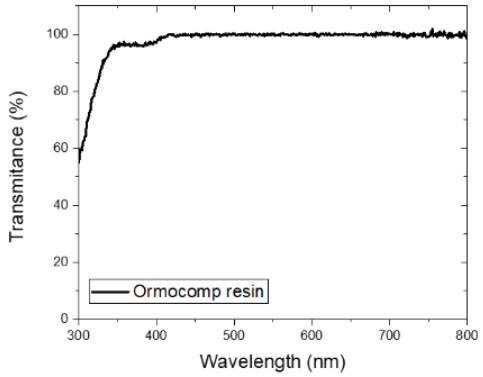

Figure 3.14: Transmittance of Ormocomp resin

The concentrated high intensity of laser sintering of Cu on flexible substrates could lead to excessive heating and shrinkage of the substrate due to the heat transfer from Cu to the substrate. Thus, lower energy intensities or pulsed sintering have to be used resulting in lower Cu conductivities. The embedding procedure could combine the high conductivity of IJP Cu structures sintered on glass with the application of the embedded Cu-grid onto a flexible substrate by using the flipping over procedure. [143] The sheet resistance value of sintered Cu remains unchanged after the transferring procedure as measured with four point probe.

Table 3.4: **Photovoltaic parameters of OPVs with embedded IJP Cu grid with different number of lines. The photovoltaic parameters were averaged over four devices.**

ITO-free Cu based OPVs	**Voc (V)**	**Jsc ($mA.cm^{-2}$)**	**FF (%)**	**PCE (%)**
ITO	0.60±0.02	14.1±0.7	58±2	4.9±0.1
Embedded 4-line grid	0.54±0.02	9.8±0.4	42±3	2.2±0.3
Embedded 6-line grid	0.54±0.01	10.6±1.1	45±4	2.6±0.2
Embedded 8-line grid	0.54±0.02	9.4±1.0	44±1	2.2±0.1

ITO-free OPVs with embedded IJP Cu grid-lines were fabricated and JV characteristics of illuminated devices and JV parameters are illustrated in Figure 3.13 and Table 3.4 respectively. The same photovoltaic trend with non-embedded IJP Cu grid based OPVs was observed for embedded IJP Cu grid based OPVs: again, the optimum configuration was the 6-line Cu grid. Embedded IJP Cu-grid could theoretically provide better performance than not-embedded IJP Cu-grid based OPVs. However, these experimental results show lower device performance. Embedded 6-line Cu grid based OPV exhibited a 2.6% PCE whereas the not-embedded 6-line Cu grid has 3.4% PCE. Comparing 6-line grid, embedded Cu based OPVs have lower values in all photovoltaics parameters compared with the non-embedded based OPVs (see Table 3.2 and Table 3.4).

The main drawback of the embedding procedure was found to be the complication and the lack of reproducibility of the flipping over procedure with such small substrates (15x15 mm) and delicate IJP Cu lines. In accordance to the above observations, IJP Cu lines were found to be too sensitive and prone to defects during the transferring procedure. It is believed that further optimization of the embedding procedure or alternative embedding methods could further improve device performance and be beneficial for processing of sintered Cu on flexible substrates. Despite the additional fabrication steps, embedding the Cu lines following the reverse nanoimprinting transfer process could meet the technical requirements to enable the fabrication of large area metal grid electrodes for flexible electronic applications.

3.4. Conclusions

In conclusion, the first functional electronic device based on ITO-free inkjet-printed Cu grid is reported. The development, sintering and optimization process of a suitable inkjet printing Cu nanoparticle ink is presented in this study. The results show that the proposed Cu-nanoparticles formed by plasma synthesis produce high quality printed Cu lines with desired values of conductivity and good adhesion properties resulting in efficient cost effective current collecting metal grids. The Si-PCPDTBT:PC[70]BM, ITO-free OPVs based on IJP Cu grid yielded 3.4% PCE whereas the ITO-based OPV was 4.9%. Despite the good compatibility of the developed Cu grid in combination with the proposed PEDOT:PSS, Cu oxidation and a reduced conductivity arises from the necessary annealing step of PEDOT:PSS in ambient conditions. This experimental work suggested that part of the ITO-free OPV losses due to reduced conductivity can be recovered by

incorporating the highly conductive PEDOT:PSS NV2. Finally, an effort to reduce R_p and transmittance losses was performed by embedding IJP Cu lines in a transparent resin through reverse nanoimprinting transfer method resulting in functional ITO-free embedded Cu-based OPVs. Despite the lower performance than the expected, the embedding procedure followed showing the potential of processing laser sintered Cu structures on flexible substrates relevant to flexible electronic applications.

4. Influence of the Hole Transporting Layer on the Thermal Stability of Inverted Organic Photovoltaics Using Accelerated Heat Lifetime Protocols

In this chapter the heat stability of a solution processed HTL (PEDOT:PSS) is compared with an evaporated HTL (MoO_3) in inverted OPVs. Inverted OPVs could be proved beneficial concerning product development targets of this technology mainly because their superiority in terms of long term stability compared to normal structured OPVs. Therefore, inverted structured OPVs are more preferable than normal structured. Furthermore, inverted structured OPVs usually use Ag as the top electrode which can be solution processed as it will be shown in Chapter 5. The most widely used HTL in inverted OPVs is the solution processed PEDOT:PSS. However, PEDOT:PSS is vulnerable to moisture due to its hygroscopic nature, a significant parameter that having a negative effect in stability of OPVs. On the other hand, high power conversion efficiency (PCE) inverted OPVs usually use thermally evaporated MoO_3 as a HTL. Despite the high PCE values reported, stability investigations are still limited and the exact degradation mechanisms of inverted OPVs using thermally evaporated MoO_3 HTL remain unclear under different environmental stress factors. In this chapter, the accelerated lifetime performance under the ISOS D-2 protocol (dark-low RH-65^o) of non-encapsulated inverted OPVs based on the thiophene-based active layer materials poly(3-hexylthiophene) (P3HT), Poly[[4,8-bis[(2-ethylhexyl)oxy]benzo[1,2-b:4,5-b']dithiophene-2,6-diyl][3-fluoro-2-[(2-ethylhexyl)carbonyl]thieno[3,4-b]thiophenediyl]] (PTB7) and thieno[3,2-b]thiophene-diketopyrrolopyrrole (DPPTTT) blended with [6,6]-phenyl C71-butyric acid methyl ester (PC[70]BM), respectively was investigated. The investigation of degradation mechanisms presented focus on optimized P3HT:PC[70]BM-based inverted OPVs. Specifically, a systematic study on the thermal stability of inverted OPVs comparing the solution processed PEDOT:PSS and the evaporated MoO_3 HTL is presented. PEDOT:PSS proved significantly more stable than MoO_3 under heat conditions. Using a series of measurements and reverse engineering methods it is reported that the P3HT:PC[70]BM/MoO_3 interface is the main origin of failure of P3HT:PC[70]BM-based inverted OPVs under heat conditions; a trend which is also observed for the two other thiophene-based polymers used in this study. The results

of this study also suggested that the interface between MoO_3 and Ag limits significantly the heat stability of inverted OPVs.

4.1. Introduction

Organic Photovoltaics have attracted great scientific interest during the last decade due to their ease of manufacture with printable techniques and their potential to become flexible, lightweight and low cost energy sources.[116,144] High power conversion efficiencies and prolonged lifetimes are essential for OPV commercialization. The barrier of 10% efficiency has already been overcome and OPVs exiting 10% power conversion efficiency (PCE) have been demonstrated.[145] On the other hand, long stabilities of OPVs is the next barrier that needs to be overcome. Understanding the degradation mechanisms that influence the stability of different device configurations using various environmental stress factors is still a challenging task.

In the inverted structure, the use of an air stable metal such as silver results in enhanced lifetime compared to normal structured OPVs, which are limited in stability mainly due to oxidation of the metals such as calcium or aluminum.[24,146,147] Poly(3,4-ethylenedioxythiophene) polystyrene sulfonate (PEDOT:PSS) is the most common material used as hole transporting layer in both architectures. It is known that due to its hydroscopic nature, ingress of moisture and oxygen from the edges into the device can cause degradation.[148,149] Also, it is suggested that PEDOT:PSS acidic nature leads in etching of ITO in normal structured OPVs.[97] On the other hand, in inverted OPVs PEDOT:PSS acts as a getter of moisture and oxygen and protects the active layer to react with air, suspending their degradation mechanism compared with normal structured OPVs.

Furthermore, heat is one of the environmental factors found to significantly affect the long term stability of OPVs. Heat stability studies at operating temperature performed by Sachs-Quintana *et al.* on normal structure OPVs show that a thin polymer layer forms at the back (metal) contact, which creates an electron barrier between the active layer and the cathode.[150] This is related to the interface between the back contact and the bulk heterojunction and is shown to be the first step in thermal degradation in organic solar cells with normal architecture and especially while using low glass transition temperature conjugated polymers. However, in inverted OPVs this barrier formation is favorable as it

helps hole selectivity. This feature has been claimed as an additional advantage of inverted OPVs.[150] Thus, the inverted structure is preferable concerning product development targets as it can allow more design flexibility and prolonged lifetime.

However, despite the prolonged lifetime of inverted structured OPVs compare with normal structured OPVs, the top electrode (the anode) of inverted OPVs has been identified as one of the most vulnerable parts of the device under various environmental stress factors. A lot of studies were performed and reveal the crucial influence of the interface between the active layer and HTL in the lifetime performance of inverted OPVs.[25,151–153] Inverted OPVs with PEDOT:PSS treated with different wetting agents present different lifetime behavior in accelerated humidity conditions, thereby showing the crucial influence of processing and HTL/active layer interface formation.[154] Furthermore, Norrman *et al.* have suggested that PEDOT:PSS is the main factor of degradation of inverted OPVs in ambient conditions. They have demonstrated that the phase separation of PEDOT:PSS into PEDOT rich and PSS rich regions and the active layer/PEDOT:PSS interface are the main sources of failure of the long-term lifetime of inverted OPVs.[155]

Therefore, the substitution of the moisture sensitive PEDOT:PSS in inverted OPVs with metal oxide HTLs such as MoO_3, V_2O_5, and WO_3 could be beneficial in some cases concerning stability of inverted OPVs. However, the use of solution processed metal oxides as HTL in inverted OPVs is still challenging, since major processing issues have to be addressed (wettability, annealing temperature, energy level alignment). Recent work has shown that solution-processed MoO_3 can be used to produce efficient and stable normal structure and inverted OPVs when used as a sole HTL, as well as when inserted in addition to PEDOT:PSS. [156–158] Mixing of solution-based MoO_3 with PEDOT:PSS has also yielded efficient inverted solar cells.[159] On the other hand, evaporated metal oxides are still more widely used as HTLs in inverted OPVs, leading in high PCEs with optimum hole selectivity. However, evaporated HTLs are incompatible with roll to roll manufacturing.

MoO_3 is a promising material as a HTL in inverted OPVs in terms of efficiency due to the favorable energy level alignment between its work function and the HOMO of typical active layers in the range of -5.0 eV for polythiophene-based materials.[160,161] Despite the promising developments of inverted OPVs using MoO_3 as a HTL in terms of PCE,

lifetime studies under humidity comparing MoO_3 and PEDOT:PSS HTL in inverted OPVs show that evaporated MoO_3 is also very sensitive to moisture and leads to inverted OPVs with limited lifetime.[162]

The reason is that oxygen and humidity ingress can alter the conductivity and work function of MoO_3.[163,164] On the other hand, the hygroscopic PEDOT:PSS in this architecture can act as a getter and protect the active layer from water interactions with air.[165] Furthermore, MoO_3 may undergo a change in the oxidation state of the Mo (VI) metal under exposure to heat. Under heat conditions, MoO_3 releases oxygen leading to lower Mo oxidation states and a shift in the work function of the oxide.[164,166] Another intrinsic problem of MoO_3 is the photochromic effect which is triggered under exposure to UV light and significantly influences its optical response. The transparency of MoO_3 is considerably reduced influencing the back reflection of the top contact which affect the photocurrent in inverted OPVs.[167] In addition, Voroshazi *et al.* have shown that the transparency reduction of MoO_3 can also occur under heat in dark conditions in inverted OPVs with MoO_3/Ag/Al top contact due to chemical interactions between MoO_3 and Al atoms.[168] Another aspect of the degradation mechanism of inverted OPVs with the aforementioned top electrode was pointed out by Rösch *et al.* through different imaging techniques, whereby they attributed the failure to the migration of silver and diffusion into the MoO_3 layer, changing its work function.[169] Greenbank et al. have shown diffusion of Ag into the active layer and its resulting weakening is correlated to performance decline (specifically V_{oc} reduction) device when used in conjunction with MoO_3 as HTL.[170] However, a full understanding of the stability of MoO_3 HTL in inverted OPVs is still lacking due to the complexity of this material and the varying environmental stress factors that can influence the degradation cause of inverted OPVs with MoO_3 HTL.

Therefore, this chapter aims to analyze the degradation mechanisms of non-encapsulated inverted OPVs using MoO_3 as HTL, under accelerated heat lifetime conditions using the ISOS-D-2 protocol (dark – low RH – 65 °C). As a first step, inverted OPVs using various polymer:fullerene active layers are investigated. Photocurrent mapping measurements provide degradation images at 65°C at various points in time. Secondly, different electrode configurations are investigated for reference P3HT:PC[70]BM polymer-fullerene active layer. Using combinations of two interlayers – MoO_3 and PEDOT:PSS –

at the top electrode of P3HT:PC[70]BM based devices, the device degradation is attributed primarily to the interface between the active layer and MoO_3 and secondly to that between MoO_3 and Ag. Furthermore, alternative reverse engineering methods are used to enhance the assumption that the MoO_3/Ag interface significantly contributes to the degradation of inverted OPVs under heat conditions.

4.2. Materials and Methods

Pre-patterned glass-ITO substrates (sheet resistance 4 Ω/sq) were purchased from Psiotec Ltd. Zinc acetate dehydrate, 2-methoxyethanol and ethanolamine were purchased from Sigma Aldrich, P3HT from Rieke Metals, PTB7 from 1-Material, PC[70]BM from Solenne BV, PEDOT:PSS PH from H.C. Stark, MoO_3 powder from Sigma Aldrich and silver pellets from Kurt J. Lesker.

For the fabrication of inverted OPVs, ITO substrates were sonicated in acetone and subsequently in isopropanol for 10 minutes. Zinc oxide (ZnO) electron transporting layer was prepared using a sol-gel process as described in detail elsewhere.[171] The ZnO precursor was doctor bladed on top of ITO substrates and annealed for 20 min at 140 °C in ambient conditions. After the annealing step a 40 nm ZnO layer is formed as measured with a Veeco Dektak 150 profilometer. The photo-active layers, which are blends of 36 mg/ml in chlorobenzene P3HT:PC[70]BM (1:0.8 by weight), 15 mg/ml in o-DCB DPPTTT:PC[70]BM (1:4 by weight), 25 mg/ml PTB7:PC[70]BM (1:1.5 by weight) were doctor bladed on top of ZnO resulting in a layer thickness of ~180 nm, 100 nm and 90 nm, respectively, as measured with a profilometer. The polymer:fullerene ratios used were chosen from the best performing devices reported in literature.[154,172,173]

For all PEDOT:PSS-based devices a treatment with two wetting agents (Zonyl and Dynol) has been applied as described in detail previously, and will be named as PEDOT:PSS:ZD within the text and figures.[154][174] The P3HT:PC[70]BM-based inverted OPVs were annealed inside a glovebox at 140°C for 20 minutes prior to thermal evaporation of a silver layer with a thickness of 100 nm, resulting in four solar cells, each with an active area of 9 mm^2. For the devices with MoO_3 HTL, 10 nm of MoO_3 was evaporated prior to silver evaporation. For devices using MoO_3 and PEDOT:PSS:ZD as HTL, MoO_3 was evaporated onto the active layer, PEDOT:PSS:ZD doctor bladed onto the MoO_3 layer, followed by silver evaporation. These devices were annealed for another

2 min at 140 °C after PEDOT:PSS:ZD deposition. For devices with PEDOT:PSS:ZD/MoO_3/Ag top electrode the procedure was the same as for PEDOT:PSS:ZD-based devices, except for an extra 10nm MoO_3 layer evaporated on top of the PEDOT:PSS:ZD layer.

The current density-voltage (J/V) characteristics were measured with a Keithley source measurement unit (SMU 2420). For illumination, a calibrated Newport Solar simulator equipped with a Xe lamp was used, providing an AM1.5G spectrum at 100mW/cm^2 as measured by an Oriel 91150V calibration cell equipped with a KG5 filter. Photocurrent measurements were performed under 405 nm laser excitation using a Botest PCT photocurrent system. Thermal aging of the devices has been performed according to ISOS-D-2 protocol, namely, inverted OPVs under test were placed in a dark chamber (Binder) at 65 °C with controlled ambient humidity ~40% and aged for several hours.[175] Their J/V characteristics were measured at different stages of degradation. The devices were un-encapsulated and the lifetime study was started 1 day after device fabrication.

4.3. Results and Discussion

From the initial heat lifetime experiments comparing inverted OPVs comprised of ITO/ZnO/P3HT:PCBM/ with a MoO_3/Ag vs PEDOT:PSS/Ag top electrode, a dramatic drop in all photovoltaic parameters of inverted OPVs using MoO_3 as HTL is observed, after just a few hours under the ISOS-D-2 protocol (65°C, ~40% RH). Therefore, a series of studies were performed aiming at the isolation of the problem and better understanding of the degradation mechanism.

4.3.1. Investigating the degradation mechanisms of inverted OPVs under the ISOS-D-2 protocol using different polymer:fullerene blends and top electrode configurations

In order to obtain a general picture about the heat degradation origins of inverted OPVs, three different polymer:fullerene blends were tested. The inverted OPVs with the following general configuration: ITO/ZnO/polymer:PC[70]BM/MoO_3/Ag or PEDOT:PSS:ZD/Ag were exposed to heat conditions based on the ISOS-D-2 protocol (T = 65 °C, dark, RH = constant ambient ~40%). P3HT:PC[70]BM (1:0.8), PTB7:PC[70]BM (1:1.5), and DPPTTT:PC[70]BM (1:4) were used as the active layers.

The initial (obtained before heat aging) average values of the photovoltaic parameters for the inverted OPVs under study are summarized in Table 4.1.

Table 4.1. **Average absolute photovoltaic parameter values and standard deviation out of 8 inverted OPVs in each case, obtained before initiating the heat aging.**

Inverted OPVs	**Voc (V)**	**Jsc ($mA.cm^{-2}$)**	**FF (%)**	**PCE (%)**
Active layer/MoO_3/Ag				
P3HT:PC[70]BM	0.56 ± 0.01	11.2 ± 0.3	56 ± 2	3.5 ± 0.2
PTB7:PC[70]BM	0.68 ± 0.02	12.5 ± 0.6	47 ± 6	4.0 ± 0.7
DPPTTT:PC[70]BM	0.55 ± 0.01	11.2 ± 0.6	53 ± 4	3.3 ± 0.4
Active layer/PEDOT:PSS:ZD/Ag				
P3HT:PC[70]BM	0.58± 0.01	9.3 ± 0.4	58 ± 3	3.2 ± 0.2
PTB7:PC[70]BM	0.69 ± 0.01	8.3 ± 0.7	50 ± 2	2.9 ± 0.3
DPPTTT:PC[70]BM	0.54 ± 0.01	8.1 ± 1.1	54 ± 1	2.5 ± 0.1

It should be noted that while some of the device performance values presented in Table 4.1 may be below some literature values for the device structure, the purpose of this work is not to produce best-performing "hero" devices.[172,173,176,177] Thus the relative performance values can still be used to obtain a general picture for the degradation behavior of different active layers, comparing PEDOT:PSS and MoO3 HTLs. Figure 4.1 shows the normalized photovoltaic parameters over time of exposure under heat conditions of all the inverted OPVs under study.

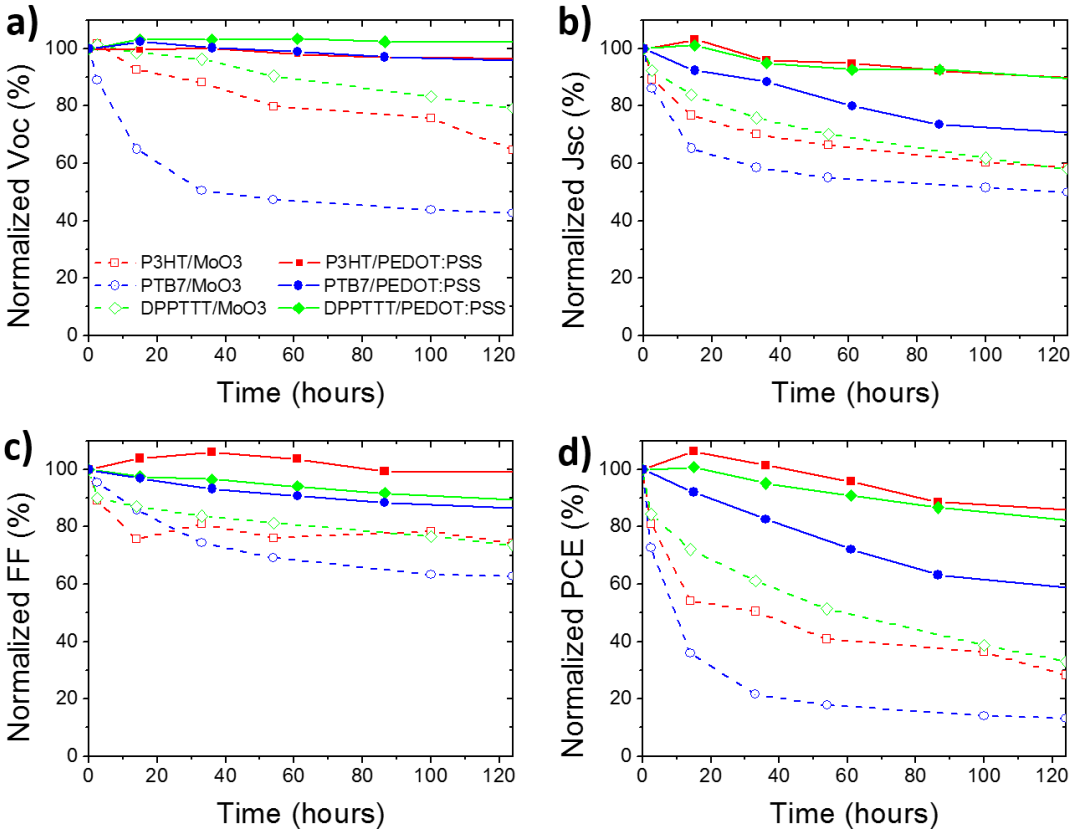

Figure 4.1: Degradation trends of the OPV parameters at 65 °C over time for non-encapsulated inverted OPVs with different active layers: P3HT:PC[70]BM (Red), DPPTTT:PC[70]BM (Green), PTB7:PC[70]BM (Blue) using either MoO3 (dashed lines) or PEDOT:PSS (solid lines) as HTL, plotted as a function of (a) normalized Voc, (b) normalized Jsc, (c) normalized FF and (d) normalized PCE.

From the initial heat lifetime experiment with three different polymers (P3HT, PTB7 and DPPTTT) comparing inverted OPVs comprised of ITO/ZnO/Active Layer/ with a MoO_3/Ag vs PEDOT:PSS/Ag top electrode (Figure 4.1), a dramatic drop in all photovoltaic parameters of inverted OPVs using MoO_3 as HTL was observed, after just a few hours under the ISOS-D-2 protocol (65°C, ~40% RH). In contrast, the lifetime performance of inverted OPVs using PEDOT:PSS as a HTL is significantly better to that observed with MoO_3 for all the different polymer:fullerene blend combinations studied. It is worth noting that all the polymers used in this study are thiophene-based (P3HT, PTB7 and DPPTTT). For PTB7:PC[70]BM-based inverted OPVs, a fast degradation pattern under 85 °C dark heat has previously been observed and been primarily attributed to morphological changes within the active layer.[178] Furthermore, PTB7 has been reported as sensitive to several environmental factors, while DPPTTT has shown greater

stability under light and oxygen, but not under thermal conditions.[172,177,179,180] On the other hand, P3HT:PC[70]BM-based inverted OPVs are known to be resistive to several environmental stress factors and impressive lifetime performances in accelerated and outdoor conditions are demonstrated elsewhere.[181–183]

All the above observations indicate that the incorporation of MoO_3 as HTL at the top electrode of inverted OPVs has a dominant influence on the lifetime performance when subjected to the ISOS D-2 protocol despite the complicated degradation patterns that might also arise due to the variety of active layers. In fact, this study focuses specifically on the electrode configurations in the inverted device structure and the effects of this on the degradation behavior of OPVs. Detailed investigations of the active layer would be beyond the scope of this work. However, the interested reader is referred to the works by Wantz *et al*., Rumer *et al*., Wang *et al*. and Schaffer *et al*. [27,28,183,184] Further analysis in the remainder of this study focus on the understanding of the degradation mechanisms of inverted OPVs using the reference and well optimized P3HT:PC[70]BM as the active layer.

4.3.2. Investigating the degradation mechanisms of P3HT:PC[70]BM/MoO_3-based inverted OPVs under the ISOS-D-2 protocol using buffer layer engineering

In order to visualize this fast degradation of P3HT:PC[70]BM-based solar cells, photocurrent images that map the device active area and its degradation are shown in Figure 4.2. This is a powerful technique that map the developed current in every defined scanned pixel, providing photocurrent distribution mapping image of complete devices.[185] A laser is moved across the device through the transparent electrode giving an indication of defects and therefore possibly diminished device performance. Inverted OPVs using P3HT:PC[70]BM as active layer and MoO_3 as HTL were aged and photocurrent mapping images were extracted at different stages of degradation. The degradation of inverted OPVs with MoO_3 as HTL happens very fast, even after 5 hours degradation under heat, and the photocurrent drops dramatically (see Figure 4.1 and Figure 4.2).

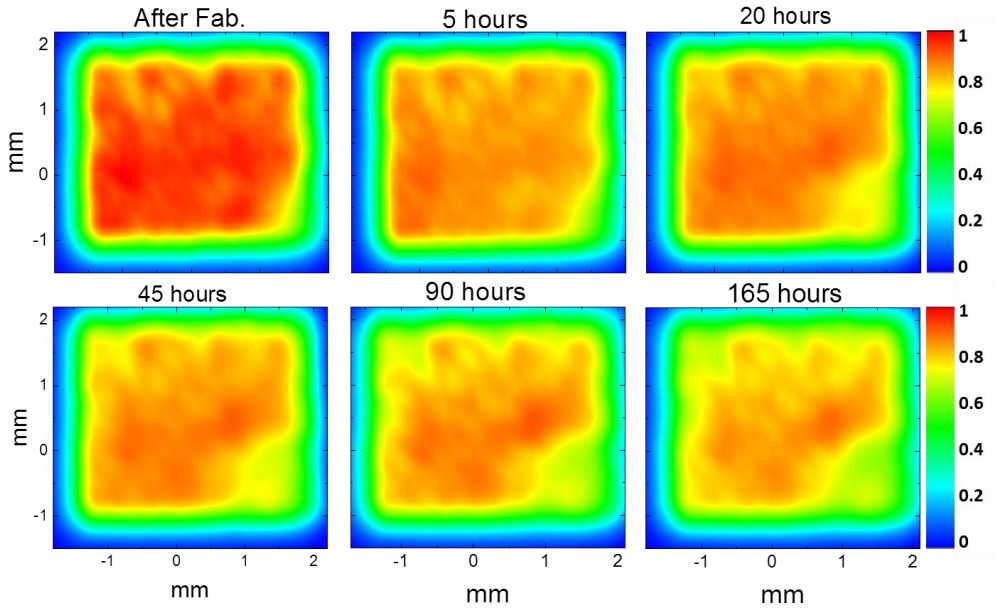

Figure 4.2: Normalized photocurrent mapping images of non-encapsulated inverted OPVs using MoO_3 as HTL in P3HT:PC[70]BM-based solar cells, showing degradation at 65 °C over time of exposure.

The photocurrent mapping measurements indicate that for non-encapsulated inverted P3HT:PC[70]BM solar cells incorporating evaporated MoO_3 HTL, the photocurrent generation drops dramatically in just 5 hours of exposure. The photocurrent intensity observed is significantly less within the whole device area. Despite the obvious drop near the edges of the devices which could be attributed to ingress of air and moisture, the center of the device also shows significantly less photocurrent generation compared to the fresh devices. This is in accordance to Figure 4.1b which shows a fast J_{sc} degradation of P3HT:PC[70]BM/MoO_3 based OPVs within the first few hours of exposure.

To investigate the interfacial interaction of MoO_3 with the P3HT:PC[70]BM active layer, buffer layer engineering was applied to isolate the interfaces under study. Inverted OPVs based on P3HT:PC[70]BM with four different configurations of top electrode –MoO_3/Ag, PEDOT:PSS:ZD/Ag, PEDOT:PSS:ZD/MoO_3/Ag and MoO_3/PEDOT:PSS:ZD/Ag – were tested under 65 °C. The photovoltaic parameters of these devices are shown in Table 4.2.

Table 4.2: Initial photovoltaic parameters and standard deviation of inverted OPVs with different hole transporting layers.

Inverted P3HT:PC[70]BM OPVs using different top electrode configurations	**Voc (V)**	**Jsc ($mA.cm^{-2}$)**	**FF (%)**	**PCE (%)**
PEDOT:PSS:ZD/Ag	0.58 ± 0.01	9.3 ± 0.4	58 ± 3	3.2 ± 0.2
PEDOT:PSS:ZD/MoO_3/Ag	0.57 ± 0.01	10.0 ± 0.5	54 ± 2	3.1 ± 0.2
MoO_3/Ag	0.56 ± 0.01	11.2 ± 0.3	56 ± 2	3.5 ± 0.2
MoO_3/PEDOT:PSS:ZD/Ag	0.55 ± 0.01	8.5 ± 0.7	57 ± 1	2.7 ± 0.3

The inverted OPVs using MoO_3/Ag top electrode show the highest initial efficiency of 3.5%. This is followed by very similar device efficiencies obtained using PEDOT:PSS:ZD/Ag and PEDOT:PSS:ZD/MoO_3/Ag of 3.2% and 3.1%, respectively. Finally, 2.7% PCE is obtained for inverted OPVs with an MoO_3/PEDOT:PSS:ZD/Ag top electrode. Interestingly, these values are comparable to those reported by Wang *et al.* using a solution-based hybrid electrode consisting of MoO_3 and PEDOT:PSS, indicating an efficient bilayer HTL.[159]

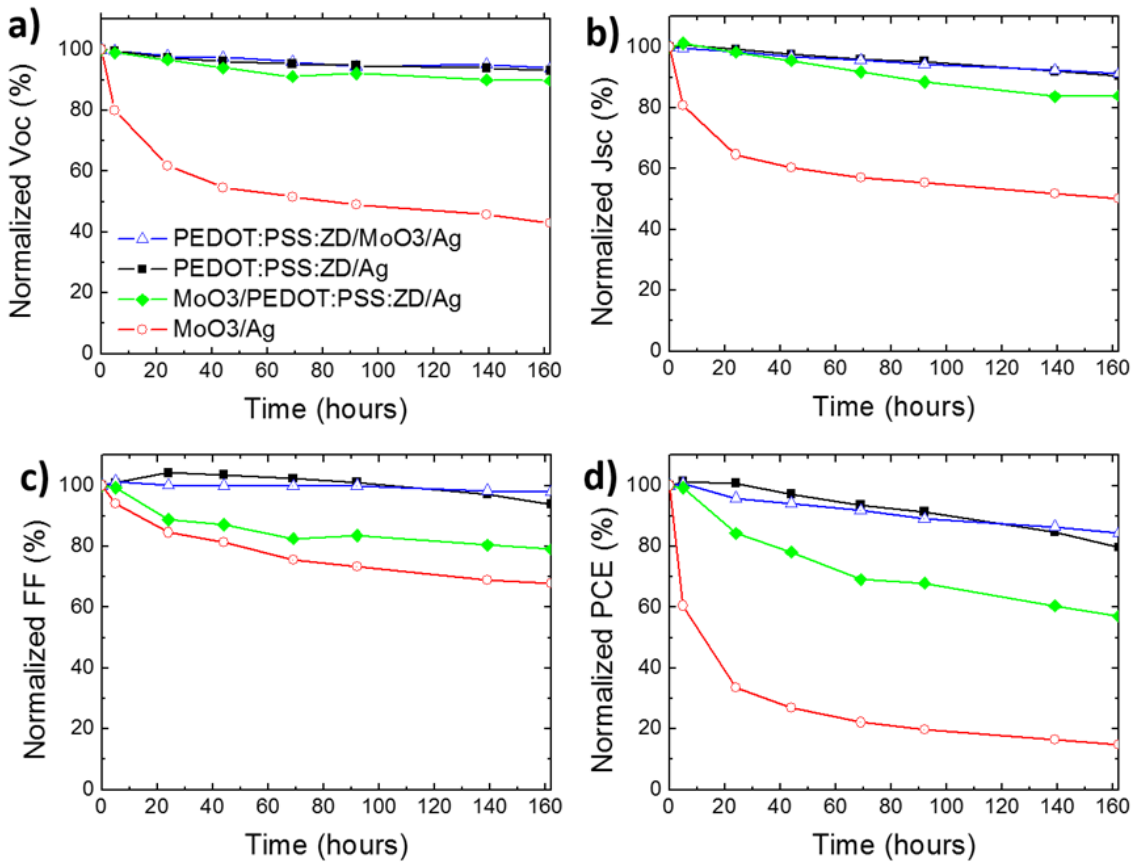

Figure 4.3: Degradation trends of inverted OPVs parameters at 65 °C over time for ITO/ZnO/P3HT:PC[70]BM with different top electrode configurations as a function of (a) normalized Voc, (b) normalized Jsc, (c) normalized FF and (d) normalized PCE.

As shown in Figure 4.3 and in line with the previous observations from Figure 4.1, inverted OPVs using MoO_3/Ag top electrode degrade very fast under heat conditions from the initial efficiency of 3.5% compared to inverted OPVs with PEDOT:PSS:ZD as HTL. As also reported elsewhere, all the J/V parameters exponentially drop without allowing precise identification of the failure mechanism.[186] However, by incorporating a PEDOT:PSS:ZD layer between the active layer and MoO_3 as well as between MoO_3 and Ag, the degradation behavior can be influenced and significant observations can be arised.[187]

Interestingly, the inverted OPVs with MoO_3/PEDOT:PSS:ZD/Ag as a top contact present an intermediate PCE decay between devices with MoO_3 and PEDOT:PSS:ZD as HTL. The majority of the PCE drop on those devices is attributed to FF (Figure 4.3). Thus, it is assumed that the influence on FF in devices with MoO_3/Ag top contact is attributed to the interface of MoO_3 and active layer. By inserting the layer of PEDOT:PSS:ZD between

MoO_3 and Ag, the suppressed decay of those devices indicates that direct contact between the MoO_3 and Ag influences device degradation. Furthermore, the V_{oc} decline of devices with a direct interface between P3HT:PC[70]BM and MoO_3 (organic/metal oxide interface) is more obvious than the devices with P3HT:PC[70]BM and PEDOT:PSS:ZD (organic/organic interface). The latter can again link the failure of the device to the interface of the P3HT:PC[70]BM active layer with MoO_3, as has been reported previously.[186]

On the other hand inverted OPVs with PEDOT:PSS:ZD/MoO_3 HTL present similar lifetime behavior to inverted OPVs with only PEDOT:PSS:ZD as HTL. In that case no obvious degradation is observed when MoO_3 and Ag are in contact. Two possible phenomena could explain this. The first is that carrier selectivity occurs through PEDOT:PSS:ZD and carrier (i.e. hole) collection through MoO_3/Ag, without allowing identification of any degradation caused due to interactions of MoO3-Ag on such devices. This could explain the reduced degradation characteristics observed in the OPVs in which PEDOT:PSS interfaces with the active layer. The second might be that silver migration and diffusion in the active layer through defects of the MoO_3 layer is prevented by inserting the PEDOT:PSS:ZD layer, as assumed elsewhere.[169,170,186] This effect of atoms diffusing into the active layer has been investigated in several works: The Wantz group has observed diffusion of silver atoms in MoO_3 and organic layers.[170,186,188] Additionally, the Österbacka group observed diffusion of MoO_3 into the active layer material causes doping effects that are detrimental to device performance.[189] The findings of this work for the MoO_3/Ag top contact seem to reflect these behaviors. However, since upon insertion of the PEDOT:PSS:ZD layer in inverted OPVs of this study the detrimental effects are slowed down drastically, it is believed that this is a strong indication that indeed the silver top contact also influences these degradation effects.

Therefore, observations made from this experimental approach, reveal that the interfaces between the active layer and MoO_3 as well as between MoO_3 and Ag majorly contribute to the degradation of the P3HT:PC[70]BM inverted OPVs under heat aging conditions, and that both electron blocking as well as diffusion of both MoO_3 and Ag species may play a role in this.

To better understand the above observations on the degradation mechanism, the dark J/V characteristics of the different types of OPVs with different buffer layers at the initial and at different stages of degradation were obtained and are shown in Figure 4.4.

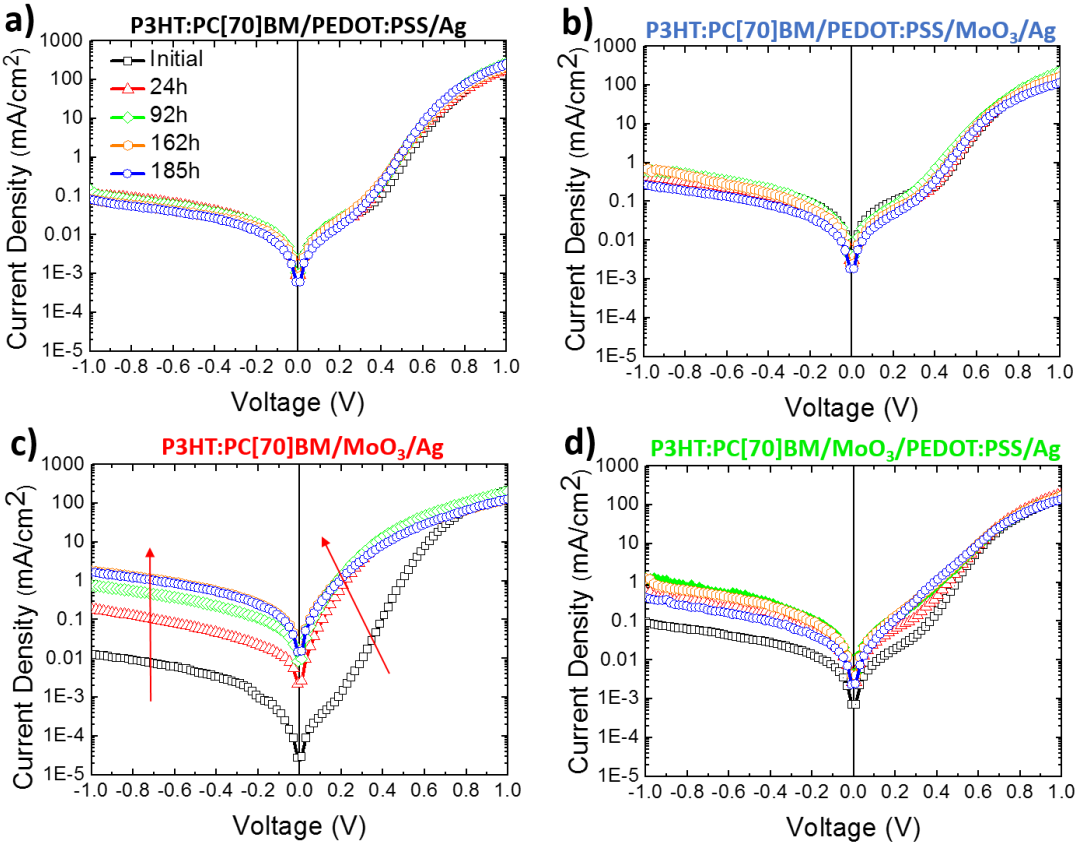

Figure 4.4: Current density versus voltage characteristics (J/V) in dark over time of exposure under heat conditions for inverted OPVs using different hole transporting layers – (a) PEDOT:PSS:ZD, (b) PEDOT:PSS:ZD/MoO_3, (c) MoO_3 and (d) MoO_3/ PEDOT:PSS:ZD.

The inverted OPVs containing MoO_3 HTL as produced and measured in the dark (see Figure 4.4) have low leakage current at reverse bias implying high shunt resistance (Rp). In addition at high forward bias they have high current density and thus low series resistance (Rs) value and therefore their diode-like behavior is better than PEDOT:PSS:ZD-containing devices and accordingly they present higher PCE values, as shown in Table 4.2.

The dark J/V curves of devices with PEDOT:PSS:ZD as HTL show more stable R_s and Rp values, which are slightly improved over time (Figure 4.4). This shows that the organic-organic interface improves over time under heat conditions and that hole transportation is favored at the first stages of degradation. In addition, the performance

(and especially FF) may be assisted by formation of a hole selective thin P3HT layer on top of the active layer under heating.[150]

Figure 4.4b shows the dark J/V for devices with PEDOT:PSS:ZD/MoO_3 as HTL. The Rp of these devices is slightly improved over time whereas Rs is slightly increased over time. It is assumed that the Rp is improved due to changes in the organic/organic interface. However, the slight reduction in Rs is attributed to the interactions of the double interlayers affecting the carrier transportation in the vertical direction.

Inverted OPVs using MoO_3 as HTL show slightly reduced Rs over time of exposure .On the other hand, a significant leakage current and ideality factor increase over time, implying poor diode properties and MoO_3/active layer interactions (Figure 4.4c). The increase in Rp of those devices is more intense and more obvious than the other inverted OPVs under study and it occurs even after some hours of degradation. In addition, the Rp and ideality factor issues over time of exposure are also observed when inverted OPVs using MoO_3/PEDOT:PSS:ZD as HTL are tested (Figure 4.4d). The latter reveals the detrimental influence of the P3HT:PC[70]BM/MoO_3 interface in carrier selectivity.[190] This interfacial interaction over time of exposure promotes high leakage current and high recombination rates resulting in poor Rp and ideality factors which are reflected in FF, as also shown in Figure 4.3.

4.3.3. Investigating the degradation mechanisms of P3HT:PC[70]BM/MoO_3-based inverted OPVs under the ISOS-D-2 protocol using reverse engineering.

To further investigate the degradation mechanism of MoO3/Ag based inverted OPVs a reverse engineering method was applied in order to examine whether these interfacial degradations are reversible. Therefore incomplete device structures were fabricated with ITO/ZnO/P3HT:PC[70]BM and ITO/ZnO/P3HT:PC[70]BM/MoO_3 layer stacks. These were aged at 65 °C prior to the deposition of the subsequent fresh MoO_3/Ag and Ag layers, respectively.

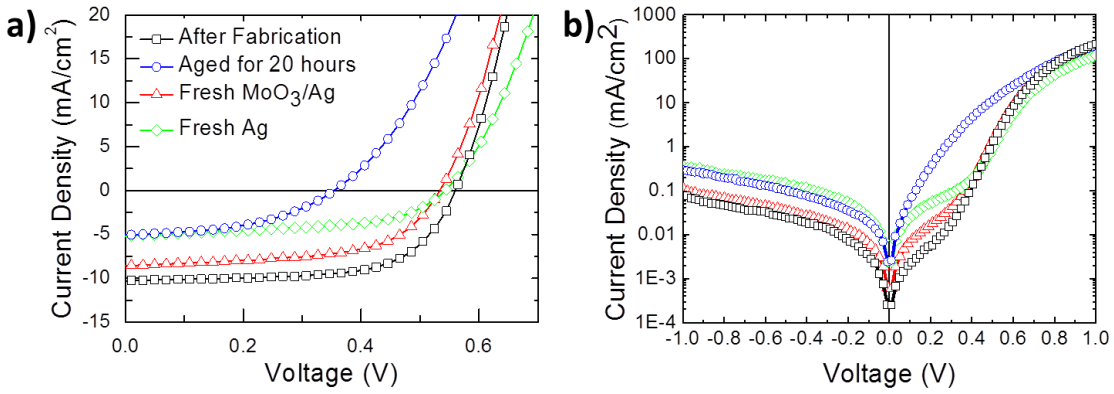

Figure 4.5: (a) Illuminated and (b) dark J/V characteristics of complete devices with MoO_3 HTL as produced (black rectangles) and aged for 20 hours (blue circles). The incomplete layer stacks were aged for 20 hours at 65 °C and then coated with the required fresh electrode. The stacks were ITO/ZnO/P3HT:PC[70]BM, which was coated with fresh MoO_3/Ag (red triangles) and ITO/ZnO/P3HT:PC[70]BM/MoO_3, which was coated with fresh Ag (green diamonds).

Figure 4.5 illustrates the illuminated and dark J/V curves for devices with MoO_3 HTL as produced and after aging for 20 hours at 65 °C. Figure 4.5 also shows the J/V characteristics for devices with degraded stacks after fresh evaporation of the top contact. The findings enhances the aspect that the MoO_3/Ag interface also plays a role in this degradation. After reverse engineering, illuminated J/Vs show the V_{oc} value is recovered when a new MoO_3/Ag is deposited and also when only a new Ag layer is deposited on the ITO/ZnO/P3HT:PC[70]BM/MoO_3 aged stack. This seems to suggest that the MoO_3/Ag interface is responsible for the V_{oc} decay in devices using MoO_3/Ag top contact.[187]

In addition, the rectification of devices with an active layer/MoO_3 interface changes over time and is getting more symmetrical (Figure 4.4c, Figure 4.4d and Figure 4.5b). However, rectification of complete devices based on aged ITO/ZnO/P3HT:PC70BM/MoO_3 upon evaporation of a fresh silver electrode, or aged ITO/ZnO/P3HT:PC70BM with fresh MoO_3/Ag the ideality factor of devices with ITO/ZnO/P3HT:PC70BM/MoO_3 and ITO/ZnO/P3HT:PC70BM aged stacks is recovered (see Figure 4.5) and is similar in shape to the as-produced devices. This is an indicator that in these devices aging of the MoO_3/Ag interface and more specifically Ag is responsible for the change in ideality factor.[186]

However, the fresh evaporation of Ag by itself does not lead to a recovery of J_{sc}. This happens only upon fresh evaporation of both MoO_3 and Ag on the aged stack of ITO/ZnO/P3HT:PC[70]BM. This could be another indication that P3HT:PCBM/MoO_3 interface is responsible for the degraded J_{sc} of the device over time of exposure under heat conditions. Overall, with a freshly evaporated MoO_3/Ag electrode, 90% of the efficiency of the as-produced devices was recovered, which is a clear indication that the device degradation is not affected by ITO/ZnO/P3HT:PCBM interfaces but almost exclusively by the interfaces of the top electrode P3HT:PCBM/MoO3/Ag as shown in Figure 4.5. It should be noted that in principle it was expected to reach the same efficiency with the as-produced devices. However, it is assumed that the exposure to moisture in combination with the heat causes faster degradation and interface modification to the uncapped devices, thereby preventing full recovery by reverse engineering the top contact.

4.4. Conclusion

The lifetime performance of P3HT:PC[70]BM, PTB7:PC[70]BM and DPPTTT:PC[70]BM inverted OPVs using solution processed PEDOT:PSS or thermally evaporated MoO_3 as HTL was monitored under heat conditions according to ISOS-D-2 protocol (T = 65 °C, dark, RH = ambient constant at ~40%). Inverted OPVs using thermally evaporated MoO_3 as HTL presented the most dramatic decay of all OPV parameters under 65 °C even after a few hours of exposure. A series of experiments were performed using photocurrent mapping and different buffer layer engineering methods in order to isolate the interfaces and reveal the failure mechanisms of P3HT:PC[70]BM using MoO_3 as HTL devices under accelerated heat conditions. Upon incorporation of the two compared HTL (evaporated MoO_3 and solution-processed PEDOT:PSS:ZD) in different combinations and configurations in inverted OPVs with the P3HT:PC[70]BM active layer, it was observed that the P3HT:PC[70]BM/MoO_3 interface is the most sensitive part of this degradation triggered at 65 °C. This is primarily shown by the reduction in FF and slower degradation of inverted OPVs with MoO_3/PEDOT:PSS:ZD double interlayer, which isolates the MoO_3 from the Ag. This was in agreement with the dark J/Vs of inverted OPVs, which show the ideality factor of OPVs with the P3HT:PC[70]BM/MoO_3 interface is affected, thereby further revealing the detrimental influence of this interface. After alternative reverse engineering method the V_{oc} and ideality factor of such devices is recovered when fresh Ag is deposited on top of

ITO/ZnO/P3HT:PC[70]BM/MoO_3 aged stacks. This showed that the Ag electrode influences the stability of inverted OPVs with MoO_3 as HTL under heat conditions and was confirmed by the suppressed decay of inverted OPVs using MoO_3/PEDOT:PSS:ZD as HTL.[187]

To conclude, in the case of inverted P3HT:PC[70]BM OPVs with MoO_3/Ag top contact, which were extensively studied in this work by using a series of measurements and device/reverse engineering methods, the results presented indicate that inverted OPV heat degradation is not affected by the ITO/ZnO/P3HT:PCBM interfaces but almost exclusively by the interfaces of the top electrode P3HT:PCBM/MoO3/Ag. The interfaces between the P3HT:PC[70]BM active layer/MoO_3 and MoO_3/Ag are the main origins of failure of inverted OPVs under intense heat conditions of OPVs using MoO3 as HTL, a trend which was observed for the three thiophene-based materials utilized in this study of inverted OPVs. The PEDOT:PSS:ZD HTL resulted in more stable for inverted OPV compared to MoO_3 HTL under ISOS-D-2 heat protocol, a fact which should be taken into account when reporting on high efficiency devices utilizing MoO_3 as HTL. In addition, this study shows the significance of lifetime performance of OPVs with different HTLs. Despite the lower initial efficiency of devices with PEDOT:PSS, OPVs with solution processed PEDOT:PSS HTL present significantly better stability than MoO_3. This is an important parameter which was taken into account for the next chapter where a fully solution processed top electrode is presented consisting of PEDOT:PSS and IJP Ag.

5. Evaporation-Free Inverted Organic Photovoltaics

Inverted OPVs usually use evaporated metal as the top metal electrode. Despite the high-quality electrodes formed by vacuum techniques, their high cost and their incompatibility with large scale production is not applicable for commercialization prospects of cheap OPV devices. Therefore, the need for a solution processed electrode is essential for the up-scalability and the commercialization of OPVs. In the previous chapter it was shown that solution processed PEDOT:PSS HTL has better lifetime stability than an evaporated MoO_3 HTL under heat conditions. However, when the metal electrode it comes to fully solution processed and especially with an inkjet-printed (IJP) silver (Ag) on top of PEDOT:PSS, the interfaces formed between solution processed materials and their impact on initial device performance need further investigation. In this chapter, an investigation of inkjet-printed nanoparticle inks combined with a poly(3,4-ethylenedioxythiophene):poly(styrenesulfonate) (PEDOT:PSS) formulation for solution-processed top electrodes in inverted organic photovoltaics employing the poly(3-hexylthiopehene):phenyl-C61-butyric acid methyl ester (P3HT:PCBM) material system was performed. These results, have suggested that thick (150 nm) highly conductive PEDOT:PSS is required for the design of the solution processed top electrode. Furthermore, a suitable mixture of commercially available Ag nanoparticle inks is proposed to control the printability and electrical conductivity of the solution-processed top electrode. Based on the proposed solution-processed hole-selective contact, a power conversion efficiency (PCE) in the range of 2.9% is reported for evaporation-free inverted OPVs whereas reference device with thermal evaporated Ag exhibited 3.5% PCE.[81]

5.1. Introduction

OPV devices with prolonged lifetime and printing manufacturing are essential for commercialization prospects of solution-based OPV technologies.[34,191–193] One of the important research and development OPV milestones is considered to be the avoidance of high vacuum and temperature deposition such as thermal evaporation of the reflective top electrode. Through the use of solution-processed top electrodes, OPVs can be fabricated in a roll-to-roll production line while simultaneously replacing the energy intensive step of thermal evaporation.[115,194,195]

In the inverted structure the electrons are extracted at the bottom electrode (ITO/n-type metal oxide) and the holes are extracted at the top electrode (Poly(3,4-ethylenedioxythiophene):poly(styrenesulfonate) (PEDOT:PSS/Metal).[196] Inverted OPVs could allow more flexibility on designing the roll to roll production process and thus can provide technological opportunities.[171,197] In addition, inverted OPVs exhibit significantly longer lifetime performance compared to normal structure OPVs, another important parameter for commercialization of such devices.[25,95,198] However most of the high performance inverted OPVs reported in the literature use thermally evaporated metal top electrodes.

Solution processed top electrode is a major challenge in designing economically viable inverted OPVs. Despite the recent progress, in solution-based metal oxide used as hole selective contacts in inverted OPVs.[199–201] PEDOT:PSS is still the most common solution-based hole selective contact in inverted OPVs top electrode, because of its tuneable electronic properties and compatibility with various printing processes.[202–204]

Recent efforts have been reported in the literature to eliminate this high energy consuming processing step for the top electrode of inverted OPVs, such as using spray-coated silver nanowires and high-conductivity PEDOT:PSS as well as screen–printed silver inks.[202,205–207] Furthermore, a relatively thick 800 nm PEDOT:PSS layer has been proposed as hole selective contact suitable for fully solution-processed top electrode.[207] When the Ag top electrode was inkjet-printed on top of this layer, 2% PCE was achieved for OPV devices with an active area of 1cm^2.[207] Galagan *et al.* have proposed that a thin layer of a specific formulation of PEDOT:PSS could be robust enough to protect the underlying layers from the diffusion of solvents.[204] This group have achieved 2.8% PCE

in devices with 40 nm PEDOT:PSS combined with inkjet printed (IJP) Ag as top electrode with an active area of 0.25cm^2.

It was shown that inkjet printing is a suitable method to print Cu and Ag bottom electrodes as a replacement for indium tin oxide (ITO).[133,208,209] However, in order for an inkjet-printed top electrode to serve as a functional replacement for its evaporated counterpart, it must fulfill two crucial requirements: Firstly, it must wet the underlying PEDOT:PSS layer without dissolving it. Secondly, the required electrical properties have to be achieved avoiding high temperature sintering, not compatible with the underlying organic active layers. In this chapter, is reported an investigation of evaporation-free inverted OPVs with an IJP Ag top electrode. Functionality and compatibility studies of PEDOT:PSS derivatives combined with a suitable mixture of silver nanoparticle ink formulations are presented in order to achieve the finest printability and the required electrical conductivity of the solution-processed top electrode. The developed solution-processed top electrode consists of a double layer (~150 nm) high-conductivity PEDOT:PSS with a suitable IJP Ag ink mixture, providing inverted OPVs with PCE in the range of 3%.

5.2. Materials and Methods

For inverted solar cells fabrication, ITO substrates were sonicated in acetone and subsequently in isopropanol for 10 minutes. Zinc oxide (ZnO) electron transporting layer was prepared using a sol-gel process as described elseward.[210] The photo-active layer, a blend of poly(3-hexylthiophene) (P3HT) and phenyl-C61-butyric acid methyl ester (PCBM) (1:0.8 wt%) 36 mg/ml in chlorobenzene, was doctor bladed on top of ZnO resulting in a thickness of ~180 nm as measured with a Veeco Dektak 150 profilometer. All hole selective layers Poly(3,4-ethylenedioxythiophene):poly(styrenesulfonate) (PEDOT:PSS) investigated in this work have been doctor bladed on top of active layers. To ensure good wetting of PEDOT:PSS on top of the hydrophobic P3HT:PCBM layer, a 0.5% mixture of surfactants (Zonyl and Dynol) in a ratio of 5:2 is added.[210] Then devices were transferred in a nitrogen filled glovebox and annealed at 140 °C for 20 minutes followed by thermal evaporation of a silver layer with a thickness of 100 nm.

For the evaporation-free OPV devices, a Dimatix 2800 inkjet printer was employed for Ag ink deposition. The printer parameters were optimized to print a uniform 250 nm Ag

layer with a four-device pattern of 9 mm^2 active area. Three silver inks (EMD5603, ANP and a mixture of the two inks) with different solids concentration and nanoparticle sizes were used for this investigation. EMD5603 ink has <150 nm nanoparticle size and 20% solids content dispersed in ethylene glycol. ANP ink has ~50 nm nanoparticle size and 30-35% solids content dispersed in triethylene glycol monoethyl ether. The third ink is a proposed mixture of 80% EMD5603 Ag ink and 20% ANP Ag ink. The annealing of the photoactive layer P3HT:PCBM for the evaporation-free devices was carried out at 140°C for 20 minutes before the Ag deposition in a nitrogen-filled glovebox. The sintering temperature of the Ag was set at 140 °C for 2 minutes on a hotplate in ambient conditions. The J/V characteristics were obtained using a calibrated Newport solar simulator equipped providing an AM1.5G spectrum at 100 mW/cm^2. All the inverted OPVs under study have the following structure ITO/ZnO/P3HT:PCBM/PEDOT:PSS/Ag. Conductivity measurements were performed using a four point probe setup from Jandel engineering Ltd.

5.3.Results and Discussion

5.3.1. Wetting properties of Ag inks

The reference inverted device used in this study is constituded from ITO/ZnO/P3HT:PCBM/PEDOT:PSS PH/evaporated Ag. ITO and zinc oxide (ZnO) form the bottom electrode which is the electron selective contact. P3HT:PCBM is the photoactive material and PEDOT:PSS PH in combination with thermally evaporated Ag forms the hole selective contact. The aim of the following study is to present recent advances for inverted OPVs with inkjet printed solution processed top Ag electrode. An investigation of different combinations of PEDOT:PSS as well as different Ag inks was performed in order to find the most suitable combination for inverted OPVs with an inkjet-printed top electrode.

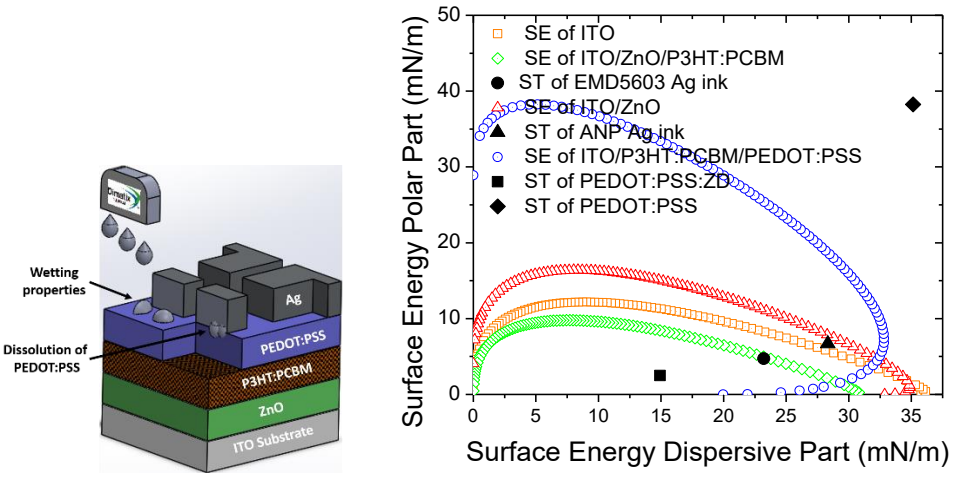

Figure 5.1: **(a) Schematic of inverted structure used in this reported work, from the bottom: ITO/ZnO/P3HT:PCBM/PEDOT:PSS/Ag (b) Surface energy wetting envelopes of ITO (opened rectangles), ITO/ZnO (opened triangles), ITO/ZnO/P3HT:PCBM (opened diamonds),ITO/ZnO/P3HT:PCBM/PEDOT:PSS (opened circles) and surface tensions of PEDOT(PH):PSS (filled diamond), PEDOT(PH):PSS:Z:D (filled rectangle), ANP silver ink (filled triangle), EMD5603 silver ink (closed circle)**

A significant parameter which should be considered for all solution processed OPVs is the wetting properties of the chosen electronic materials. Figure 5.1b shows the wetting envelopes and surface tension values for every electronic material employed within the inverted OPV device structure under study. Based on these measurements PEDOT:PSS surface tension is outside of the wetting envelope of P3HT:PCBM. The latter exhibits

high surface hydrophobicity and in order to ensure good wetting of PEDOT:PSS on top, surfactants are needed as reported elsewhere.[174] The addition of the surfactant mixture significantly improved the wetting properties of PEDOT:PSS and, as expected, the obtained surface tension values were significantly reduced (Figure 5.1b).

Regarding the solution processed metal contact, the surface tension of the two commercially available Ag inks used in this study (EMD5603 and ANP) were measured and are shown in Figure 5.1b. As it can be seen the surface tension values for the silver inks lie well within the wetting envelope of PEDOT:PSS layer (see Figure 5.1b). However, wetting properties of PEDOT:PSS significantly alter as they are affected by the underlying layer (P3HT:PCBM). This affects the printability of silver on PEDOT:PSS. Surface tension values of EMD5603 ink is on the edge of the wetting envelope of P3HT:PCBM and ANP silver ink is outside (Figure 5.1b). The last observation is in agreement with the experimental trials performed to print both aforementioned Ag inks. In addition, due to the high surface tension of ANP ink, pattering and morphological issues arise during printing and sintering. To achieve higher layer quality with ANP Ag ink, it was diluted with isopropyl alcohol (IPA) in a ratio of 1:0.5.

5.3.2. PEDOT:PSS for IJP Ag electrode

The initial trials to fabricate fully solution-processed electrodes, comprised of PEDOT:PSS (50nm)/IJP Ag nanoparticles (EMD 5603) resulted in poor device performance (Figure 5.2b). Diffusion of the inks caused dissolution of the underlying organic layers as previously reported, leading to low electrode selectivity, caused by direct contact of the Ag ink with the semiconducting layer and thus poor inverted OPVs performance. [206,207,211,212]

In order to increase the chemical resistance of PEDOT:PSS, firstly it was investigated the effect of increasing the PSS content in PEDOT:PSS hole transporting layer.[213] However, the experimental trials did not lead to a significant improvement in evaporation free inverted OPV device performance upon inclusion of this higher PSS content as shown inFigure 5.2b and Figure 5.2c.

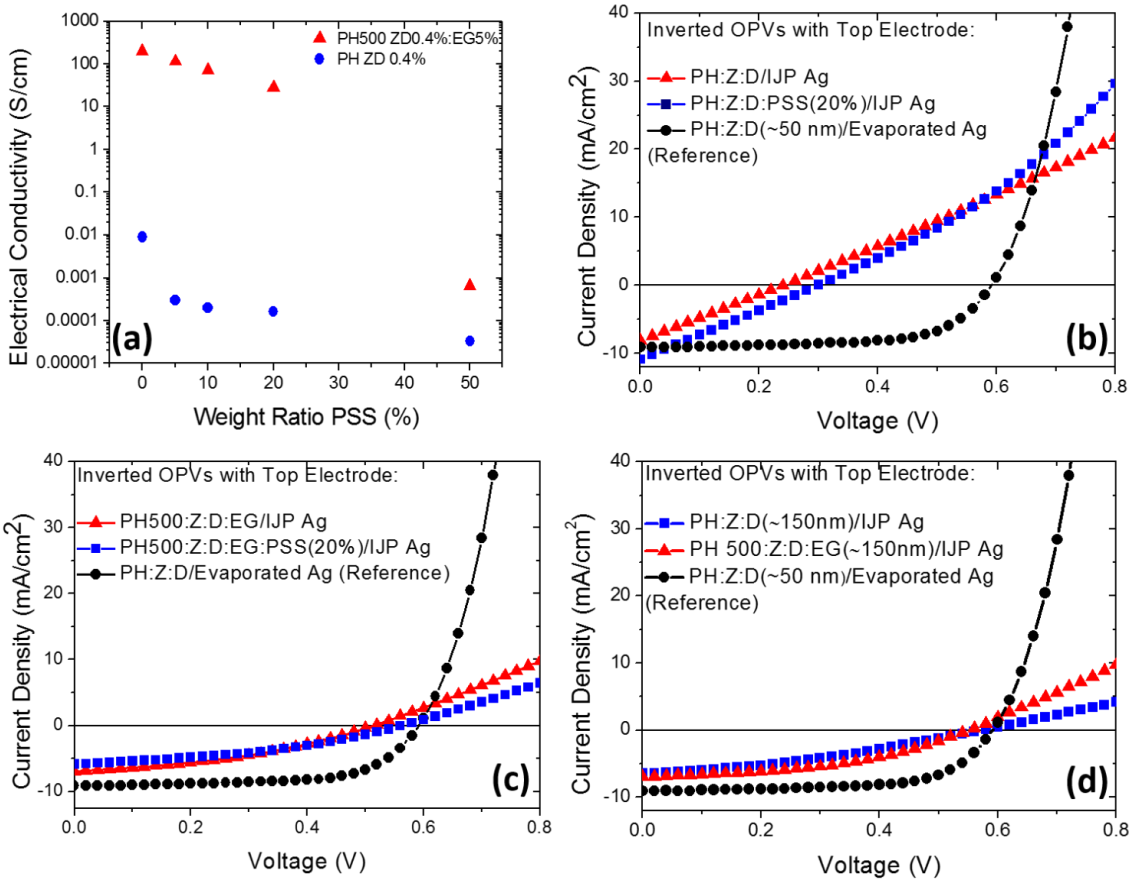

Figure 5.2: **(a) Conductivity of PEDOT(PH):PSS:ZD as a function of PSS content (b) Illuminated J/V characteristics of inverted OPVs with top electrode: ~50 nm PEDOT(PH):PSS:ZD with IJP Ag (EMD5603 ink) (triangles), ~50 nm PEDOT:PSS:ZD:PSS (20%) with IJP Ag (squares) and ~50 nm PEDOT(PH):PSS:ZD with evaporated Ag (circles). (c) Illuminated J/V characteristics of inverted OPVs with top electrode: ~50 nm PEDOT(PH500):PSS:ZD:EG(5%) with IJP Ag (EMD5603 Ag ink) (triangles), ~50 nm PEDOT(PH500):PSS:ZD:EG(5%):PSS(20%) with IJP Ag (squares) and ~50 nm PEDOT(PH):PSS:ZD with evaporated Ag (d) Illuminated J/V characteristics for inverted OPVs with top electrode: ~150 nm PEDOT(PH):PSS:ZD with IJP Ag(EMD5603 ink) (squares), ~150 nm PEDOT:PSS (PH500) with IJP Ag (triangles) and ~50 nm PEDOT:PSS (PH) with evaporated Ag (circles).**

Figure 5.2a demonstrates electrical conductivity measurements performed on all PEDOT:PSS formulations used in this study. The addition of ethylene glycol (EG) in PEDOT:PSS (Clevios PH500) leads to increased electrical conductivity values as described elsewhere.[214] On the other-hand increasing percentage of PSS content in PEDOT:PSS leads to electrical conductivity decrease for both PEDOT:PSS formulations. Figure 5.2c indicates the illuminated J/V characteristics of devices with PEDOT:PSS(PH500):ZD:EG(5%) with and without extra PSS(20%). Due to higher conductivity PEDOT:PSS(PH500):ZD:EG(5%) with and without increased PSS content

provides better hole selectivity than the PEDOT PH when combined with Ag printed inks for evaporation-free top electrodes. The addition of PSS content does not eliminate the diffusion issues involved during the processing and sintering procedure, and thus resulting in inverted OPVs with poor top electrode selectivity.

A second approach which can be followed to reduce diffusion of Ag ink formulation into the active layer is the deposition of thicker PEDOT:PSS layers.[207] The two aforementioned PEDOT:PSS formulations with different conductivities were used and compared. A 150 nm double layer PEDOT:PSS for each formulation was used in combination with IJP EMD5603 Ag ink to form the solution processed top electrode. The J/V characteristics in Figure 5.2d show that by increasing the thickness of PEDOT:PSS, functional electrodes can be achieved using both PEDOT:PSS derivatives as hole selective contacts. Conductivity issues are critical for solution-processed top electrodes. PEDOT:PSS PH500 with 5%vol ethylene glycol has 230 S/cm conductivity as measured with four point probe. This value is approximately five orders of magnitude higher than the conductivity measured for PEDOT PH (0.01 S/cm). Both approximate 150 nm thick PEDOT:PSS formulations [(PEDOT:PSS(PH):ZD and PEDOT:PSS(PH500):ZD:EG(5%)] resulted in functional evaporation-free inverted OPVs. Figure 5.2d shows the illuminated J/V characteristics for the devices under study. Based on this study, the PEDOT:PSS (PH500) based formulation provides slightly better fill factor (FF) and series resistance (Rs) values as well as better reproducibility compared to PEDOT:PSS (PH) based formulations for evaporation-free inverted OPVs.

5.3.3. Metal nanoparticle inks

The conductivity limitations also arise due to processing requirements of the IJP Ag nanoparticle top electrodes within the inverted OPV structure. The FF of evaporation-free OPVs is much lower compared to the reference inverted OPVs using low-conductivity PEDOT:PSS (PH) hole selective contact. One of the reasons for the lower FF of the evaporation-free inverted OPVs could be the low conductivity of the EMD5603 Ag IJP top electrode. The sintering temperature value is limited by the functional properties of the active layer. The sintering has to be carried out at a maximum of 140°C to avoid negative influence on the performance of P3HT:PCBM active layer. Thus, the conductivity of the particular Ag ink cannot reach higher values as its conductivity is strongly dependent on the optimized OPV processing temperature. Thus, the other critical

parameter that can be modified to improve the conductivity values is the metal nanoparticle size. A high sintering temperature provides higher conductivity and a smaller nanoparticle size can provides lower curing temperature.[133] Therefore, ANP inkjet-printed layers are expected to provide higher conductivity at 140°C due to the smaller nanoparticle sizes they contain.

From a printability point of view, EMD5603 prints well on PEDOT:PSS in contrast with ANP which presents some morphological and patterning issues during the printing and sintering process. During inkjet printing, the ANP ink accumulated in the center of the printed pattern due to its high surface tension and its high solid concentration. During the sintering of ANP ink, a flow from the edges to the center was observed and most of the Ag was accumulated in the center. This effect was mentioned elsewhere as Maragoni flow which is generated during the drying of the printed ink.[112] The inverse flow when ink flows from the center to the edges is well known as capillary flow. These flows depends on solvents concentration (surface tension-boiling point) and sintering temperature.[46] In order to overcome this problem and balance the flows generated during the drying of ink, ANP was diluted with IPA in a 1:0.5 ratio since the sintering temperature was kept constant at 140 °C for two minutes. Based on this formulation the inkjet printing parameters of ANP can be improved but not fully resolved.

To address the above critical issues, it is proposed within this paper an ink mixture which can provide solution-based current-collecting electrodes that combine the printability of EMD5603 with the electrical properties of ANP. ANP ink exhibits higher conductivity (35190 S/cm) than EMD5603 (25446 S/cm) ink sintered at 140°C as measured using the four point probe method. The optimized ink mixture consists of 80% EMD5603 and 20% ANP ink demonstrates good printability and slightly higher conductivity values (37713 S/cm) compared with pristine ANP and EMD inks.

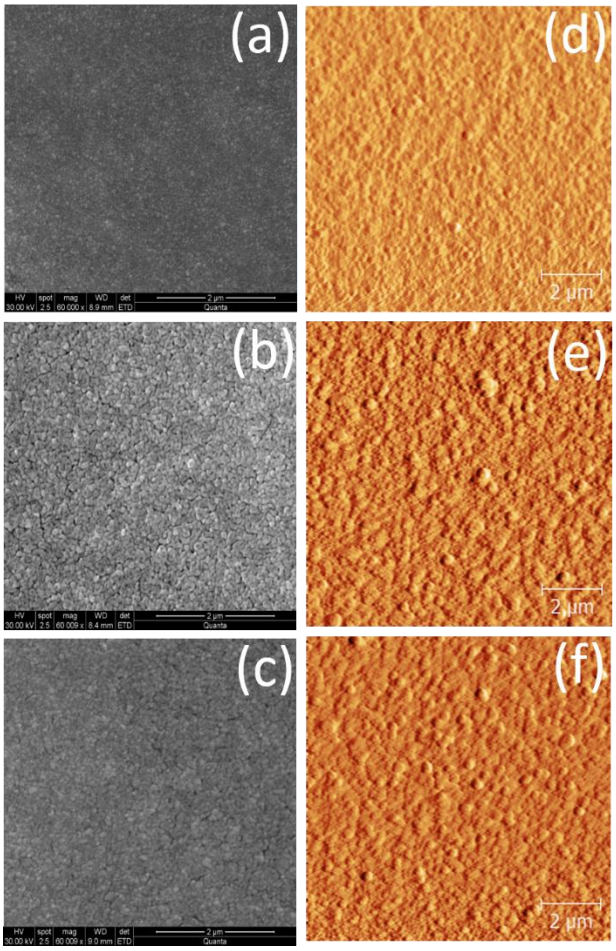

Figure 5.3: **SEM ((a),(b), (c)) and AFM ((d), (e), (f)) images of inkjet-printed EMD5603 Ag ink ((a), (d)), ANP:IPA (1:0.5) Ag ink ((b), (e)) and Ag ink mixture ((c), (f)) on glass. The scale bar for all images is 2 µm.**

In order to examine the surface topography of the Ag inkjet-printed inks, scanning electron microscopy (SEM) and atomic force microscopy (AFM) studies were performed. Figure 5.3 shows SEM and AFM images for the three different silver inks sintered at 140°C for 2 minutes.Figure 5.3a and Figure 5.3d represents EMD5603 Ag IJP layers, showing smaller cluster sizes whereas ANP IJP layers show larger clusters (Figure 5.3b, Figure 5.3e, Figure 5.3c and Figure 5.3f), then, seems to show both cluster sizes seen for EMD5603 and ANP ink.

As previously reported the Ag cluster size and the agglomeration is depend on the sintering temperature and has influence on the conductivity.[215–218] Small nanoparticles have lower curing temperature and thus are able to growth more than the large nanoparticles at 140°C. The ink mixture contains small (~50 nm) and large (~150 nm) nanoparticle sizes, it is suggested that this combination of small and large nanoparticles

can form a better carrier transportation network than EMD5603 ink leading also to slightly higher conductivity values compared to the ANP ink. More importantly, the proposed Ag ink mixture eliminates printing processing limitations providing functional top contact and intimate interfaces for the solution processed top electrode.

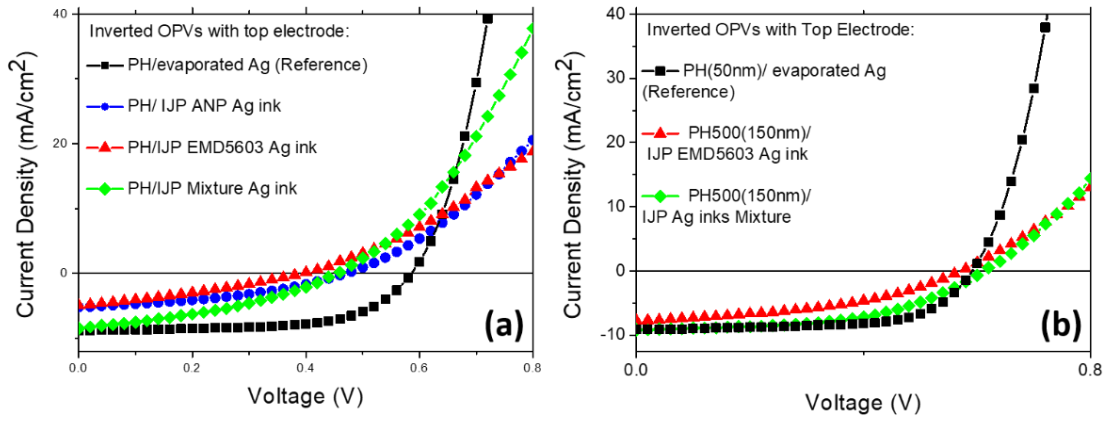

Figure 5.4: (a) Illuminated J/V characteristics of inverted OPVs with top electrode PEDOT:PSS(PH):ZD and IJP Ag with EMD5603 ink (red triangles), ANP:IPA (1:0.5) ink (blue squares) and Mixture ink (green diamonds) and evaporated Ag (black circles). (b) Illuminated J/V characteristics of inverted OPVs with top electrode: ~150 nm PEDOT:PSS(PH500):ZD:EG(5%) and IJP Ag Mixture (red diamonds), 150 nm PEDOT:PSS(PH500):ZD:EG(5%) and IJP Ag with EMD5603 ink (red triangles)and ~50 nm PEDOT:PSS(PH):ZD evaporated Ag (circles)

In order to compare the different ink formulations with the evaporated Ag, the three different ink formulations (EMD5603, ANP and ink mixture) have been inkjet-printed on the reference ~50 nm PEDOT:PSS(PH):ZD layer. Comparing the three evaporation-free inverted OPVs, the best PCE value is achieved using the ink mixture as shown in Figure 5.4a. OPVs using ink mixture have shown better Jsc and FF values than the other two inks in study. Figure 5.4b illustrates the illuminated J/V characteristics of IJP Ag inks printed on the optimized ~150 nm PEDOT:PSS (PH500). Note that OPV curve which represent IJP ANP based OPVs is not included since the devices were shunted in this particular run. This is another one indication showing the bad printability of ANP ink for this work requirements.

Table 5.1: **PCE performance parameters of the reference (evaporated Ag) inverted OPVs and the optimum evaporation-free inverted OPVs with IJP Ag.**

OPV	Voc (V)	Jsc (mA/cm^2)	FF (%)	PCE (%)
Reference	0.59	9.1	65	3.5
IJP	0.61	9.2	51	2.9

When then combining the previously established 150 nm layer of PEDOT:PSS (PH500):ZD:EG(5%) with the Ag ink mixture, the resulting J/V characteristics are shown in Figure 5.4b together with the reference inverted OPVs using evaporated silver top electrode and PEDOT:PSS(PH):ZD-(50 nm) hole selective contact. The evaporation-free inverted OPVs containing IJP Ag (ink mixture) top electrodes only show slightly lower PCE compared to the optimized reference inverted OPVs. The PCE parameters such as V_{oc} and J_{sc} have similar values as shown in Table 5.1. The main drop is observed in the FF which is 65% in the reference inverted OPVs and 51% for the optimum evaporation-free inverted OPVs. Despite the above limitations on the hole carrier selectivity of the proposed solution-processed top electrode for inverted OPV performance, a 2.9% PCE has been achieved for evaporation-free inverted OPVs using the proposed 150 nm and highly conductive PEDOT:PSS formulation combined with the proposed IJP Ag ink mixture. PCE reduction is expected for larger than $1cm^2$ active area devices due to a likely increase in series resistance (Rs) as experimentally studied by P. Kopola et al.[115]

5.4. Conclusion

In summary, the fabrication of the solution-processed top electrode in inverted OPV devices was investigated. The crucial points which deserve consideration during the fabrication of solution-processed top electrodes are each layer's wetting properties and the prevention of dissolving of the underlying layers. The electronic properties, printing parameters and intimate interfaces are shown to be critical for achieving high performance solution-processed top electrodes. A double layer of PEDOT:PSS(PH500):ZD:EG(5%) with overall thickness of approximately 150 nm, can provide a functional hole selective contact for solution-processed top electrodes and can be used to partly resolve the limitations caused by diffusion of the Ag ink formulation in PEDOT:PSS. However, there are still many critical challenges that need to be overcome in order to eliminate diffusion issues on the way to achieving high performance solution-processed top electrodes for long lived evaporation-free inverted OPVs.

Importantly, by mixing suitable Ag inks with different nanoparticle sizes and curing temperature, it was shown that adequate conductivity and inkjet printing processing properties at sintering temperatures compatible with the requirements of inverted OPVs solution processed requirements, can be achieved. For all the experimental runs performed for the purpose of this work using different PEDOT:PSS hole selective contacts, the ink mixture showed that could be used to improve the PCE inverted OPVs incorporating solution-processed top electrode. The resulting evaporation-free inverted OPVs reached 2.9% PCE in comparison to the optimized reference inverted OPVs exhibiting PCE of 3.5%.

6. Future Work

This thesis sets the baselines for the development and characterization of up-scalable solution processed electrodes of OPVs. This work will be continued toward the development of ITO-free and evaporation-free stable and up-scalable electrodes for efficient OPVs. A brief overview of the future work is followed.

6.1. Doped metal oxides investigation for up-scalable OPVs

Metal oxides have been extensively used as n-type or p-type buffer layers in OPVs due to their high transparency, relatively high conductivity, tunable work function and solution processability. Furthermore, the advantage of solution processing of these materials at low temperatures provide opportunities for up-scalability of OPVs. Solution processed doped metal oxides with improved conductivities could meet the routes for up-scalable OPVs since thicker layers (100-200 nm) can be deposited without affecting significantly the transparency and conductivity of the layer. A lot of studies have shown that PFN or PEI (Polyethylenimine) modification of oxide materials by several methods such as dipping, bi-layer or as additive in the precursor improve the device performance and stability of OPVs.[219–223] More specifically, they have shown that PEI improve the morphology and structural order of ZnO and thereby the electron mobility in the vertical direction. Most importantly PEI is widely used to reduce the work function of metal oxides (and consequently the work function of bottom electrodes of inverted OPVs) and thereby assist in band alignment.[224] As a result, incorporation of such layers enhance the device performance of OPVs mainly due to improved FF values.

Figure 6.1 shows the illuminated JV characteristics of inverted OPVs with different ETL and the following device configuration: ITO/ETL/P3HT:PCBM/MoO_3/Ag. The preliminary results of this work have shown that inverted OPVs using a sole antimuonium doped tin oxide (ATO) used as n-type buffer layer function as a resistor (Figure 6.1) showing that an energetic barrier is created at the bottom electrode. Moreover, OPVs without ETL have presented 1.4% PCE whereas OPVs with PEI (3-5nm) as ETL (or modification of ITO with PEI) have shown an improvement in device performance and a PCE of 2.9% (Table 6.1). Interestingly, the ATO/PEI nanocomposite has performed efficiently as n-type buffer layer in inverted OPVs and PCEs in the range of 3.8% were achieved. According to the above observations, the improved PCE could be attributed to

a work function reduction of the ATO layer. Furthermore, by increasing the thickness of doped oxide at 120 nm the performance is still high (3.7% PCE) showing that the incorporation of PEI does not affect conductivity of the doped oxide and provide opportunities for the usage of this material for up-scalability purposes. This preliminary study will be extended to further understanding the properties of ATO/PEI and the mechanism of work function shifting. Further studies on lifetime performance of inverted OPVs comparing ATO/PEI, ZnO (reference), ZnO/PEI, AZO (most widely used doped oxide) and AZO/PEI will be performed.

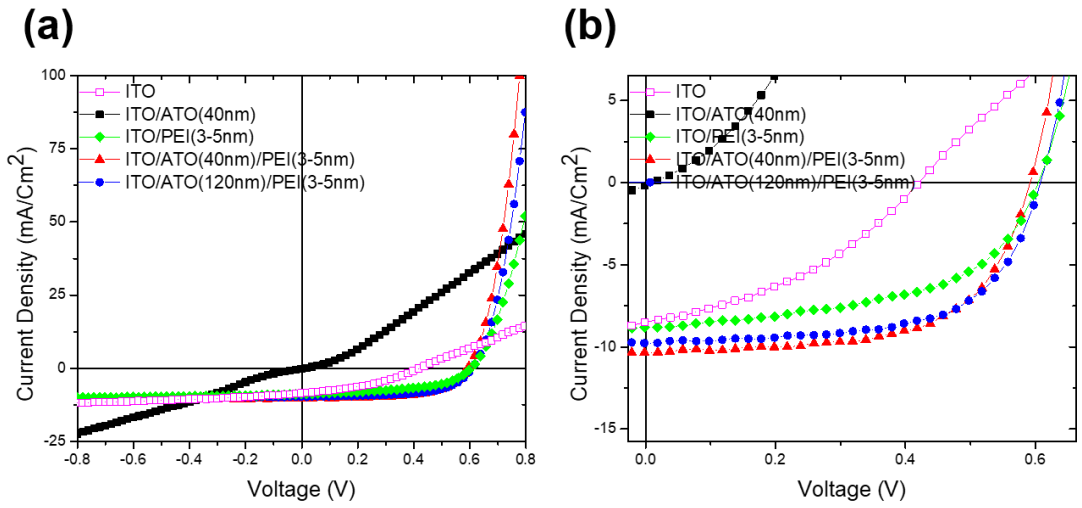

Figure 6.1: (a) Illuminated JV characteristics of inverted OPVs with ETL: ATO (black squares), ATO(40nm)/PEI (red rectangles), ATO(120nm)/PEI (blue circles), PEI (green diamonds) and without ETL-ITO only (magenta squares). (b) magnification

Table 6.1: JV parameters of inverted OPVs with ETL: ATO(40nm), ATO(40nm)/PEI, ATO(120nm)/PEI, PEI(3-5nm) and without ETL (ITO only).

OPVs with ETL:	V_{oc} (V)	J_{sc} (mA.cm^{-2})	FF (%)	PCE (%)
ITO	0.42	8.5	39	1.4
ITO/ATO	-	-	-	-
ITO/PEI	0.60	8.6	56	2.9

ITO/ATO 40nm/PEI	0.60	10.3	61	3.8
ITO/ATO 120nm/PEI	0.62	9.8	61	3.7

6.2. ITO-free and evaporation-free high efficient OPVs

Normal structure OPVs with ITO-free electrode with IJP metal grid use PEDOT:PSS as HTL and as conductivity enhancer of the electrode. ITO-free inverted structure OPVs with IJP metal grid also use PEDOT:PSS as electrode enhancer and an ETL on top of the IJP metal grid/PEDOT:PSS electrode. Replacing PEDOT:PSS with doped metal oxide could be beneficial for product development targets since several issues arise due to its hygroscopic and acidic nature. Other studies have shown the implementation of doped oxides on Ag nanowire but to the best of my knowledge, IJP metal grids combined with a doped metal oxide have not been reported. Doped oxide should have high transparency (>80%) and high conductivity (0.01-200 S/cm) at high thicknesses and low annealing temperature in order to be used in conjunction with the IJP metal grid and substitute the PEDOT:PSS layer. Furthermore, the formation of doped oxide on IJP line morphology is another challenge that need further investigation but as it was shown in chapter 3 the embedding procedure can be used to control grid morphology. Therefore, a study to combine a highly conductive IJP Ag electrode with a doped metal oxide (AZO, ATO/PEI) will be performed and their effect on device performance and stability will be investigated.

In Chapter 3 the limitations arise during the processing of IJP Cu grid as a bottom electrode in OPVs were reported. The oxidation reactivity of Cu-grid at elevated temperatures revealed as the main drawback of Cu grid based OPVs. This has a major influence on the performance and the stability of Cu-grid based OPVs during the fabrication process of OPVs since most of the materials (active layers, HTL and ETL) consisting an OPV require annealing treatment. A solution to this problem could be a protecting layer on top of Cu grid in order to protect them from oxygen interactions in air during processing. The effect of conductivity of Cu at elevated temperatures incorporating different types of protecting layers will be investigated. In addition, mixing

of copper nanoparticles with other noble metal nanoparticles in a core-shell structure could be another potential solution to the oxidation instability of IJP Cu.

Novel non-fullerene acceptor materials (such as ITIC and IDTBR) have already been used with newly synthesized conjugated polymeric donors (such as PTB7-th and PBDBT) achieving efficiencies that exceed 10%. This remarkable progress in terms of device efficiency demonstrates the potential of large scale production of OPVs. The main goal of this study will be the design of efficient solution processed electrodes adopting the ITO-free and evaporation-free concepts of this thesis as well as incorporating other deposition techniques and electrode materials. The electrodes will be designed according to the up to date most efficient donor/acceptor system in order to achieve high efficient solution processed OPVs. OPVs will be fabricated with roll to roll compatible techniques and tested under ISOS protocols in indoor and outdoor conditions.

7. Conclusions

The ability to fabricate ultrathin, lightweight, flexible and low-cost photovoltaics trigger the research community and industries in a depth investigation of OPVs during the last two decades. The three main pillars of commercialization of OPVs is efficiency, stability and fabrication cost. The avoidance of high vacuum, energy intensive techniques and high cost materials are necessary requirements for the up-scalability and roll to roll production of this technology. This thesis has demonstrated routes toward solution processed electrodes showing the potential for fully solution processed OPVs.

Chapter 3 of this thesis demonstrates ITO-free normal structured OPVs based on IJP Cu grid/highly conductive PEDOT:PSS electrode. Cu ink is much cheaper than Ag ink which is the metal ink with dominant use in IJP electrodes for OPVs. Therefore, Cu have attracted a lot of attention during the last years. The oxidation reactivity of Cu is the main drawback of Cu nanoparticle ink. However, a lot of progress has been made in the development of Cu inks and in the sintering methods to produce high conductivity Cu grid structures. In this work, high quality IJP Cu lines with desired conductivity values were achieved through printing parameters and sintering optimization. Despite the decent PCE values achieved with non-embedded IJP Cu grid (3.4%) compared with the reference ITO-based device (4.9%), limitations arise during the processing of OPVs fabrication. More specifically, during the necessary annealing step of PEDOT:PSS at 140 °C in air, Cu oxidizes due to its high oxidation reactivity at elevated temperatures. As a result, the conductivity of Cu is reduced and highly conductive PEDOT:PSS was combined in order to compensate this conductivity loss and enhance the overall conductivity of the electrode. Cost effective ITO-free OPVs with 3.4% PCE were achieved with IJP Cu grid/PEDOT:PSS as the bottom electrode whereas the reference exhibited 4.9% PCE. Furthermore, the efforts to embed Cu grid electrode in a transparent resin with a reverse nanoimprinting method are presented. Embedding of Cu grid could reduce electrode transmittance losses and improve OPV performance parameters since lower R_p values were expected for flat line surfaces. In addition, the embedding procedure followed could provide opportunities also for other applications (sensors, light emitting diodes, RFID antennas) since optimized sintered Cu from glass substrate can be transferred to flexible substrates avoiding shrinkage of the plastic substrate due to the excess heat during laser sintering. However, the results with embedded IJP Cu grid have not improved the

performance possibly due to the complication and lack of reproducibility of the embedding procedure with small substrates. Further optimization or alternative embedding methods could be beneficial for OPVs and for other applications.

The next Chapters (Chapters 4 and 5) are focused on the top electrode of inverted structured OPVs which is more stable and could provide technological opportunities since Ag top electrode could be deposited through solution processed techniques. In chapter 4, the influence of thermal stability of a solution processed HTL (PEDOT:PSS) compared with an evaporated HTL (MoO_3) is demonstrated under the ISOS-D2 at 65°C. The PCE of inverted OPVs that use MoO_3 as HTL drops dramatically even after a few hours of exposure to heat. Significant observations were extracted during the identification of the failure mechanism of inverted OPVs with MoO_3 under heat through buffer layer and device engineering methods. The P3HT:PCBM/MoO_3 interface as well as MoO3/Ag contribute to the fast degradation of inverted OPVs with MoO_3 as HTL. Indeed, PEDOT:PSS has been proved one of the most vulnerable parts in inverted OPVs. However, replacing of PEDOT:PSS is still a challenging task since alternative HTL such as metal oxides need further investigation not only in PCE but also in stability. It has been concluded that solution processed PEDOT:PSS has significantly better lifetime performance than evaporated MoO_3 under heat conditions (65°C, ISOS-D2).

Chapter 5 is based on a fully solution processed top electrode of inverted OPVs consisting with an IJP Ag combined with highly conductive PEDOT:PSS HTL as a top electrode in inverted OPVs. The most significant challenges that arise when an evaporated electrode comes to a fully solution processed electrode is the wetting properties of the materials used on top of the active layer, the dissolution of the underlying layers and the sintering temperature of the metal top contact. It was concluded that thick PEDOT:PSS layer is required in order to block the diffusion of solvents contain in Ag ink. In addition highly conductive formulation (PH500 PEDOT:PSS) is required in order to enhance the conductivity of the electrode. Furthermore, by mixing two commercially available Ag inks (80%EMD+20%ANP) with different nanoparticle size the printing parameters were controlled, and desired conductivity values were achieved providing efficient carrier transportation network and intimate interfaces. PCE of 2.9% was achieved for inverted OPVs with fully solution processed electrode whereas the reference evaporated Ag electrode based OPVs exhibited 3.5 % PCE.

To conclude, a transparent electrode is developed based on IJP Cu lines grid/highly conductive PEDOT:PSS showing the potential for a cost effective solution processed photovoltaics. Lifetime performance studies have shown that OPVs with PEDOT:PSS as HTL are more stable than MoO_3 HTL under heat conditions showing that replacement of PEDOT:PSS is not an easy task and lifetime performance factors should be taken into account. Finally, an efficient fully solution processed top electrode, based on highly conductive thick PEDOT:PSS combined with IJP Ag, for inverted OPVs was designed.

8. References

[1] A.E. Becquerel, Photoelctrochemical effect, Compt. Rend. Acad. Sci. 9 (1839) 145.

[2] W.G. Adams, R.E. Day, The Action of Light on Selenium., Proc. R. Soc. London. 25 (1876) 113–117. doi:10.1098/rspl.1876.0024.

[3] C.E. Fritts, On a new form of selenium cell, and some electrical discoveries made by its use, Am. J. Sci. s3-26 (1883) 465–472. doi:10.2475/ajs.s3-26.156.465.

[4] D.M. Chapin, C.S. Fuller, G.L. Pearson, A new silicon p-n junction photocell for converting solar radiation into electrical power, J. Appl. Phys. 25 (1954) 676. http://link.aip.org/link/doi/10.1063/1.1721711.

[5] M.A. Green, Y. Hishikawa, E.D. Dunlop, D.H. Levi, J. Hohl-Ebinger, A.W.Y. Ho-Baillie, Solar cell efficiency tables (version 51), Prog. Photovoltaics Res. Appl. 26 (2018) 3–12. doi:10.1002/pip.2978.

[6] C.W. Tang, Two-layer organic photovoltaic cell, Appl. Phys. Lett. 48 (1986) 183. doi:10.1063/1.96937.

[7] H. Shirakawa, E.J. Louis, A.G. MacDiarmid, C.K. Chiang, A.J. Heeger, Synthesis of electrically conducting organic polymers: halogen derivatives of polyacetylene, (CH) x, J. Chem. Soc. Chem. Commun. (1977) 578. doi:10.1039/c39770000578.

[8] S. Mori, H. Oh-oka, H. Nakao, T. Gotanda, Y. Nakano, H. Jung, A. Iida, R. Hayase, N. Shida, M. Saito, K. Todori, T. Asakura, A. Matsui, M. Hosoya, Organic photovoltaic module development with inverted device structure, MRS Proc. 1737 (2015) mrsf14-1737-u17-02. doi:10.1557/opl.2015.540.

[9] C.H. Peters, I.T. Sachs-Quintana, J.P. Kastrop, S. Beaupré, M. Leclerc, M.D. McGehee, High Efficiency Polymer Solar Cells with Long Operating Lifetimes, Adv. Energy Mater. 1 (2011) 491–494. doi:10.1002/aenm.201100138.

[10] R. Søndergaard, M. Hösel, D. Angmo, T.T. Larsen-Olsen, F.C. Krebs, Roll-to-roll

fabrication of polymer solar cells, Mater. Today. 15 (2012) 36–49. doi:10.1016/S1369-7021(12)70019-6.

[11] V.I. Arkhipov, H. Bässler, Exciton dissociation and charge photogeneration in pristine and doped conjugated polymers, Phys. Status Solidi A. 201 (2004) 1152–1187. doi:10.1002/pssa.200404339.

[12] C. Deibel, V. Dyakonov, C.J. Brabec, Organic Bulk-Heterojunction Solar Cells, IEEE JSTQE. 16 (2010) 1517–1527. doi:10.1109/JSTQE.2010.2048892.

[13] C. Deibel, V. Dyakonov, Polymer–fullerene bulk heterojunction solar cells, Rep. Prog. Phys. 73 (2010) 96401. http://dx.doi.org/10.1088/0034-4885/73/9/096401.

[14] G. Yu, J. Gao, J.C. Hummelen, F. Wudl, A.J. Heeger, Polymer photovoltaic cells: enhanced efficiencies via a network of internal donor-acceptor heterojunctions, Science (80-.). 270 (1995) 1789–1790. http://lib.semi.ac.cn:8080/tsh/dzzy/wsqk/science/vol270/270-1789.pdf.

[15] H. Wang, H.-Y. Wang, B.-R. Gao, L. Wang, Z.-Y. Yang, X.-B. Du, Q.-D. Chen, J.-F. Song, H.-B. Sun, Exciton diffusion and charge transfer dynamics in nano phase-separated P3HT/PCBM blend films, Nanoscale. 3 (2011) 2280–2285. doi:10.1039/c0nr01002b.

[16] Y. Yao, J. Hou, Z. Xu, G. Li, Y. Yang, Effects of solvent mixtures on the nanoscale phase separation in polymer solar cells, Adv. Funct. Mater. 18 (2008) 1783–1789. doi:10.1002/adfm.200701459.

[17] C.-W. Chu, H. Yang, W.-J. Hou, J. Huang, G. Li, Y. Yang, Control of the nanoscale crystallinity and phase separation in polymer solar cells, Appl. Phys. Lett. 92 (2008) 103306. doi:10.1063/1.2891884.

[18] G. Janssen, A. Aguirre, E. Goovaerts, P. Vanlaeke, J. Poortmans, J. Manca, Optimization of morphology of P3HT/PCBM films for organic solar cells: effects of thermal treatments and spin coating solvents, Eur. Phys. J. Appl. Phys. 37 (2007) 287–290. doi:10.1051/epjap:2007002.

[19] J. Nelson, Organic photovoltaic films, Mater. Today. 5 (2002) 20–27.

http://www.sciencedirect.com/science/article/pii/S1359028602000062.

[20] C. Deibe, T. Strobe, V. Dyakonov, Role of the charge transfer state in organic donor-acceptor solar cells, Adv. Mater. 22 (2010) 4097–4111. doi:10.1002/adma.201000376.

[21] M.C. Scharber, D. Mühlbacher, M. Koppe, P. Denk, C. Waldauf, A.J. Heeger, C.J. Brabec, Design Rules for Donors in Bulk-Heterojunction Solar Cells—Towards 10 % Energy-Conversion Efficiency, Adv. Mater. 18 (2006) 789–794. doi:10.1002/adma.200501717.

[22] M. Knupfer, Exciton binding energies in organic semiconductors, Appl. Phys. A. 77 (2003) 623–626. doi:10.1007/s00339-003-2182-9.

[23] M. Wang, F. Xie, J. Du, Q. Tang, S. Zheng, Q. Miao, J. Chen, N. Zhao, J.B. Xu, Degradation mechanism of organic solar cells with aluminum cathode, Sol. Energy Mater. Sol. Cells. 95 (2011) 3303–3310. doi:10.1016/j.solmat.2011.07.020.

[24] M. Lira-Cantu, D.M. Tanenbaum, K. Norrman, E. Voroshazi, M. Hermenau, M.T. Lloyd, G. Teran-Escobar, Y. Galagan, B. Zimmermann, M. Hösel, H.F. Dam, M. Jørgensen, S. Gevorgyan, L. Lutsen, D. Vanderzande, H. Hoppe, R. Rösch, U. Würfel, R. Andriessen, A. Rivaton, G.Y. Uzunoğlu, D. Germack, B. Andreasen, M. V. Madsen, E. Bundgaard, F.C. Krebs, Combined characterization techniques to understand the stability of a variety of organic photovoltaic devices: the ISOS-3 inter-laboratory collaboration, in: N.G. Dhere, J.H. Wohlgemuth (Eds.), 2012: p. 847203. doi:10.1117/12.929579.

[25] V.M. Drakonakis, A. Savva, M. Kokonou, S.A. Choulis, Investigating electrodes degradation in organic photovoltaics through reverse engineering under accelerated humidity lifetime conditions, Sol. Energy Mater. Sol. Cells. 130 (2014) 544–550. doi:10.1016/j.solmat.2014.07.051.

[26] L.-M. Chen, Z. Hong, G. Li, Y. Yang, Recent Progress in Polymer Solar Cells: Manipulation of Polymer:Fullerene Morphology and the Formation of Efficient Inverted Polymer Solar Cells, Adv. Mater. 21 (2009) 1434–1449. doi:10.1002/adma.200802854.

[27] G. Wantz, L. Derue, O. Dautel, A. Rivaton, P. Hudhomme, C. Dagron-Lartigau, Stabilizing polymer-based bulk heterojunction solar cells via crosslinking, Polym. Int. 63 (2014) 1346–1361. doi:10.1002/pi.4712.

[28] J.W. Rumer, I. McCulloch, Organic photovoltaics: Crosslinking for optimal morphology and stability, Mater. Today. 18 (2015) 425–435. doi:10.1016/j.mattod.2015.04.001.

[29] S.A. Gevorgyan, I.M. Heckler, E. Bundgaard, M. Corazza, M. Hösel, R.R. Søndergaard, G.A. dos Reis Benatto, M. Jørgensen, F.C. Krebs, Improving, characterizing and predicting the lifetime of organic photovoltaics, J. Phys. D. Appl. Phys. 50 (2017) 103001. doi:10.1088/1361-6463/50/10/103001.

[30] M.O. Reese, S.A. Gevorgyan, M. Jørgensen, E. Bundgaard, S.R. Kurtz, D.S. Ginley, D.C. Olson, M.T. Lloyd, P. Morvillo, E.A. Katz, A. Elschner, O. Haillant, T.R. Currier, V. Shrotriya, M. Hermenau, M. Riede, K. R. Kirov, G. Trimmel, T. Rath, O. Inganäs, F. Zhang, M. Andersson, K. Tvingstedt, M. Lira-Cantu, D. Laird, C. McGuiness, S. (Jimmy) Gowrisanker, M. Pannone, M. Xiao, J. Hauch, R. Steim, D.M. DeLongchamp, R. Rösch, H. Hoppe, N. Espinosa, A. Urbina, G. Yaman-Uzunoglu, J.-B. Bonekamp, A.J.J.M. van Breemen, C. Girotto, E. Voroshazi, F.C. Krebs, Consensus stability testing protocols for organic photovoltaic materials and devices, Sol. Energy Mater. Sol. Cells. 95 (2011) 1253–1267. doi:10.1016/j.solmat.2011.01.036.

[31] M. Corazza, F.C. Krebs, S.A. Gevorgyan, Predicting, categorizing and intercomparing the lifetime of OPVs for different ageing tests, Sol. Energy Mater. Sol. Cells. 130 (2014) 99–106. doi:10.1016/j.solmat.2014.06.031.

[32] S.A. Gevorgyan, M. V. Madsen, B. Roth, M. Corazza, M. Hösel, R.R. Søndergaard, M. Jørgensen, F.C. Krebs, Lifetime of Organic Photovoltaics: Status and Predictions, Adv. Energy Mater. 6 (2016) 1501208. doi:10.1002/aenm.201501208.

[33] S.A. Gevorgyan, N. Espinosa, L. Ciammaruchi, B. Roth, F. Livi, S. Tsopanidis, S. Züfle, S. Queirós, A. Gregori, G.A. dos R. Benatto, M. Corazza, M. V. Madsen, M. Hösel, M.J. Beliatis, T.T. Larsen-Olsen, F. Pastorelli, A. Castro, A.

Mingorance, V. Lenzi, D. Fluhr, R. Roesch, M. Maria Duarte Ramos, A. Savva, H. Hoppe, L.S.A. Marques, I. Burgués, E. Georgiou, L. Serrano-Luján, F.C. Krebs, Baselines for Lifetime of Organic Solar Cells, (2016). doi:10.1002/aenm.201600910.

[34] C.J.M. Emmott, A. Urbina, J. Nelson, Environmental and economic assessment of ITO-free electrodes for organic solar cells, Sol. Energy Mater. Sol. Cells. 97 (2012) 14–21. doi:10.1016/j.solmat.2011.09.024.

[35] W.-H. Baek, M. Choi, T.-S. Yoon, H.H. Lee, Y.-S. Kim, Use of fluorine-doped tin oxide instead of indium tin oxide in highly efficient air-fabricated inverted polymer solar cells, Appl. Phys. Lett. 96 (2010) 133506. doi:10.1063/1.3374406.

[36] D. Chen, C. Zhang, Z. Wang, J. Zhang, S. Tang, W. Wei, L. Sun, Y. Hao, Efficient indium-tin-oxide free inverted organic solar cells based on aluminum-doped zinc oxide cathode and low-temperature aqueous solution processed zinc oxide electron extraction layer, Appl. Phys. Lett. 104 (2014) 243301. doi:10.1063/1.4884059.

[37] A.T. Barrows, R. Masters, A.J. Pearson, C. Rodenburg, D.G. Lidzey, Indium-free multilayer semi-transparent electrodes for polymer solar cells, Sol. Energy Mater. Sol. Cells. 144 (2016) 600–607. doi:10.1016/j.solmat.2015.10.010.

[38] H.K. Park, J.W. Kang, S.I. Na, D.Y. Kim, H.K. Kim, Characteristics of indium-free GZO/Ag/GZO and AZO/Ag/AZO multilayer electrode grown by dual target DC sputtering at room temperature for low-cost organic photovoltaics, Sol. Energy Mater. Sol. Cells. 93 (2009) 1994–2002. doi:10.1016/j.solmat.2009.07.016.

[39] C.-H. Chu, H.-W. Wu, J.-L. Huang, AZO/Au/AZO tri-layer thin films for the very low resistivity transparent electrode applications, Mater. Sci. Eng. B. 186 (2014) 117–121. doi:10.1016/j.mseb.2014.03.016.

[40] Y.J. Noh, S.S. Kim, T.W. Kim, S.I. Na, Cost-effective ITO-free organic solar cells with silver nanowire-PEDOT:PSS composite electrodes via a one-step spray deposition method, Sol. Energy Mater. Sol. Cells. 120 (2014) 226–230. doi:10.1016/j.solmat.2013.09.007.

[41] D. Alemu, H.-Y. Wei, K.-C. Ho, C.-W. Chu, Highly conductive PEDOT:PSS

electrode by simple film treatment with methanol for ITO-free polymer solar cells, Energy Environ. Sci. 5 (2012) 9662. doi:10.1039/c2ee22595f.

[42] P. Maisch, K.C. Tam, L. Lucera, H.J. Egelhaaf, H. Scheiber, E. Maier, C.J. Brabec, Inkjet printed silver nanowire percolation networks as electrodes for highly efficient semitransparent organic solar cells, Org. Electron. Physics, Mater. Appl. 38 (2016) 139–143. doi:10.1016/j.orgel.2016.08.006.

[43] L. Tan, H. Zhou, T. Ji, L. Huang, Y. Chen, High conductive PEDOT via post-treatment by halobenzoic for high-efficiency ITO-free and transporting layer-free organic solar cells, Org. Electron. Physics, Mater. Appl. 33 (2016) 316–323. doi:10.1016/j.orgel.2016.03.037.

[44] D.S. Hecht, L. Hu, G. Irvin, Emerging Transparent Electrodes Based on Thin Films of Carbon Nanotubes, Graphene, and Metallic Nanostructures, Adv. Mater. 23 (2011) 1482–1513. doi:10.1002/adma.201003188.

[45] E. Arici, S. Karazhanov, Carbon nanotubes for organic/inorganic hybrid solar cells, Mater. Sci. Semicond. Process. 41 (2016) 137–149. doi:10.1016/j.mssp.2015.07.086.

[46] M. Neophytou, E. Georgiou, M.M. Fyrillas, S.A. Choulis, Two step sintering process and metal grid design optimization for highly efficient ITO free organic photovoltaics, Sol. Energy Mater. Sol. Cells. 122 (2014) 1–7. doi:10.1016/j.solmat.2013.11.021.

[47] M. Xie, H. Lu, L. Zhang, J. Wang, Q. Luo, J. Lin, L. Ba, H. Liu, W. Shen, L. Shi, C.-Q. Ma, Fully Solution-Processed Semi-Transparent Perovskite Solar Cells With Ink-Jet Printed Silver Nanowires Top Electrode, Sol. RRL. 2 (2018) 1700184. doi:10.1002/solr.201700184.

[48] M. Song, D.S. You, K. Lim, S. Park, S. Jung, C.S. Kim, D.-H. Kim, D.-G. Kim, J.-K. Kim, J. Park, Y.-C. Kang, J. Heo, S.-H. Jin, J.H. Park, J.-W. Kang, Highly Efficient and Bendable Organic Solar Cells with Solution-Processed Silver Nanowire Electrodes, Adv. Funct. Mater. 23 (2013) 4177–4184. doi:10.1002/adfm.201202646.

[49] D.-S. Leem, A. Edwards, M.A. Faist, J. Nelson, D.D.C. Bradley, J.C. de Mello, Efficient Organic Solar Cells with Solution-Processed Silver Nanowire Electrodes, Adv. Mater. 23 (2011) 4371–4375. doi:10.1002/adma.201100871.

[50] F. Guo, P. Kubis, T. Stubhan, N. Li, D. Baran, T. Przybilla, E. Spiecker, K. Forberich, C.J. Brabec, Fully Solution-Processing Route toward Highly Transparent Polymer Solar Cells, ACS Appl. Mater. Interfaces. 6 (2014) 18251–18257. doi:10.1021/am505347p.

[51] Y.H. Kim, C. Sachse, A.A. Zakhidov, J. Meiss, A.A. Zakhidov, L. Müller-Meskamp, K. Leo, Combined alternative electrodes for semi-transparent and ITO-free small molecule organic solar cells, Org. Electron. 13 (2012) 2422–2428. doi:10.1016/j.orgel.2012.06.034.

[52] S. Chen, Q. Cui, X. Guo, Annealing-Free Solution-Processed Silver Nanowire-Polymer Composite Transparent Electrodes and Flexible Device Applications, IEEE Trans. Nanotechnol. 14 (2015) 36–41. doi:10.1109/TNANO.2014.2362536.

[53] V. Nam, D. Lee, Copper Nanowires and Their Applications for Flexible, Transparent Conducting Films: A Review, Nanomaterials. 6 (2016) 47. doi:10.3390/nano6030047.

[54] F. Bonaccorso, Z. Sun, T. Hasan, A.C. Ferrari, Graphene photonics and optoelectronics, Nat. Photonics. 4 (2010) 611–622. doi:10.1038/nphoton.2010.186.

[55] K.S. Kim, Y. Zhao, H. Jang, S.Y. Lee, J.M. Kim, K.S. Kim, J.-H. Ahn, P. Kim, J.-Y. Choi, B.H. Hong, Large-scale pattern growth of graphene films for stretchable transparent electrodes, Nature. 457 (2009) 706–710. doi:10.1038/nature07719.

[56] M. Layani, A. Kamyshny, S. Magdassi, Transparent conductors composed of nanomaterials, Nanoscale. 6 (2014) 5581–5591. doi:10.1039/C4NR00102H.

[57] F. Bonaccorso, Z. Sun, T. Hasan, A.C. Ferrari, Graphene photonics and optoelectronics, Nat. Photon. 4 (2010) 611–622. doi:10.1038/nphoton.2010.186.

[58] T. Dürkop, S.A. Getty, E. Cobas, M.S. Fuhrer, Extraordinary Mobility in

Semiconducting Carbon Nanotubes, Nano Lett. 4 (2004) 35–39. doi:10.1021/nl034841q.

[59] M.W. Rowell, M.A. Topinka, M.D. McGehee, H.J. Prall, G. Dennler, N.S. Sariciftci, L. Hu, G. Gruner, Organic solar cells with carbon nanotube network electrodes, Appl. Phys. Lett. 88 (2006) 86–89. doi:10.1063/1.2209887.

[60] D.-Y. Cho, K. Eun, S.-H. Choa, H.-K. Kim, Highly flexible and stretchable carbon nanotube network electrodes prepared by simple brush painting for cost-effective flexible organic solar cells, Carbon N. Y. 66 (2014) 530–538. doi:10.1016/j.carbon.2013.09.035.

[61] R. V Salvatierra, C.E. Cava, L.S. Roman, A.J.G. Zarbin, ITO-Free and Flexible Organic Photovoltaic Device Based on High Transparent and Conductive Polyaniline/Carbon Nanotube Thin Films, Adv. Funct. Mater. 23 (2012) 1490–1499. doi:10.1002/adfm.201201878.

[62] X. Zhang, J. Wu, J. Wang, J. Zhang, Q. Yang, Y. Fu, Z. Xie, Highly conductive PEDOT:PSS transparent electrode prepared by a post-spin-rinsing method for efficient ITO-free polymer solar cells, Sol. Energy Mater. Sol. Cells. 144 (2016) 143–149. doi:10.1016/j.solmat.2015.08.039.

[63] Y. Xia, K. Sun, J. Ouyang, Solution-Processed Metallic Conducting Polymer Films as Transparent Electrode of Optoelectronic Devices, Adv. Mater. 24 (2012) 2436–2440. doi:10.1002/adma.201104795.

[64] M. Kaltenbrunner, M.S. White, E.D. Głowacki, T. Sekitani, T. Someya, N.S. Sariciftci, S. Bauer, Ultrathin and lightweight organic solar cells with high flexibility, Nat. Commun. 3 (2012) 770. doi:10.1038/ncomms1772.

[65] S.-I. Na, S.-S. Kim, J. Jo, D.-Y. Kim, Efficient and Flexible ITO-Free Organic Solar Cells Using Highly Conductive Polymer Anodes, Adv. Mater. 20 (2008) 4061–4067. doi:10.1002/adma.200800338.

[66] N. Kim, S. Kee, S.H. Lee, B.H. Lee, Y.H. Kahng, Y.-R. Jo, B.-J. Kim, K. Lee, Highly Conductive PEDOT:PSS Nanofibrils Induced by Solution-Processed Crystallization, Adv. Mater. 26 (2014) 2268–2272. doi:10.1002/adma.201304611.

[67] G.A. dos Reis Benatto, B. Roth, M. Corazza, R.R. Søndergaard, S.A. Gevorgyan, M. Jørgensen, F.C. Krebs, Roll-to-roll printed silver nanowires for increased stability of flexible ITO-free organic solar cell modules, Nanoscale. 8 (2016) 318–326. doi:10.1039/C5NR07426F.

[68] E. VITORATOS, S. SAKKOPOULOS, E. DALAS, N. PALIATSAS, D. KARAGEORGOPOULOS, F. PETRAKI, S. KENNOU, S. CHOULIS, Thermal degradation mechanisms of PEDOT:PSS, Org. Electron. 10 (2009) 61–66. doi:10.1016/j.orgel.2008.10.008.

[69] T. Aernouts, P. Vanlaeke, W. Geens, J. Poortmans, P. Heremans, S. Borghs, R. Mertens, R. Andriessen, L. Leenders, Printable anodes for flexible organic solar cell modules, Thin Solid Films. 451–452 (2004) 22–25. doi:10.1016/j.tsf.2003.11.038.

[70] M. Glatthaar, M. Niggemann, B. Zimmermann, P. Lewer, M. Riede, A. Hinsch, J. Luther, Organic solar cells using inverted layer sequence, Thin Solid Films. 491 (2005) 298–300. doi:10.1016/j.tsf.2005.06.006.

[71] M.-G. Kang, M.-S. Kim, J. Kim, L.J. Guo, Organic Solar Cells Using Nanoimprinted Transparent Metal Electrodes, Adv. Mater. 20 (2008) 4408–4413. doi:10.1002/adma.200800750.

[72] Y. Galagan, J.-E.J.M. Rubingh, R. Andriessen, C.-C. Fan, P.W.M. Blom, S.C. Veenstra, J.M. Kroon, J.-E.J.M. Rubingh, P.W.M. Blom, ITO-free flexible organic solar cells with printed current collecting grids, Sol. Energy Mater. Sol. Cells. 95 (2011) 1339–1343. doi:10.1016/j.solmat.2010.08.011.

[73] D. Angmo, S.A. Gevorgyan, T.T. Larsen-Olsen, R.R. Søndergaard, M. Hösel, M. Jørgensen, R. Gupta, G.U. Kulkarni, F.C. Krebs, Scalability and stability of very thin, roll-to-roll processed, large area, indium-tin-oxide free polymer solar cell modules, Org. Electron. 14 (2013) 984–994. doi:10.1016/j.orgel.2012.12.033.

[74] D. Li, W.-Y. Lai, Y.-Z. Zhang, W. Huang, Printable Transparent Conductive Films for Flexible Electronics, Adv. Mater. 30 (2018) 1704738. doi:10.1002/adma.201704738.

[75] J. Perelaer, R. Abbel, S. Wünscher, R. Jani, T. van Lammeren, U.S. Schubert, Roll-to-Roll Compatible Sintering of Inkjet Printed Features by Photonic and Microwave Exposure: From Non-Conductive Ink to 40% Bulk Silver Conductivity in Less Than 15 Seconds, Adv. Mater. 24 (2012) 2620–2625. doi:10.1002/adma.201104417.

[76] J. Perelaer, M. Klokkenburg, C.E. Hendriks, U.S. Schubert, Microwave Flash Sintering of Inkjet-Printed Silver Tracks on Polymer Substrates, Adv. Mater. 21 (2009) 4830–4834. doi:10.1002/adma.200901081.

[77] P. Peng, A. Hu, Y. Zhou, Laser sintering of silver nanoparticle thin films: microstructure and optical properties, Appl. Phys. A. 108 (2012) 685–691. doi:10.1007/s00339-012-6951-1.

[78] M. Zenou, O. Ermak, A. Saar, Z. Kotler, Laser sintering of copper nanoparticles, J. Phys. D. 47 (2013) 25501. doi:10.1088/0022-3727/47/2/025501.

[79] M. Neophytou, E. Georgiou, M.M. Fyrillas, S.A. Choulis, Two step sintering process and metal grid design optimization for highly efficient ITO free organic photovoltaics, Sol. Energy Mater. Sol. Cells. 122 (2014) 1–7. doi:10.1016/j.solmat.2013.11.021.

[80] Y. Galagan, B. Zimmermann, E.W.C. Coenen, M. Jørgensen, D.M. Tanenbaum, F.C. Krebs, H.H. Gorter, S. Sabik, L.H. Slooff, S.C. Veenstra, J.M. Kroon, R. Andriessen, Current Collecting Grids for ITO-Free Solar Cells, Adv. Energy Mater. 2 (2012) 103–110. doi:10.1002/aenm.201100552.

[81] E. Georgiou, A. Savva, M. Neophytou, F. Hermerschmidt, T. Demosthenous, S.A. Choulis, Evaporation-free inverted organic photovoltaics using a mixture of silver nanoparticle ink formulations for solution-processed top electrodes, Appl. Phys. Lett. 105 (2014) 233901. doi:10.1063/1.4903893.

[82] S. Jung, A. Sou, K. Banger, D.-H. Ko, P.C.Y. Chow, C.R. McNeill, H. Sirringhaus, All-Inkjet-Printed, All-Air-Processed Solar Cells, Adv. Energy Mater. 4 (2014) n/a-n/a. doi:10.1002/aenm.201400432.

[83] Y. Galagan, S. Shanmugam, J.P. Teunissen, T.M. Eggenhuisen, A.F.K. V

Biezemans, T. Van Gijseghem, W.A. Groen, R. Andriessen, Solution processing of back electrodes for organic solar cells with inverted architecture, Sol. Energy Mater. Sol. Cells. 130 (2014) 163–169. doi:10.1016/j.solmat.2014.07.007.

[84] T.M. Eggenhuisen, Y. Galagan, A.F.K. V. Biezemans, T.M.W.L. Slaats, W.P. Voorthuijzen, S. Kommeren, S. Shanmugam, J.P. Teunissen, A. Hadipour, W.J.H. Verhees, S.C. Veenstra, M.J.J. Coenen, J. Gilot, R. Andriessen, W.A. Groen, High efficiency, fully inkjet printed organic solar cells with freedom of design, J. Mater. Chem. A. 3 (2015) 7255–7262. doi:10.1039/C5TA00540J.

[85] F.C. Krebs, R. Søndergaard, M. Jørgensen, Printed metal back electrodes for R2R fabricated polymer solar cells studied using the LBIC technique, Sol. Energy Mater. Sol. Cells. 95 (2011) 1348–1353. doi:10.1016/j.solmat.2010.11.007.

[86] Y. Galagan, E.W.C. Coenen, S. Sabik, H.H. Gorter, M. Barink, S.C. Veenstra, J.M. Kroon, R. Andriessen, P.W.M. Blom, Evaluation of ink-jet printed current collecting grids and busbars for ITO-free organic solar cells, Sol. Energy Mater. Sol. Cells. 104 (2012) 32–38. doi:10.1016/j.solmat.2012.04.039.

[87] I. Burgués-Ceballos, N. Kehagias, C.M. Sotomayor-Torres, M. Campoy-Quiles, P.D. Lacharmoise, Embedded inkjet printed silver grids for ITO-free organic solar cells with high fill factor, Sol. Energy Mater. Sol. Cells. 127 (2014) 50–57. doi:10.1016/j.solmat.2014.03.024.

[88] M. Neophytou, F. Hermerschmidt, A. Savva, E. Georgiou, S.A. Choulis, Highly efficient indium tin oxide-free organic photovoltaics using inkjet-printed silver nanoparticle current collecting grids, Appl. Phys. Lett. 101 (2012) 193302. doi:10.1063/1.4765343.

[89] L. Lu, T. Zheng, Q. Wu, A.M. Schneider, D. Zhao, L. Yu, Recent Advances in Bulk Heterojunction Polymer Solar Cells, Chem. Rev. 115 (2015) 12666–12731. doi:10.1021/acs.chemrev.5b00098.

[90] W. Zhao, D. Qian, S. Zhang, S. Li, O. Inganäs, F. Gao, J. Hou, Fullerene-Free Polymer Solar Cells with over 11% Efficiency and Excellent Thermal Stability, Adv. Mater. (2016) 4734–4739. doi:10.1002/adma.201600281.

[91] N. Gasparini, M. Salvador, S. Strohm, T. Heumueller, I. Levchuk, A. Wadsworth, J.H. Bannock, J.C. de Mello, H.-J. Egelhaaf, D. Baran, I. McCulloch, C.J. Brabec, Burn-in Free Nonfullerene-Based Organic Solar Cells, Adv. Energy Mater. 7 (2017) 1700770. doi:10.1002/aenm.201700770.

[92] W. Zhao, S. Zhang, J. Hou, Realizing 11.3% efficiency in fullerene-free polymer solar cells by device optimization, Sci. China Chem. 59 (2016) 1574–1582. doi:10.1007/s11426-016-0198-0.

[93] H. Lu, J. Zhang, J. Chen, Q. Liu, X. Gong, S. Feng, X. Xu, W. Ma, Z. Bo, Ternary-Blend Polymer Solar Cells Combining Fullerene and Nonfullerene Acceptors to Synergistically Boost the Photovoltaic Performance, Adv. Mater. 28 (2016) 9559–9566. doi:10.1002/adma.201603588.

[94] R. Steim, F.R. Kogler, C.J. Brabec, Interface materials for organic solar cells, J. Mater. Chem. 20 (2010) 2499. doi:10.1039/b921624c.

[95] E. Voroshazi, B. Verreet, A. Buri, R. Muller, D. Di Nuzzo, P. Heremans, Influence of cathode oxidation via the hole extraction layer in polymer:fullerene solar cells, Org. Electron. 12 (2011) 736–744. doi:10.1016/j.orgel.2011.01.025.

[96] C.W.T. Bulle-Lieuwma, W.J.H. van Gennip, J.K.J. van Duren, P. Jonkheijm, R.A.J. Janssen, J.W. Niemantsverdriet, Characterization of polymer solar cells by TOF-SIMS depth profiling, Appl. Surf. Sci. 203–204 (2003) 547–550. doi:10.1016/S0169-4332(02)00756-0.

[97] M.P. de Jong, L.J. van IJzendoorn, M.J.A. de Voigt, Stability of the interface between indium-tin-oxide and poly(3,4-ethylenedioxythiophene)/poly(styrenesulfonate) in polymer light-emitting diodes, Appl. Phys. Lett. 77 (2000) 2255–2257. doi:10.1063/1.1315344.

[98] T. Stubhan, I. Litzov, N. Li, M. Salinas, M. Steidl, G. Sauer, K. Forberich, G.J. Matt, M. Halik, C.J. Brabec, Overcoming interface losses in organic solar cells by applying low temperature, solution processed aluminum-doped zinc oxide electron extraction layers, J. Mater. Chem. A. 1 (2013) 6004. doi:10.1039/c3ta10987a.

[99] T. Stubhan, H. Oh, L. Pinna, J. Krantz, I. Litzov, C.J. Brabec, Inverted organic

solar cells using a solution processed aluminum-doped zinc oxide buffer layer, Org. Electron. 12 (2011) 1539–1543. doi:10.1016/j.orgel.2011.05.027.

[100] A. Savva, S.A. Choulis, Cesium-doped zinc oxide as electron selective contact in inverted organic photovoltaics, Appl. Phys. Lett. 102 (2013). doi:10.1063/1.4811088.

[101] L.J.A. Koster, V.D. Mihailetchi, P.W.M. Blom, Ultimate efficiency of polymer/fullerene bulk heterojunction solar cells, Appl. Phys. Lett. 88 (2006) 93511. http://link.aip.org/link/?APL/88/093511/1.

[102] M. Lenes, L.J.A. Koster, V.D. Mihailetchi, P.W.M. Blom, Thickness dependence of the efficiency of polymer:fullerene bulk heterojunction solar cells, Appl. Phys. Lett. 88 (2006) 243502. doi:10.1063/1.2211189.

[103] G. Dennler, M.C. Scharber, C.J. Brabec, Polymer-Fullerene Bulk-Heterojunction Solar Cells, Adv. Mater. 21 (2009) 1323–1338. doi:10.1002/adma.200801283.

[104] D. Angmo, T.T. Larsen-olsen, F.C. Krebs, Roll-to-roll fabrication of polymer solar cells As the performance in terms of power conversion efficiency and operational, Mater. Today. 15 (2012) 36–49. doi:10.1016/S1369-7021(12)70019-6.

[105] F.C. Krebs, Fabrication and processing of polymer solar cells: a review of printing and coating techniques, Sol. Energy Mater. Sol. Cells. 93 (2009) 394–412. http://dx.doi.org/10.1016/j.solmat.2008.10.004.

[106] M. Manceau, D. Angmo, M. Jørgensen, F.C. Krebs, ITO-free flexible polymer solar cells: From small model devices to roll-to-roll processed large modules, Org. Electron. 12 (2011) 566–574. doi:10.1016/j.orgel.2011.01.009.

[107] D. Jang, D. Kim, J. Moon, Influence of fluid physical properties on ink-jet printability., Langmuir. 25 (2009) 2629–35. doi:10.1021/la900059m.

[108] A. Lange, W. Schindler, M. Wegener, K. Fostiropoulos, S. Janietz, Inkjet printed solar cell active layers prepared from chlorine-free solvent systems, Sol. Energy Mater. Sol. Cells. 109 (2013) 104–110. doi:10.1016/j.solmat.2012.10.011.

[109] C.N. Hoth, S.A. Choulis, P. Schilinsky, C.J. Brabec, High Photovoltaic

Performance of Inkjet Printed Polymer:Fullerene Blends, Adv. Mater. 19 (2007) 3973–3978. doi:10.1002/adma.200700911.

[110] Y. Jang, J. Jo, D.-S. Kim, Control of doctor-blade coated poly (3,4-ethylenedioxythiophene)/poly(styrenesulfonate) electrodes shape on prepatterned substrates via microflow control in a drying droplet, J. Polym. Sci. B. 49 (2011) 1590–1596. doi:10.1002/polb.22347.

[111] M. Neophytou, W. Cambarau, F. Hermerschmidt, C. Waldauf, C. Christodoulou, R. Pacios, S.A. Choulis, Inkjet-printed polymer–fullerene blends for organic electronic applications, Microelectron. Eng. 95 (2012) 102–106. doi:10.1016/j.mee.2012.02.005.

[112] H. Hu, R.G. Larson, Marangoni Effect Reverses Coffee-Ring Depositions, J. Phys. Chem. B. 110 (2006) 7090–7094. doi:10.1021/jp0609232.

[113] C.J. Mulligan, C. Bilen, X. Zhou, W.J. Belcher, P.C. Dastoor, Levelised cost of electricity for organic photovoltaics, Sol. Energy Mater. Sol. Cells. 133 (2015) 26–31. doi:10.1016/j.solmat.2014.10.043.

[114] S.A. Gevorgyan, N. Espinosa, L. Ciammaruchi, B. Roth, F. Livi, S. Tsopanidis, S. Züfle, S. Queirós, A. Gregori, G.A. dos R. Benatto, M. Corazza, M. V. Madsen, M. Hösel, M.J. Beliatis, T.T. Larsen-Olsen, F. Pastorelli, A. Castro, A. Mingorance, V. Lenzi, D. Fluhr, R. Roesch, M. Maria Duarte Ramos, A. Savva, H. Hoppe, L.S.A. Marques, I. Burgués, E. Georgiou, L. Serrano-Luján, F.C. Krebs, Baselines for Lifetime of Organic Solar Cells, Adv. Energy Mater. 6 (2016) 1600910. doi:10.1002/aenm.201600910.

[115] P. Kopola, T. Aernouts, R. Sliz, S. Guillerez, M. Ylikunnari, D. Cheyns, M. Välimäki, M. Tuomikoski, J. Hast, G. Jabbour, R. Myllylä, A. Maaninen, Gravure printed flexible organic photovoltaic modules, Sol. Energy Mater. Sol. Cells. 95 (2011) 1344–1347. doi:10.1016/j.solmat.2010.12.020.

[116] M. Hösel, R.R. Søndergaard, D. Angmo, F.C. Krebs, Comparison of Fast Roll-to-Roll Flexographic, Inkjet, Flatbed, and Rotary Screen Printing of Metal Back Electrodes for Polymer Solar Cells, Adv. Eng. Mater. 15 (2013) 995–1001. doi:10.1002/adem.201300011.

[117] B. Zimmermann, H.F. Schleiermacher, M. Niggemann, U. Würfel, ITO-free flexible inverted organic solar cell modules with high fill factor prepared by slot die coating, Sol. Energy Mater. Sol. Cells. 95 (2011) 1587–1589. doi:10.1016/j.solmat.2010.11.025.

[118] T.M. Eggenhuisen, Y. Galagan, A.F.K. V. Biezemans, T.M.W.L. Slaats, W.P. Voorthuijzen, S. Kommeren, S. Shanmugam, J.P. Teunissen, A. Hadipour, W.J.H. Verhees, S.C. Veenstra, M.J.J. Coenen, J. Gilot, R. Andriessen, W.A. Groen, High efficiency, fully inkjet printed organic solar cells with freedom of design, J. Mater. Chem. A. 3 (2015) 7255–7262. doi:10.1039/C5TA00540J.

[119] F. Hermerschmidt, P. Papagiorgis, A. Savva, C. Christodoulou, G. Itskos, S.A. Choulis, Inkjet printing processing conditions for bulk-heterojunction solar cells using two high-performing conjugated polymer donors, Sol. Energy Mater. Sol. Cells. 130 (2014) 474–480. doi:10.1016/j.solmat.2014.07.050.

[120] C.N. Hoth, P. Schilinsky, S.A. Choulis, C.J. Brabec, Printing Highly Efficient Organic Solar Cells, Nano Lett. 8 (2008) 2806–2813. doi:10.1021/nl801365k.

[121] A. Andersson, N. Johansson, P. Bröms, N. Yu, D. Lupo, W.R. Salaneck, Fluorine Tin Oxide as an Alternative to Indium Tin Oxide in Polymer LEDs, Adv. Mater. 10 (1998) 859–863. doi:10.1002/(SICI)1521-4095(199808)10:11<859::AID-ADMA859>3.0.CO;2-1.

[122] A. Kumar, C. Zhou, The Race To Replace Tin-Doped Indium Oxide: Which Material Will Win?, ACS Nano. 4 (2010) 11–14. doi:10.1021/nn901903b.

[123] Y. Yu, X. Xiao, Y. Zhang, K. Li, C. Yan, X. Wei, L. Chen, H. Zhen, H. Zhou, S. Zhang, Z. Zheng, Photoreactive and Metal-Platable Copolymer Inks for High-Throughput, Room-Temperature Printing of Flexible Metal Electrodes for Thin-Film Electronics, Adv. Mater. 28 (2016) 4926–4934. doi:10.1002/adma.201505119.

[124] I. Burgués-Ceballos, N. Kehagias, C.M. Sotomayor-Torres, M. Campoy-Quiles, P.D. Lacharmoise, Embedded inkjet printed silver grids for ITO-free organic solar cells with high fill factor, Sol. Energy Mater. Sol. Cells. 127 (2014) 50–57. doi:10.1016/j.solmat.2014.03.024.

[125] Y. Galagan, E.W.C. Coenen, S. Sabik, H.H. Gorter, M. Barink, S.C. Veenstra, J.M. Kroon, R. Andriessen, P.W.M. Blom, E.W.C. Coenen, P.W.M. Blom, Evaluation of ink-jet printed current collecting grids and busbars for ITO-free organic solar cells, Sol. Energy Mater. Sol. Cells. 104 (2012) 32–38. doi:10.1016/j.solmat.2012.04.039.

[126] S.-I. Na, D.-W. Park, S.-S. Kim, S.-Y. Yang, K. Lee, M.-H. Lee, ITO-free flexible polymer solar cells with ink-jet-printed Ag grids, Semicond. Sci. Technol. 27 (2012) 125002. doi:10.1088/0268-1242/27/12/125002.

[127] M. Neophytou, F. Hermerschmidt, A. Savva, E. Georgiou, S.A. Choulis, Highly efficient indium tin oxide-free organic photovoltaics using inkjet-printed silver nanoparticle current collecting grids, Appl. Phys. Lett. 101 (2012). doi:10.1063/1.4765343.

[128] G. Polino, R. Abbel, S. Shanmugam, G.J.P. Bex, R. Hendriks, F. Brunetti, A. Di Carlo, R. Andriessen, Y. Galagan, A benchmark study of commercially available copper nanoparticle inks for application in organic electronic devices, Org. Electron. Physics, Mater. Appl. 34 (2016). doi:10.1016/j.orgel.2016.04.021.

[129] R. Dharmadasa, M. Jha, D.A. Amos, T. Druffel, Room Temperature Synthesis of a Copper Ink for the Intense Pulsed Light Sintering of Conductive Copper Films, ACS Appl. Mater. Interfaces. 5 (2013) 13227–13234. doi:10.1021/am404226e.

[130] Yang Wei, Yi Li, R. Torah, J. Tudor, Laser curing of screen and inkjet printed conductors on flexible substrates, in: 2015 Symp. Des. Test, Integr. Packag. MEMS/MOEMS, IEEE, 2015: pp. 1–4. doi:10.1109/DTIP.2015.7160991.

[131] J. Niittynen, E. Sowade, H. Kang, R.R. Baumann, M. Mäntysalo, Comparison of laser and intense pulsed light sintering (IPL) for inkjet-printed copper nanoparticle layers, Sci. Rep. 5 (2015) 8832. doi:10.1038/srep08832.

[132] K. Woo, Y. Kim, B. Lee, J. Kim, J. Moon, Effect of Carboxylic Acid on Sintering of Inkjet-Printed Copper Nanoparticulate Films, ACS Appl. Mater. Interfaces. 3 (2011) 2377–2382. doi:10.1021/am2002907.

[133] M. Neophytou, E. Georgiou, M.M. Fyrillas, S.A. Choulis, Two step sintering

process and metal grid design optimization for highly efficient ITO free organic photovoltaics, Sol. Energy Mater. Sol. Cells. 122 (2014) 1–7. doi:10.1016/j.solmat.2013.11.021.

[134] K. Tvingstedt, O. Inganäs, Electrode Grids for ITO Free Organic Photovoltaic Devices, Adv. Mater. 19 (2007) 2893–2897. doi:10.1002/adma.200602561.

[135] K.-W. Seo, Y.-J. Noh, S.-I. Na, H.-K. Kim, Random mesh-like Ag networks prepared via self-assembled Ag nanoparticles for ITO-free flexible organic solar cells, Sol. Energy Mater. Sol. Cells. 155 (2016) 51–59. doi:10.1016/j.solmat.2016.04.056.

[136] Y. Li, L. Meng, Y. (Michael) Yang, G. Xu, Z. Hong, Q. Chen, J. You, G. Li, Y. Yang, Y. Li, High-efficiency robust perovskite solar cells on ultrathin flexible substrates, Nat. Commun. 7 (2016) 10214. doi:10.1038/ncomms10214.

[137] F. Hermerschmidt, I. Burgués-Ceballos, A. Savva, E.D. Sepos, A. Lange, C. Boeffel, S. Nau, E.J.W. List-Kratochvil, S.A. Choulis, High performance indium tin oxide-free solution-processed organic light emitting diodes based on inkjet-printed fine silver grid lines, Flex. Print. Electron. 1 (2016) 35004. doi:10.1088/2058-8585/1/3/035004.

[138] L. Kinner, S. Nau, K. Popovic, S. Sax, I. Burgués-Ceballos, F. Hermerschmidt, A. Lange, C. Boeffel, S.A. Choulis, E.J.W. List-Kratochvil, Inkjet-printed embedded Ag-PEDOT:PSS electrodes with improved light out coupling effects for highly efficient ITO-free blue polymer light emitting diodes, Appl. Phys. Lett. 110 (2017) 101107. doi:10.1063/1.4978429.

[139] T. Stubhan, I. Litzov, N. Li, M. Salinas, M. Steidl, G. Sauer, K. Forberich, G.J. Matt, M. Halik, C.J. Brabec, Overcoming interface losses in organic solar cells by applying low temperature, solution processed aluminum-doped zinc oxide electron extraction layers, J. Mater. Chem. A. 1 (2013) 6004–6009. doi:10.1039/c3ta10987a.

[140] A. Savva, E. Georgiou, G. Papazoglou, A.Z. Chrusou, K. Kapnisis, S.A. Choulis, Photovoltaic analysis of the effects of PEDOT:PSS-additives hole selective contacts on the efficiency and lifetime performance of inverted organic solar cells,

Sol. Energy Mater. Sol. Cells. 132 (2015) 507–514. doi:10.1016/j.solmat.2014.10.004.

[141] C. Mayousse, C. Celle, A. Carella, J.-P. Simonato, Synthesis and purification of long copper nanowires. Application to high performance flexible transparent electrodes with and without PEDOT:PSS, Nano Res. 7 (2014) 315–324. doi:10.1007/s12274-013-0397-4.

[142] X.W. Ye Wan, H. Sun, Y. Li, K. Zhang, Y. Wu, Corrosion behavior of copper at elevated temperature, Int. J. Electrochem. Sci. 7 (2012) 7902–7914.

[143] S. Back, B. Kang, Low-cost optical fabrication of flexible copper electrode via laser-induced reductive sintering and adhesive transfer, Opt. Lasers Eng. 101 (2018) 78–84. doi:10.1016/j.optlaseng.2017.09.027.

[144] F.C. Krebs, Fabrication and processing of polymer solar cells: A review of printing and coating techniques, Sol. Energy Mater. Sol. Cells. 93 (2009) 394–412. doi:10.1016/j.solmat.2008.10.004.

[145] M.A. Green, Y. Hishikawa, W. Warta, E.D. Dunlop, D.H. Levi, J. Hohl-Ebinger, A.W.H. Ho-Baillie, Solar cell efficiency tables (version 50), Prog. Photovoltaics Res. Appl. 25 (2017) 668–676. doi:10.1002/pip.2909.

[146] R. Steim, S.A. Choulis, P. Schilinsky, C.J. Brabec, Interface modification for highly efficient organic photovoltaics, Appl. Phys. Lett. 92 (2008) 227–230. doi:10.1063/1.2885724.

[147] C. Waldauf, M. Morana, P. Denk, P. Schilinsky, K. Coakley, S.A. Choulis, C.J. Brabec, Highly efficient inverted organic photovoltaics using solution based titanium oxide as electron selective contact, Appl. Phys. Lett. 89 (2006) 233517. doi:10.1063/1.2402890.

[148] J. Adams, M. Salvador, L. Lucera, S. Langner, G.D. Spyropoulos, F.W. Fecher, M.M. Voigt, S.A. Dowland, A. Osvet, H.-J. Egelhaaf, C.J. Brabec, Water Ingress in Encapsulated Inverted Organic Solar Cells: Correlating Infrared Imaging and Photovoltaic Performance, Adv. Energy Mater. 5 (2015) 1501065. doi:10.1002/aenm.201501065.

[149] T.S. Glen, N.W. Scarratt, H. Yi, A. Iraqi, T. Wang, J. Kingsley, A.R. Buckley, D.G. Lidzey, A.M. Donald, Dependence on material choice of degradation of organic solar cells following exposure to humid air, J. Polym. Sci. Part B Polym. Phys. 54 (2016) 216–224. doi:10.1002/polb.23905.

[150] I.T. Sachs-Quintana, T. Heumüller, W.R. Mateker, D.E. Orozco, R. Cheacharoen, S. Sweetnam, C.J. Brabec, M.D. McGehee, Electron barrier formation at the organic-back contact interface is the first step in thermal degradation of polymer solar cells, Adv. Funct. Mater. 24 (2014) 3978–3985. doi:10.1002/adfm.201304166.

[151] K. Kawano, R. Pacios, D. Poplavskyy, J. Nelson, D.D.C. Bradley, J.R. Durrant, Degradation of organic solar cells due to air exposure, Sol. Energy Mater. Sol. Cells. 90 (2006) 3520–3530. doi:10.1016/j.solmat.2006.06.041.

[152] M.T. Lloyd, C.H. Peters, A. Garcia, I. V. Kauvar, J.J. Berry, M.O. Reese, M.D. McGehee, D.S. Ginley, D.C. Olson, Influence of the hole-transport layer on the initial behavior and lifetime of inverted organic photovoltaics, Sol. Energy Mater. Sol. Cells. 95 (2011) 1382–1388. doi:10.1016/j.solmat.2010.12.036.

[153] M.T. Lloyd, D.C. Olson, P. Lu, E. Fang, D.L. Moore, M.S. White, M.O. Reese, D.S. Ginley, J.W.P. Hsu, Impact of contact evolution on the shelf life of organic solar cells, J. Mater. Chem. 19 (2009) 7638. doi:10.1039/b910213b.

[154] A. Savva, E. Georgiou, G. Papazoglou, A.Z. Chrusou, K. Kapnisis, S.A. Choulis, Photovoltaic analysis of the effects of PEDOT:PSS-additives hole selective contacts on the efficiency and lifetime performance of inverted organic solar cells, Sol. Energy Mater. Sol. Cells. 132 (2015) 507–514. doi:10.1016/j.solmat.2014.10.004.

[155] K. Norrman, M. V Madsen, S.A. Gevorgyan, F.C. Krebs, Degradation patterns in water and oxygen of an inverted polymer solar cell., J. Am. Chem. Soc. 132 (2010) 16883–92. doi:10.1021/ja106299g.

[156] K. Zilberberg, H. Gharbi, A. Behrendt, S. Trost, T. Riedl, Low-Temperature, Solution-Processed MoOx for Efficient and Stable Organic Solar Cells, ACS Appl. Mater. Interfaces. 4 (2012) 1164–1168. doi:10.1021/am201825t.

[157] W. Qiu, R. Müller, E. Voroshazi, B. Conings, R. Carleer, H.-G. Boyen, M. Turbiez, L. Froyen, P. Heremans, A. Hadipour, Nafion-Modified MoO x as Effective Room-Temperature Hole Injection Layer for Stable, High-Performance Inverted Organic Solar Cells, ACS Appl. Mater. Interfaces. 7 (2015) 3581–3589. doi:10.1021/am507459t.

[158] J.-H. Kim, E.-K. Park, J.-H. Kim, H.J. Cho, D.-H. Lee, Y.-S. Kim, Improving charge transport of P3HT:PCBM organic solar cell using MoO3 nanoparticles as an interfacial buffer layer, Electron. Mater. Lett. 12 (2016) 383–387. doi:10.1007/s13391-016-5452-3.

[159] Y. Wang, Q. Luo, N. Wu, Q. Wang, H. Zhu, L. Chen, Y.-Q. Li, L. Luo, C.-Q. Ma, Solution-Processed MoO 3 :PEDOT:PSS Hybrid Hole Transporting Layer for Inverted Polymer Solar Cells, ACS Appl. Mater. Interfaces. 7 (2015) 7170–7179. doi:10.1021/am509049t.

[160] S.R. Hammond, J. Meyer, N.E. Widjonarko, P.F. Ndione, A.K. Sigdel, A. Garcia, A. Miedaner, M.T. Lloyd, A. Kahn, D.S. Ginley, J.J. Berry, D.C. Olson, Low-temperature, solution-processed molybdenum oxide hole-collection layer for organic photovoltaics, J. Mater. Chem. 22 (2012) 3249–3254. doi:10.1039/c2jm14911g.

[161] S. Park, J. Jeong, G. Hyun, M. Kim, H. Lee, Y. Yi, The origin of high PCE in PTB7 based photovoltaics: proper charge neutrality level and free energy of charge separation at PTB7/PC71BM interface, Sci. Rep. 6 (2016) 35262. doi:10.1038/srep35262.

[162] H.C. Weerasinghe, S.E. Watkins, N. Duffy, D.J. Jones, A.D. Scully, Influence of moisture out-gassing from encapsulant materials on the lifetime of organic solar cells, Sol. Energy Mater. Sol. Cells. 132 (2015) 485–491. doi:10.1016/j.solmat.2014.09.030.

[163] Irfan, H. Ding, Y. Gao, C. Small, D.Y. Kim, J. Subbiah, F. So, Energy level evolution of air and oxygen exposed molybdenum trioxide films, Appl. Phys. Lett. 96 (2010) 243307. doi:10.1063/1.3454779.

[164] J. Griffin, D.C. Watters, H. Yi, A. Iraqi, D. Lidzey, A.R. Buckley, The Influence

of MoO x Anode Stoicheometry on the Performance of Bulk Heterojunction Polymer Solar Cells, Adv. Energy Mater. 3 (2013) 903–908. doi:10.1002/aenm.201200886.

[165] E. Voroshazi, I. Cardinaletti, G. Uytterhoeven, S. Li, M. Empl, T. Aernouts, B.P. Rand, Role of Electron- and Hole-Collecting Buffer Layers on the Stability of Inverted Polymer: Fullerene Photovoltaic Devices, IEEE J. Photovoltaics. 4 (2014) 265–270. doi:10.1109/JPHOTOV.2013.2287913.

[166] Z. Zhang, Y. Xiao, H.-X. Wei, G.-F. Ma, S. Duhm, Y.-Q. Li, J.-X. Tang, Impact of Oxygen Vacancy on Energy-Level Alignment at MoO x /Organic Interfaces, Appl. Phys. Express. 6 (2013) 95701. doi:10.7567/APEX.6.095701.

[167] H. Zhang, A. Borgschulte, F.A. Castro, R. Crockett, A.C. Gerecke, O. Deniz, J. Heier, S. Jenatsch, F. Nüesch, C. Sanchez-Sanchez, A. Zoladek-Lemanczyk, R. Hany, Photochemical Transformations in Fullerene and Molybdenum Oxide Affect the Stability of Bilayer Organic Solar Cells, Adv. Energy Mater. 5 (2015) 1400734. doi:10.1002/aenm.201400734.

[168] E. Voroshazi, G. Uytterhoeven, K. Cnops, T. Conard, P. Favia, H. Bender, R. Muller, D. Cheyns, Root-Cause Failure Analysis of Photocurrent Loss in Polythiophene:Fullerene-Based Inverted Solar Cells, ACS Appl. Mater. Interfaces. 7 (2015) 618–623. doi:10.1021/am506771e.

[169] R. Rösch, D.M. Tanenbaum, M. Jørgensen, M. Seeland, M. Bärenklau, M. Hermenau, E. Voroshazi, M.T. Lloyd, Y. Galagan, B. Zimmermann, U. Würfel, M. Hösel, H.F. Dam, S.A. Gevorgyan, S. Kudret, W. Maes, L. Lutsen, D. Vanderzande, R. Andriessen, G. Teran-Escobar, M. Lira-Cantu, A. Rivaton, G.Y. Uzunoğlu, D. Germack, B. Andreasen, M. V. Madsen, K. Norrman, H. Hoppe, F.C. Krebs, Investigation of the degradation mechanisms of a variety of organic photovoltaic devices by combination of imaging techniques—the ISOS-3 inter-laboratory collaboration, Energy Environ. Sci. 5 (2012) 6521. doi:10.1039/c2ee03508a.

[170] W. Greenbank, N. Rolston, E. Destouesse, G. Wantz, L. Hirsch, R. Dauskardt, S. Chambon, Improved mechanical adhesion and electronic stability of organic solar

cells with thermal ageing: the role of diffusion at the hole extraction interface, J. Mater. Chem. A. 5 (2017) 2911–2919. doi:10.1039/C6TA09665D.

[171] A. Savva, S.A. Choulis, Cesium-doped zinc oxide as electron selective contact in inverted organic photovoltaics, Appl. Phys. Lett. 102 (2013) 233301. doi:10.1063/1.4811088.

[172] H.C. Wong, Z. Li, C.H. Tan, H. Zhong, Z. Huang, H. Bronstein, I. McCulloch, J.T. Cabral, J.R. Durrant, Morphological Stability and Performance of Polymer–Fullerene Solar Cells under Thermal Stress: The Impact of Photoinduced PC 60 BM Oligomerization, ACS Nano. 8 (2014) 1297–1308. doi:10.1021/nn404687s.

[173] L. Lu, L. Yu, Understanding Low Bandgap Polymer PTB7 and Optimizing Polymer Solar Cells Based on It, Adv. Mater. 26 (2014) 4413–4430. doi:10.1002/adma.201400384.

[174] A. Savva, M. Neophytou, C. Koutsides, K. Kalli, S.A. Choulis, Synergistic effects of buffer layer processing additives for enhanced hole carrier selectivity in inverted Organic Photovoltaics, Org. Electron. 14 (2013) 3123–3130. doi:10.1016/j.orgel.2013.07.024.

[175] M.O. Reese, S.A. Gevorgyan, M. Jørgensen, E. Bundgaard, S.R. Kurtz, D.S. Ginley, D.C. Olson, M.T. Lloyd, P. Morvillo, E.A. Katz, A. Elschner, O. Haillant, T.R. Currier, V. Shrotriya, M. Hermenau, M. Riede, K.R. Kirov, G. Trimmel, T. Rath, O. Inganäs, F. Zhang, M. Andersson, K. Tvingstedt, M. Lira-Cantu, D. Laird, C. McGuiness, S.J. Gowrisanker, M. Pannone, M. Xiao, J. hauch, R. Steim, D.M. DeLongchamp, R. Rösch, H. Hoppe, N. Espinosa, A. Urbina, G. Yaman-Uzunoglu, J.-B. Bonekamp, A.J.J.M. van Breemen, C. Girotto, E. Voroshazi, F.C. Krebs, Consensus stability testing protocols for organic photovoltaic materials and devices, Sol. Energy Mater. Sol. Cells. 95 (2011) 1253–1267. doi:10.1016/j.solmat.2011.01.036.

[176] Z. He, C. Zhong, S. Su, M. Xu, H. Wu, Y. Cao, Enhanced power-conversion efficiency in polymer solar cells using an inverted device structure, Nat. Photon. 6 (2012) 593–597. doi:10.1038/nphoton.2012.190.

[177] Y.W. Soon, H. Cho, J. Low, H. Bronstein, I. McCulloch, J.R. Durrant, Correlating

triplet yield, singlet oxygen generation and photochemical stability in polymer/fullerene blend films, Chem. Commun. 49 (2013) 1291. doi:10.1039/c2cc38243a.

[178] M. Tessarolo, A. Guerrero, D. Gedefaw, M. Bolognesi, M. Prosa, X. Xu, M. Mansour, E. Wang, M. Seri, M.R. Andersson, M. Muccini, G. Garcia-Belmonte, Predicting thermal stability of organic solar cells through an easy and fast capacitance measurement, Sol. Energy Mater. Sol. Cells. 141 (2015) 240–247. doi:10.1016/j.solmat.2015.05.041.

[179] J. Razzell-Hollis, J. Wade, W.C. Tsoi, Y. Soon, J. Durrant, J.-S. Kim, Photochemical stability of high efficiency PTB7:PC 70 BM solar cell blends, J. Mater. Chem. A. 2 (2014) 20189–20195. doi:10.1039/C4TA05641H.

[180] Z. Huang, E.C. Fregoso, S. Dimitrov, P.S. Tuladhar, Y.W. Soon, H. Bronstein, I. Meager, W. Zhang, I. McCulloch, J.R. Durrant, Optimisation of diketopyrrolopyrrole:fullerene solar cell performance through control of polymer molecular weight and thermal annealing, J. Mater. Chem. A. 2 (2014) 19282–19289. doi:10.1039/C4TA03589E.

[181] J.A. Hauch, P. Schilinsky, S.A. Choulis, R. Childers, M. Biele, C.J. Brabec, Flexible organic P3HT: PCBM bulk-heterojunction modules with more than 1 year outdoor lifetime, Sol. Energy Mater. Sol. Cells. 92 (2008) 727–731. doi:10.1016/j.solmat.2008.01.004.

[182] S.B. Sapkota, A. Spies, B. Zimmermann, I. D??rr, U. W??rfel, Promising long-term stability of encapsulated ITO-free bulk-heterojunction organic solar cells under different aging conditions, Sol. Energy Mater. Sol. Cells. 130 (2014) 144–150. doi:10.1016/j.solmat.2014.07.004.

[183] W. Wang, C.J. Schaffer, L. Song, V. Körstgens, S. Pröller, E.D. Indari, T. Wang, A. Abdelsamie, S. Bernstorff, P. Müller-Buschbaum, In operando morphology investigation of inverted bulk heterojunction organic solar cells by GISAXS, J. Mater. Chem. A. 3 (2015) 8324–8331. doi:10.1039/C5TA01109D.

[184] C.J. Schaffer, C.M. Palumbiny, M.A. Niedermeier, C. Jendrzejewski, G. Santoro, S. V. Roth, P. Müller-Buschbaum, A Direct Evidence of Morphological

Degradation on a Nanometer Scale in Polymer Solar Cells, Adv. Mater. 25 (2013) 6760–6764. doi:10.1002/adma.201302854.

[185] J.-B. Bonekamp, A.J. Moulé, K. Meerholz, Detailed study of the decay mechanism in polymeric OLEDs, in: Z.H. Kafafi, P.A. Lane (Eds.), 2005: p. 593713. doi:10.1117/12.620517.

[186] W. Greenbank, L. Hirsch, G. Wantz, S. Chambon, Interfacial thermal degradation in inverted organic solar cells, Appl. Phys. Lett. 107 (2015). doi:10.1063/1.4938554.

[187] F. Hermerschmidt, A. Savva, E. Georgiou, S.M. Tuladhar, J.R. Durrant, I. McCulloch, D.D.C. Bradley, C.J. Brabec, J. Nelson, S.A. Choulis, Influence of the Hole Transporting Layer on the Thermal Stability of Inverted Organic Photovoltaics Using Accelerated-Heat Lifetime Protocols, ACS Appl. Mater. Interfaces. 9 (2017) 14136–14144. doi:10.1021/acsami.7b01183.

[188] S. Chambon, L. Derue, M. Lahaye, B. Pavageau, L. Hirsch, G. Wantz, MoO3 Thickness, Thermal Annealing and Solvent Annealing Effects on Inverted and Direct Polymer Photovoltaic Solar Cells, Materials (Basel). 5 (2012) 2521–2536. doi:10.3390/ma5122521.

[189] M. Nyman, S. Dahlström, O.J. Sandberg, R. Österbacka, Unintentional Bulk Doping of Polymer-Fullerene Blends from a Thin Interfacial Layer of MoO 3, Adv. Energy Mater. 6 (2016) 1600670. doi:10.1002/aenm.201600670.

[190] K.E. Lee, L. Liu, T.L. Kelly, Effect of Molybdenum Oxide Electronic Structure on Organic Photovoltaic Device Performance: An X-ray Absorption Spectroscopy Study, J. Phys. Chem. C. 118 (2014) 27735–27741. doi:10.1021/jp508972v.

[191] B. Azzopardi, C.J.M. Emmott, A. Urbina, F.C. Krebs, J. Mutale, J. Nelson, Economic assessment of solar electricity production from organic-based photovoltaic modules in a domestic environment, Energy Environ. Sci. 4 (2011) 3741. doi:10.1039/c1ee01766g.

[192] F. Machui, M. Hösel, N. Li, G.D. Spyropoulos, T. Ameri, R.R. Søndergaard, M. Jørgensen, A. Scheel, D. Gaiser, K. Kreul, D. Lenssen, M. Legros, N. Lemaitre,

M. Vilkman, M. Välimäki, S. Nordman, C.J. Brabec, F.C. Krebs, Cost analysis of roll-to-roll fabricated ITO free single and tandem organic solar modules based on data from manufacture, Energy Environ. Sci. 7 (2014) 2792. doi:10.1039/C4EE01222D.

[193] N. Espinosa, R. García-Valverde, A. Urbina, F. Lenzmann, M. Manceau, D. Angmo, F.C. Krebs, Life cycle assessment of ITO-free flexible polymer solar cells prepared by roll-to-roll coating and printing, Sol. Energy Mater. Sol. Cells. 97 (2012) 3–13. doi:10.1016/j.solmat.2011.09.048.

[194] F.C. Krebs, S.A. Gevorgyan, J. Alstrup, A roll-to-roll process to flexible polymer solar cells: model studies, manufacture and operational stability studies, J. Mater. Chem. 19 (2009) 5442. doi:10.1039/b823001c.

[195] F.C. Krebs, All solution roll-to-roll processed polymer solar cells free from indium-tin-oxide and vacuum coating steps, Org. Electron. 10 (2009) 761–768. doi:10.1016/j.orgel.2009.03.009.

[196] F. Zhang, X. Xu, W. Tang, J. Zhang, Z. Zhuo, J. Wang, J. Wang, Z. Xu, Y. Wang, Recent development of the inverted configuration organic solar cells, Sol. Energy Mater. Sol. Cells. 95 (2011) 1785–1799. doi:10.1016/j.solmat.2011.02.002.

[197] C. Waldauf, M. Morana, P. Denk, P. Schilinsky, K. Coakley, S.A. Choulis, C.J. Brabec, Highly efficient inverted organic photovoltaics using solution based titanium oxide as electron selective contact, Appl. Phys. Lett. 89 (2006) 233517. http://link.aip.org/link/?APL/89/233517/1.

[198] K. Norrman, M. V Madsen, S.A. Gevorgyan, F.C. Krebs, Degradation Patterns in Water and Oxygen of an Inverted Polymer Solar Cell, J. Am. Chem. Soc. 132 (2010) 16883–16892. doi:10.1021/ja106299g.

[199] C.-P. Chen, Y.-D. Chen, S.-C. Chuang, High-performance and highly durable inverted organic photovoltaics embedding solution-processable vanadium oxides as an interfacial hole-transporting layer., Adv. Mater. 23 (2011) 3859–63. doi:10.1002/adma.201102142.

[200] K. Zilberberg, J. Meyer, T. Riedl, Solution processed metal-oxides for organic

electronic devices, J. Mater. Chem. C. 1 (2013) 4796. doi:10.1039/c3tc30930d.

[201] X. Li, F. Xie, S. Zhang, J. Hou, W.C. Choy, MoOx and V2Ox as hole and electron transport layers through functionalized intercalation in normal and inverted organic optoelectronic devices, Light Sci. Appl. 4 (2015) e273. doi:10.1038/lsa.2015.46.

[202] J. Krantz, T. Stubhan, M. Richter, S. Spallek, I. Litzov, G.J. Matt, E. Spiecker, C.J. Brabec, Spray-Coated Silver Nanowires as Top Electrode Layer in Semitransparent P3HT:PCBM-Based Organic Solar Cell Devices, Adv. Funct. Mater. 23 (2013) 1711–1717. doi:10.1002/adfm.201202523.

[203] D. Angmo, J. Sweelssen, R. Andriessen, Y. Galagan, F.C. Krebs, Inkjet Printing of Back Electrodes for Inverted Polymer Solar Cells, Adv. Energy Mater. 3 (2013) 1230–1237. doi:10.1002/aenm.201201050.

[204] Y. Galagan, S. Shanmugam, J.P. Teunissen, T.M. Eggenhuisen, A.F.K.V. Biezemans, T. Van Gijseghem, W.A. Groen, R. Andriessen, Solution processing of back electrodes for organic solar cells with inverted architecture, Sol. Energy Mater. Sol. Cells. 130 (2014) 163–169. doi:10.1016/j.solmat.2014.07.007.

[205] Y.-F. Lim, S. Lee, D.J. Herman, M.T. Lloyd, J.E. Anthony, G.G. Malliaras, Spray-deposited poly(3,4-ethylenedioxythiophene):poly(styrenesulfonate) top electrode for organic solar cells, Appl. Phys. Lett. 93 (2008) 193301. doi:10.1063/1.3021022.

[206] F.C. Krebs, R. Søndergaard, M. Jørgensen, Printed metal back electrodes for R2R fabricated polymer solar cells studied using the LBIC technique, Sol. Energy Mater. Sol. Cells. 95 (2011) 1348–1353. doi:10.1016/j.solmat.2010.11.007.

[207] D. Angmo, J. Sweelssen, R. Andriessen, Y. Galagan, F.C. Krebs, Inkjet Printing of Back Electrodes for Inverted Polymer Solar Cells, Adv. Energy Mater. 3 (2013) 1230–1237. doi:10.1002/aenm.201201050.

[208] M. Neophytou, F. Hermerschmidt, A. Savva, E. Georgiou, S.A. Choulis, Highly efficient indium tin oxide-free organic photovoltaics using inkjet-printed silver nanoparticle current collecting grids, Appl. Phys. Lett. 101 (2012) 193302.

doi:10.1063/1.4765343.

[209] E. Georgiou, S.A. Choulis, F. Hermerschmidt, S.M. Pozov, I. Burgués-Ceballos, C. Christodoulou, G. Schider, S. Kreissl, R. Ward, E.J.W. List-Kratochvil, C. Boeffel, Printed Copper Nanoparticle Metal Grids for Cost-Effective ITO-Free Solution Processed Solar Cells, Sol. RRL. (2018) 1700192. doi:10.1002/solr.201700192.

[210] A. Savva, M. Neophytou, C. Koutsides, K. Kalli, S.A. Choulis, Synergistic effects of buffer layer processing additives for enhanced hole carrier selectivity in inverted Organic Photovoltaics, Org. Electron. 14 (2013) 3123–3130. doi:10.1016/j.orgel.2013.07.024.

[211] Y. Noguchi, T. Sekitani, T. Yokota, T. Someya, Direct inkjet printing of silver electrodes on organic semiconductors for thin-film transistors with top contact geometry, Appl. Phys. Lett. 93 (2008) 43303. doi:10.1063/1.2959728.

[212] C. Girotto, B.P. Rand, J. Genoe, P. Heremans, Exploring spray coating as a deposition technique for the fabrication of solution-processed solar cells, Sol. Energy Mater. Sol. Cells. 93 (2009) 454–458. doi:10.1016/j.solmat.2008.11.052.

[213] J. Yang, R. Zhu, Z. Hong, Y. He, A. Kumar, Y. Li, Y. Yang, A robust inter-connecting layer for achieving high performance tandem polymer solar cells., Adv. Mater. 23 (2011) 3465–70. doi:10.1002/adma.201100221.

[214] Z. Hu, J. Zhang, Z. Hao, Y. Zhao, Influence of doped PEDOT:PSS on the performance of polymer solar cells, Sol. Energy Mater. Sol. Cells. 95 (2011) 2763–2767. doi:10.1016/j.solmat.2011.04.040.

[215] C. Girotto, B.P. Rand, S. Steudel, J. Genoe, P. Heremans, Nanoparticle-based, spray-coated silver top contacts for efficient polymer solar cells, Org. Electron. 10 (2009) 735–740. doi:10.1016/j.orgel.2009.03.006.

[216] K. Park, D. Seo, J. Lee, Conductivity of silver paste prepared from nanoparticles, Colloids Surfaces A Physicochem. Eng. Asp. 313–314 (2008) 351–354. doi:10.1016/j.colsurfa.2007.04.147.

[217] H.-H. Lee, K.-S. Chou, K.-C. Huang, Inkjet printing of nanosized silver colloids., Nanotechnology. 16 (2005) 2436–41. doi:10.1088/0957-4484/16/10/074.

[218] K.-S. Chou, K.-C. Huang, H.-H. Lee, Fabrication and sintering effect on the morphologies and conductivity of nano-Ag particle films by the spin coating method, Nanotechnology. 16 (2005) 779–784. doi:10.1088/0957-4484/16/6/027.

[219] B.A.E. Courtright, S.A. Jenekhe, Polyethylenimine Interfacial Layers in Inverted Organic Photovoltaic Devices: Effects of Ethoxylation and Molecular Weight on Efficiency and Temporal Stability, ACS Appl. Mater. Interfaces. 7 (2015) 26167–26175. doi:10.1021/acsami.5b08147.

[220] X. Jia, L. Zhang, Q. Luo, H. Lu, X. Li, Z. Xie, Y. Yang, Y.-Q. Li, X. Liu, C.-Q. Ma, Power Conversion Efficiency and Device Stability Improvement of Inverted Perovskite Solar Cells by Using a ZnO:PFN Composite Cathode Buffer Layer, ACS Appl. Mater. Interfaces. 8 (2016) 18410–18417. doi:10.1021/acsami.6b03724.

[221] S. Woo, W. Hyun Kim, H. Kim, Y. Yi, H.-K. Lyu, Y. Kim, 8.9% Single-Stack Inverted Polymer Solar Cells with Electron-Rich Polymer Nanolayer-Modified Inorganic Electron-Collecting Buffer Layers, Adv. Energy Mater. 4 (2014) 1301692. doi:10.1002/aenm.201301692.

[222] C. Liu, Z. Li, X. Zhang, W. Guo, L. Zhang, S. Ruan, Annealing-Free ZnO:PEI Composite Cathode Interfacial Layer for Efficient Organic Solar Cells, ACS Photonics. 4 (2017) 2952–2958. doi:10.1021/acsphotonics.7b01096.

[223] X. Min, F. Jiang, F. Qin, Z. Li, J. Tong, S. Xiong, W. Meng, Y. Zhou, Polyethylenimine Aqueous Solution: A Low-Cost and Environmentally Friendly Formulation to Produce Low-Work-Function Electrodes for Efficient Easy-to-Fabricate Organic Solar Cells, ACS Appl. Mater. Interfaces. 6 (2014) 22628–22633. doi:10.1021/am5077974.

[224] H.-C. Chen, S.-W. Lin, J.-M. Jiang, Y.-W. Su, K.-H. Wei, Solution-Processed Zinc Oxide/Polyethylenimine Nanocomposites as Tunable Electron Transport Layers for Highly Efficient Bulk Heterojunction Polymer Solar Cells, ACS Appl. Mater. Interfaces. 7 (2015) 6273–6281. doi:10.1021/acsami.5b00521.

APPENDIX

Publications related directly with the Thesis

M. Neophytou, **E. Georgiou**, M.M. Fyrillas, S.A. Choulis, Two step sintering process and metal grid design optimization for highly efficient ITO free organic photovoltaics, Sol. Energy Mater. Sol. Cells. 122 (2014) 1–7. doi:10.1016/j.solmat.2013.11.021.

E. Georgiou, A. Savva, M. Neophytou, F. Hermerschmidt, T. Demosthenous, S.A. Choulis, Evaporation-free inverted organic photovoltaics using a mixture of silver nanoparticle ink formulations for solution-processed top electrodes, Appl. Phys. Lett. 105 (2014) 233901. doi:10.1063/1.4903893.

S.A. Gevorgyan, N. Espinosa, L. Ciammaruchi, B. Roth, F. Livi, S. Tsopanidis, S. Züfle, S. Queirós, A. Gregori, G.A. dos R. Benatto, M. Corazza, M. V. Madsen, M. Hösel, M.J. Beliatis, T.T. Larsen-Olsen, F. Pastorelli, A. Castro, A. Mingorance, V. Lenzi, D. Fluhr, R. Roesch, M. Maria Duarte Ramos, A. Savva, H. Hoppe, L.S.A. Marques, I. Burgués, **E. Georgiou**, L. Serrano-Luján, F.C. Krebs, Baselines for Lifetime of Organic Solar Cells, (2016). doi:10.1002/aenm.201600910.

F. Hermerschmidt, A. Savva, **E. Georgiou**, S.M. Tuladhar, J.R. Durrant, I. McCulloch, D.D.C. Bradley, C.J. Brabec, J. Nelson, S.A. Choulis, Influence of the Hole Transporting Layer on the Thermal Stability of Inverted Organic Photovoltaics Using Accelerated-Heat Lifetime Protocols, ACS Appl. Mater. Interfaces. 9 (2017) 14136–14144. doi:10.1021/acsami.7b01183.

E. Georgiou, S.A. Choulis, F. Hermerschmidt, S.M. Pozov, I. Burgués-Ceballos, C. Christodoulou, G. Schider, S. Kreissl, R. Ward, E.J.W. List-Kratochvil, C. Boeffel, Printed Copper Nanoparticle Metal Grids for Cost-Effective ITO-Free Solution Processed Solar Cells, Sol. RRL. (2018) 1700192. doi:10.1002/solr.201700192.

Other Publications related with the research activity of Molecular Electronics and Photonics research unit

M. Neophytou, F. Hermerschmidt, A. Savva, **E. Georgiou**, S.A. Choulis, Highly efficient

indium tin oxide-free organic photovoltaics using inkjet-printed silver nanoparticle current collecting grids, Appl. Phys. Lett. 101 (2012). doi:10.1063/1.4765343.

A.Savva, **E. Georgiou**, G. Papazoglou, A.Z. Chrusou, K. Kapnisis, S.A. Choulis, Photovoltaic analysis of the effects of PEDOT:PSS-additives hole selective contacts on the efficiency and lifetime performance of inverted organic solar cells, Sol. Energy Mater. Sol. Cells. 132 (2015) 507–514. doi:10.1016/j.solmat.2014.10.004.

I. Burgués-Ceballos, A. Savva, **E. Georgiou**, K. Kapnisis, P. Papagiorgis, A. Mousikou, G. Itskos, A. Othonos, S.A. Choulis, The influence of additives in the stoichiometry of hybrid lead halide perovskites, AIP Adv. 7 (2017) 115304. doi:10.1063/1.5010261.

Presentations

E. Georgiou, M. Neophytou and S. A. Choulis, "High Performance Indium Tin Oxide - Free Organic Photovoltaics", International Winterschool on Bioelectronics, Kirchberg in Tirol, Austria. April 2014. **Poster presentation**.

E. Georgiou, A. Savva, S. A. Choulis, Evaporation-free inverted organic photovoltaics using a mixture of silver nanoparticle ink formulations for solution-processed top electrodes., EMRS spring Metting, Lille, France, May 2015. **Oral Presentation**.